University of Navarra

School of Sciences

Role of EPCR in breast cancer progression and metastasis

Naiara Perurena Aizcorbe

Doctoral Thesis

University of Navarra

School of Sciences

Role of EPCR in breast cancer progression and metastasis

A dissertation presented by **Naiara Perurena Aizcorbe** to the University of Navarra in partial fulfillment of the requirements for the degree of Doctor of Philosophy.

I certify that the present work has been conducted under my supervision at the Oncology Department of the Center for Applied Medical Research and authorize its presentation to the members of the Thesis Committee.

Pamplona, 27th August 2015

Dr. Fernando Lecanda Cordero

This work was supported by:

- A short-term FPU fellowship from the Ministry of Education (EST13/00784).
- A predoctoral FPU fellowship from the Ministry of Education (AP2010-2197).
- A predoctoral fellowship from the Government of Navarra.
- The Spanish Ministry of Economy and Competitiveness SAF2012-40056.
- The Cancer Research Thematic Network of the Health Institute Carlos III (RTICC RD12/0036/0066).
- UTE project from the Foundation for Applied Medical Research.
- The CSHL Cancer Center Support Grant 5P30CA045508.

Gracias a la Universidad de Navarra y al Centro de Investigación Médica Aplicada (CIMA) por la oportunidad de realizar esta tesis doctoral.

Gracias al Departamento de Bioquímica y Genética por permitirme formarme como docente.

Gracias a todas aquellas personas que han contribuido a este trabajo:

A Fernando, por haberme ofrecido embarcarme en este proyecto. Todo lo aprendido en el camino recorrido ha merecido la pena sin duda alguna. Gracias por tu disposición y ayuda siempre que la he necesitado.

A Carolina y Susana, por vuestra ayuda indispensable durante estos años. Y por todos los buenos momentos compartidos.

A los demás miembros del laboratorio 1.02. A los que me enseñaron en mis inicios: Iker, Diego y Karmele. A los que me han acompañado en la recta final: Haritz, Adrián, Silvia y Paolo. A Silve, por darme la oportunidad de participar en otros proyectos.

A José Hermida y Eva Molina, por sus consejos y todas las herramientas prestadas.

A Laura Guembe y todo el equipo de Morfología, por todo el trabajo realizado.

A Víctor Segura y Elizabeth Guruceaga, del servicio de Bioinformática.

Thanks to Dr. Mikala Egeblad for giving me the opportunity to work in her laboratory at Cold Spring Harbor Laboratory for three months. Thanks to Dr. Ana Almeida, for her help and friendship.

Al Dr. Gomis y a la Dra. Santisteban, por las líneas celulares utilizadas en este trabajo.

A todo el personal del CIMA que en algún momento me ha prestado su ayuda.

Gracias a las personas del CIMA con las que he compartido buenos momentos durante estos años: Inés, Marta, Miriam, Arrate, María.

Gracias a todas las personas que me han apoyado y han estado a mi lado durante estos años:

A mis amigas de Leitza, especialmente a Iera, Leire y Oihana. Y a mis amigas farmacéuticas: Amaia, Ainhoa, Andrea, Iosune, Vanesa, Cristina y Ujué.

A mis padres, por su constante interés y apoyo incondicional. A mi hermano, por ayudarme a distraerme. A mi abuelo y a mi tía Ainhoa.

A Iker, por estar a mi lado.

INDEX

LIST OF ABBREVIATIONS

A

7AAD	7-Aminoactinomycin D
ADAM17/12	ADAM metallopeptidase domain 17 (TACE)/12
AJCC	American Joint Committee on Cancer
AKT	v-akt murine thyoma viral oncogene homolog
ANV	Antigen negative variant
APC	Activated protein C
APS	Ammonium persulfate
AR	Androgen receptor
ATCC	American Type Culture Collection

B

Bax	Bcl-2-Associated X Protein
BCA	Bicinchoninic acid
Bcl-2	B-cell CLL/Lymphoma 2
BL	Bioluminescence
BLI	Bioluminescence imaging
BMP	Bone morphogenetic protein
BSA	Bovine serum albumin

C

CAF	Cancer associated fibroblast
cAMP	Cyclic adenosine monophosphate
CAV1	Caveolin-1
CCL2	Chemokine (C-C motif) ligand 2
CCR2	Chemokine (C-C motif) receptor 2
CDH1	E-cadherin
CK	Cytokeratin
CLDN	Claudin
CM	Conditioned medium/media
COX2	Cyclooxigenase 2
CSF-1	Colony stimulating factor 1
CTC	Circulating tumor cell
CXCL1	Chemokine (C-X-C motif) ligand 1
CXCR4	Chemokine (C-X-C motif) receptor 4

D

2D	2-Dimensional
3D	3-Dimensional

DC	Dendritic cells
DEPC	Diethylpyrocarbonate
DMSO	Dimethyl sulfoxide
DPBS	Dulbecco's Modified Phosphate Buffered Saline
DR4/TRAILR1	Death receptor 4/TRAIL receptor 1
DR5/TRAILR2	Death receptor 5/TRAIL receptor 2
DTT	Dithiothreitol
Dvl-2	Dishevelled segment polarity protein 2

E

EdU	5-ethynyl-2'-deoxyuridine
EGFR	Epidermal growth factor receptor
EMT	Epithelial-mesenchymal transition
EPCR	Endothelial protein C receptor
ER	Estrogen receptor
EREG	Epiregulin
ERK	Extracellular signal regulated kinase

F

FABF7	Fatty acid binding protein 7
FACS	Fluorescence Activated Cell Sorting
FLNB/C	Filamin B/C
FOXA1	Hepatocyte nuclear factor 3α
FV/VII	Factor V/VII
FZD8	Frizzled class receptor 8

G

GAPDH	Glyceraldehyde-3-phosphate dehydrogenase
GATA3	GATA binding protein 3
GLI2	GLI family zinc finger 2
GO	Gene Ontology

H

H&E	Hematoxylin-eosin
HER2/ERBB2	Human epidermal growth factor receptor 2
HGF	Hepatocyte growth factor
HIF	Hypoxia inducible factor
HRP	Horseradish peroxidase
HSPA1A/B	Heat Shock 70 kDa Protein 1A/B

I

ID1/3	Inhibitor of DNA binding 1/3, dominant negative helix-loop-helix protein

IFN	Inteferon
IGFBP	Insulin-like growth factor binding protein
IIa	Thrombin
IL6/8	Interleukin 6/8
ILC	Invasive lobular carcinoma
IPA	Ingenuity pathway analysis
ITGB4	Integrin, beta 4

J

JAG1	Jagged-1
JAK	Janus kinase
JNK	c-Jun N-terminal kinase

K

KRT19	Keratin 19

L

LIV1/SLC39A6	Solute carrier family 39 zinc transporter, member 6
LOXL2	Lysyl oxidase-like 2
LPA	Lysophosphatidic acid

M

Mac-1	Vascular cell adhesion molecule 1
MAP3K1	Mitogen-activated protein kinase kinase kinase 1, E3 ubiquitin protein ligase
Mcl-1	Myeloid cell leukemia 1
MCP-1	Monocyte chemoattractant protein 1
MDSC	Myeloid derived suppressor cell
MENA	Mammalian Ena
Mfp-MDA-MB-231	Mammary fat pad enhanced MDA-MB-231
MMC	Mouse mammary carcinoma
MMP	Matrix metalloproteinase
MSC	Mesenchymal stem cell
MSLN	Mesothelin
MTS	3-(4,5-dimethylthiazol-2-yl)-5-(3-carboxy methoxyphenyl)-2-(4-sulfophenyl)-2H-tetrazolium

N

NF-κB	Nuclear factor kappa B
NK	Natural killer
NOS	Invasive ductal carcinoma, not otherwise specified
NST	Invasive carcinoma of no special type
NWASP	Wiskott-Aldrich syndrome-like

P

PAR1	Protease activated receptor 1
PARP	Poly ADP ribose polymerase
PBN	DPBS + 1% BSA + 0.02% sodium azide
PC	Protein C
PCh	Phosphatidylcholine
PfEMP1	*Plasmodium falciparum* erythrocyte membrane protein I
PI3K	Phosphatidylinositol 3-kinase
PIK3CA	Phosphatidylinositol-4,5-bisphosphate 3-kinase, catalytic subunit alpha
PR	Progesterone receptor
PR3	Proteinase 3
PS	Phosphatidylserine
PTEN	Phosphatase and tensin homolog
PTHrP	Parathyroid hormone-like protein
PyMT	Polyoma middle T

Q

qPCR	Quantitative polymerase chain reaction

R

RUNX2	Runt-related transcription factor 2

S

S1P	Sphingosine-1-phosphate
S1P1	Sphingosine-1-phosphate receptor 1
SD	Standard deviation
SDS	Sodium dodecyl sulfate
SEM	Standard error of the mean
SPARC	Secreted protein, acidic, cysteine-rich (osteonectin)
SRC	V-Src Avian Sarcoma (Schmidt-Ruppin A-2) Viral Oncogene Homolog
STAT1/3	Signal transducer and activator of transcription 1/3

T

TAE	Tris-Acetic acid-EDTA
TAM	Tumor associated macrophage
TCGA	The Cancer Genome Atlas
TEM	Transendothelial migration
TEMED	Tetramethylethylenediamine
TF	Tissue factor
TGFβ	Transforming growth factor, beta
TM	Thrombomodulin

T_m	Melting temperature
TN	Triple-negative
TNC	Tenascin C
TNF	Tumor necrosis factor
TNFRSF10A/B	Tumor necrosis factor receptor superfamily member 10A/B
TNM	Tumor-node-metastasis
TP53	Tumor protein p53
TRAIL	TNF-related apoptosis inducing ligand

U

uPA	Urokinase plasminogen activator

V

VEGF	Vascular endothelial growth factor

W

WHO	World Health Organization
WNT	Wingless
WT	Wild type

X

XBP1	X-box binding protein 1

Z

ZO-1	Tight junction protein 1

I Introduction

1. BREAST CANCER

1.1. Epidemiology

Breast cancer is the most frequently diagnosed and most fatal cancer in women[1]. In 2012, 1,676,600 new breast cancer cases and 521,900 breast cancer deaths were registered worldwide (GLOBOCAN)[1] (Figure 1). In Europe, breast cancer accounted for 28.8% (464,000) of new cancer cases and 16.8% (131,000) of cancer deaths in females[2]. In Spain, there were 25,215 new cancer cases and 6,075 deaths due to breast cancer[2]. However, it was the second leading cause of cancer death in females in the USA, where 234,190 new cases and 40,730 deaths are predicted for 2015[3].

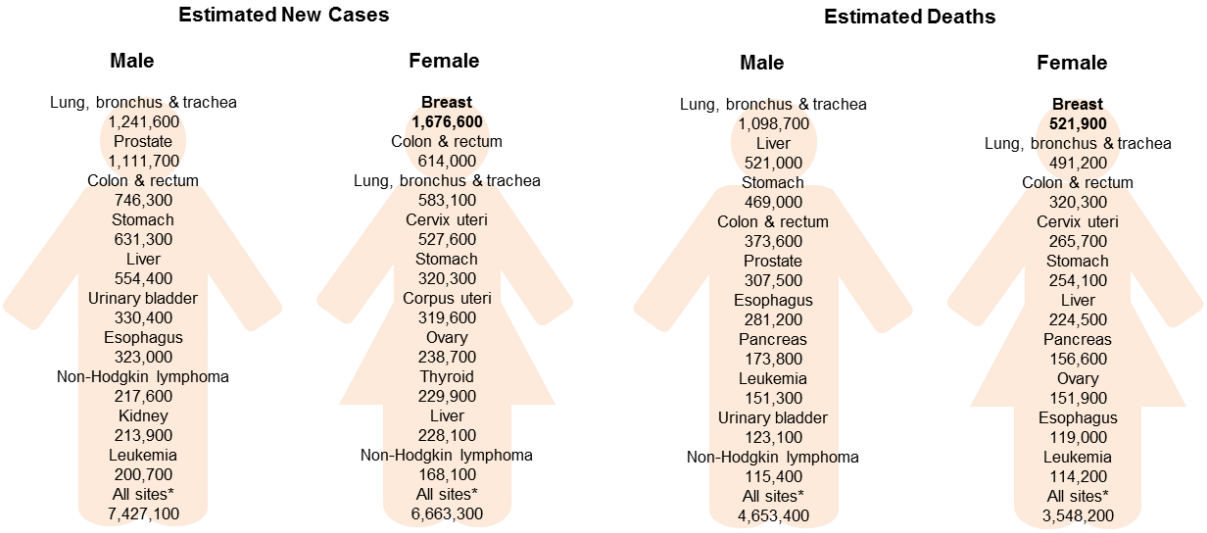

Figure 1. Estimated new cancer cases and deaths worldwide by sex. GLOBOCAN 2012. *Excluding non-melanoma skin cancers. Adapted from Torre LA *et al.*[1]

Most deaths among breast cancer patients occur as a consequence of cancer dissemination. Indeed, 5-year survival rate is around 99% when the tumor is localized, but decreases to 25.9% when the tumor has spread to other organs (SEER 18 2005-2011). Therefore, novel therapies to treat metastatic breast cancer and improve patient survival are urgently needed.

1.2. Classification

1.2.1. Histopathological classification

1.2.1.1. Breast cancer types

The first classification of breast tumors was performed based on their morphological characteristics. This classification was updated in 2012 by the World Health Organization (WHO) in the 4th Edition of WHO Classification of Tumors of the Breast (Appendix 1). The most frequent

subtype, ~75% of breast cancers, is the invasive carcinoma of no special type (NST), known previously as invasive ductal carcinoma, not otherwise specified (NOS)[4-6]. It is followed by the invasive lobular carcinoma (ILC), which accounts for ~10% of breast cancers[4-6]. NST comprises all tumors that lack specific characteristics of special subtypes and the diagnosis is made by exclusion[7]. Although some special types of breast cancer (adenoid cystic, medullary, mucinous and tubular carcinomas) have better overall outcomes, in general, histological typing is a weak prognostic marker and is not relevant for clinical decision making[4,8].

1.2.1.2. Histological grade

Histological grade of breast cancers is usually determined by the Nottingham grading system, also called the Elston-Ellis modification of the Scarff-Bloom-Richardson grading system[9,10]. The histological grade is indicative of the differentiation state of the tumor and it is established based on the semiquantitative assessment of three morphological features: tubule formation, mitotic activity and nuclear pleomorphism. Final grade is defined as: G1 (low grade or well differentiated), G2 (intermediate grade or moderately differentiated) and G3 (high grade or poorly differentiated)[9,10]. Histological grade is an established prognostic marker: risk of metastasis increases with grade, being higher for G3 tumors[8].

1.2.1.3. Stage

Breast tumors are staged following the TNM (tumor-node-metastasis) staging system, according to the latest 7th edition of the staging manual from the American Joint Committee on Cancer (AJCC) (Appendix 2). This is considered the most clinically useful cancer staging system. It is based on anatomic factors: tumor size (T), regional lymph node involvement (N) and distant metastases (M)[11]. Tumor size and axillary lymph-node status are established prognostic markers: metastasis risk increases with primary tumor size and the number of lymph-node metastases[8].

1.2.2. Immunohistochemical classification

Three receptors are routinely tested in clinical practice as prognostic and predictive markers: estrogen receptor (ER), progesterone receptor (PR) and human epidermal growth factor receptor 2 (HER2)[12] (Figure 2).

ER+ tumors are the most frequent (around 75% of invasive cancers) and respond to endocrine therapy, such as tamoxifen and aromatase inhibitors. Patients with ER+ tumors exhibit the best prognosis[12]. PR expression, usually associated with ER expression, has less clinical significance[12]. Approximately 10-15% of breast cancer patients have HER2 overexpression and/or amplification and can be treated with anti-HER2 agents[12]. The remaining 10-15% of breast cancers do not express ER, PR and HER2 and are called triple-negative (TN). These tumors are associated with the worst prognosis and lack targeted therapeutic options[12,13].

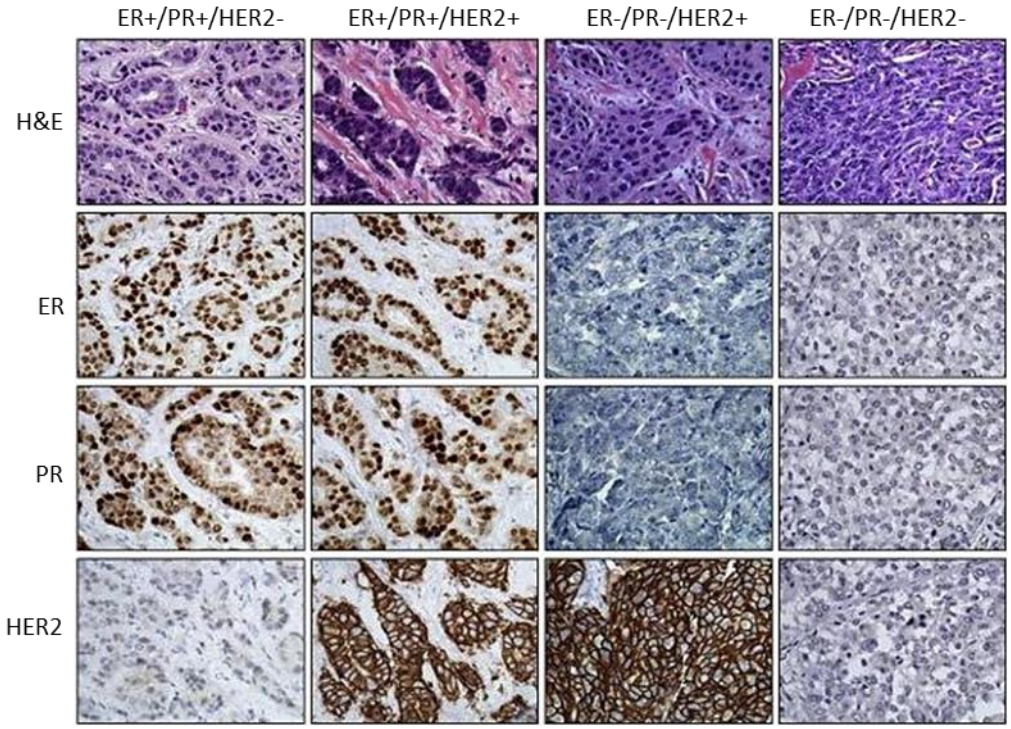

Figure 2. Classification of breast cancer based on the immunodetection of ER, PR and HER2. Representative images at 40X magnification are shown. Immunohistochemical classification results in four major groups: ER+/PR+/HER2-, ER+/PR+/HER2+, ER-/PR-/HER2+ and ER-/PR-/HER2-. From Rivenbark *et al.*[12]

1.2.3. Transcriptomic or Molecular classification

Transcriptomic analysis of breast tumors using microarrays has led to the identification of several molecular breast cancer subtypes. The first molecular classification was described by Perou *et al.* in 2000[14]. They analyzed 42 human normal and malignant breast tissues (36 infiltrating ductal carcinomas, 2 lobular carcinomas, 1 ductal carcinoma *in situ*, 1 fibroadenoma and 3 normal breast samples) by unsupervised clustering in order to group samples with similar gene expression patterns[14]. They found three ER- groups: basal-like, HER2+ and normal breast-like and one ER+ group (luminal epithelial)[14], which was further divided into luminal A and luminal B[15]. This classification was validated in other breast cancer cohorts[16]. More recently, new molecular subtypes have been identified: claudin-low, molecular apocrine and interferon-related group[17-20]. Interestingly, these molecular subtypes differ in incidence, clinical outcome and response to therapy[17].

There have been two major attempts to introduce this molecular classification into clinical practice: the development of PAM50, a 50-gene subtype predictor[21], and the development of an immunohistochemical assay able to reproduce the breast cancer classification obtained by microarray analysis[22] (Table 1). Yet tumor size, node status, histological grade and ER, PR and HER2 status continue to represent routinely evaluated parameters in clinical practice for prognosis prediction and treatment selection[23,24].

Table 1. Immunohistochemical markers that characterize molecular subtypes[5,16,17,22].

Molecular subtype	ER, PR, HER2	Additional markers
Basal-like	ER-, PR-, HER2-	CK5/6+ and/or EGFR+, high Ki67
HER2+	ER-, PR-, HER2+	CK5/6+/-, EGFR+/-, high Ki67
Normal breast-like	ER+/-, PR unknown, HER2-	CK5/6+, EGFR+, low Ki67
Luminal A	ER+, PR+/-, HER2+	Low Ki67
Luminal B	ER+, PR+/-, HER2+/-	High Ki67
Claudin-low	ER-, PR-, HER2-	CK5/6+/-, EGFR+/-, high Ki67, CLDN low/-, CDH1 low/-, high vimentin
Molecular apocrine	ER-, PR-, HER2+/-	AR+, CK5/6+/-, EGFR+/-, high Ki67
Interferon-related	ER+/-, PR unknown, HER2-	STAT1, high Ki67

1.2.3.1. Luminal A

Luminal A tumors are the most common and account for around 30% of all breast cancers[12,25]. They are associated with good prognosis and long-term survival and respond weakly to chemotherapy[15,16].

They are defined as ER+, PR+/- and HER2-, and display low histological grade and proliferation rates. They are characterized by high expression levels of genes related to ER signaling, such as ER, GATA binding protein 3 (GATA3), X-box binding protein 1 (XBP1), hepatocyte nuclear factor 3α (FOXA1), estrogen-regulated LIV-1 (solute carrier family 39 zinc transporter, member 6) and keratins 8 and 18, which are expressed by the luminal cells[12,14-16,25].

1.2.3.2. Luminal B

Luminal B tumors represent around 20% of breast cancers and have lower survival rates than luminal A tumors, but better clinical outcomes than basal-like, claudin-low and HER2+ tumors[12,25]. Luminal B tumors also express ER-regulated genes and differ from luminal A tumors because of the high expression of proliferation-related genes. They are defined as ER+, PR+/- and HER2+ or HER2- with high proliferation rate (high Ki67)[12,14-16,25].

1.2.3.3. HER2+

HER2+ tumors account for 17% of breast cancers and are characterized by high expression of HER2 and other genes in the HER2 amplicon. These tumors are negative for ER and PR and show high proliferation rates. Their poor clinical outcome has been significantly improved with the development of anti-HER2 therapies. In addition, HER2+ tumors respond relatively well to chemotherapy[12,14-16,25].

1.2.3.4. Basal-like

Basal-like tumors represent around 15% of breast cancers and have the worst clinical outcome, although they respond relatively well to neoadjuvant chemotherapy[12,25]. They express genes found in the expression profile of basal/myoepithelial cells of the mammary gland: keratins 5 and

17, laminin, ITGB4 (integrin, beta 4) and FABP7 (fatty acid binding protein 7)[14-16]. They are defined as TN tumors and have high grade and proliferation rates[12,25].

1.2.3.5. Normal breast-like

Normal breast-like tumors express genes found in adipocytes and other non-epithelial cell types[14,15]. More recently, it has been suggested that this group could be an artifact, in consequence of a disproportionately high content of normal tissue contamination[5].

1.2.3.6. Claudin-low

Claudin-low tumors were previously clustered within the basal-like group. They represent 10% of breast tumors and show poor prognosis and intermediate response rate to standard chemotherapy[18]. Claudin-low tumors are characterized by low to absent expression of luminal differentiation markers, high expression of epithelial-to-mesenchymal (EMT) transition markers, immune response genes and cancer stem cell-like features[18]. The majority of claudin-low tumors are TN invasive ductal carcinomas with a high frequency of metaplastic and medullary differentiation[18].

1.2.3.7. Molecular apocrine

The molecular apocrine subtype has been identified in two independent experiments[19,26]. In both cases these tumors accounted for 11-12% of breast tumors analyzed (39/355 and 6/49). They are mainly related to the HER2+ class[19]. Apocrine tumors are ER negative with increased androgen signaling and show some apocrine features, such as abundant eosinophilic cytoplasm and prominent nucleoli. These tumors show early recurrence, mainly to the brain, despite a relatively good response to chemotherapy[26].

1.2.3.8. Interferon-related

Hu *et al.*[20] identified this group in addition to the molecular subtypes described in the molecular classification by Perou *et al.* It included 8% of the tumors analyzed (25/315), characterized by low differentiation (32% grade 2, 64% grade 3) and high expression of interferon (IFN)-regulated genes, classified into “immune response” and “defense response” Gene Ontology (GO, http://geneontology.org) categories[20]. It also showed high levels of STAT1, the transcription factor thought to mediate IFN-regulation of gene expression[20]. Genes in the IFN cluster have been linked to lymph node metastasis and poor prognosis[20]; however, the clinical significance of this newly described class needs to be determined[5].

1.3. Breast tumorigenesis

1.3.1. Driver genes

Cancer is heavily driven by alteration of the genomic landscape, as a consequence of two processes: the continuous acquisition of heritable genetic variation in individual cells and the natural selection of resultant phenotypes[27]. Genetic variation includes substitutions; insertions or deletions of small or large segments of DNA; rearrangements; copy number variations; integration of external DNA from viruses; and epigenetic changes that alter gene expression[27]. Although several susceptibility genes related to inherited breast cancers have been found[28,29], the majority of genetic variants present in cancers are somatic. These somatic variants can be drivers (they are causally implicated in oncogenesis) or passengers (they are present in the tumors but not involved in oncogenesis)[27]. Importantly, the pattern of driver and passenger variants is dynamic and probably changes over the course of the disease. For example, it has been shown that passenger variants present in minor subclones of the tumor can be selected during treatment, becoming drivers that cause the expansion of the resistant subclones and recurrence[27]. These genetic alterations confer several distinctive and complementary capabilities to cancer cells (hallmarks of cancer), which enable primary tumor growth: sustained proliferative signaling, evasion of growth factor suppressors, evasion of immunesurveillance, replicative immortality, angiogenesis, resistance to cell death and deregulation of cellular energetics[30].

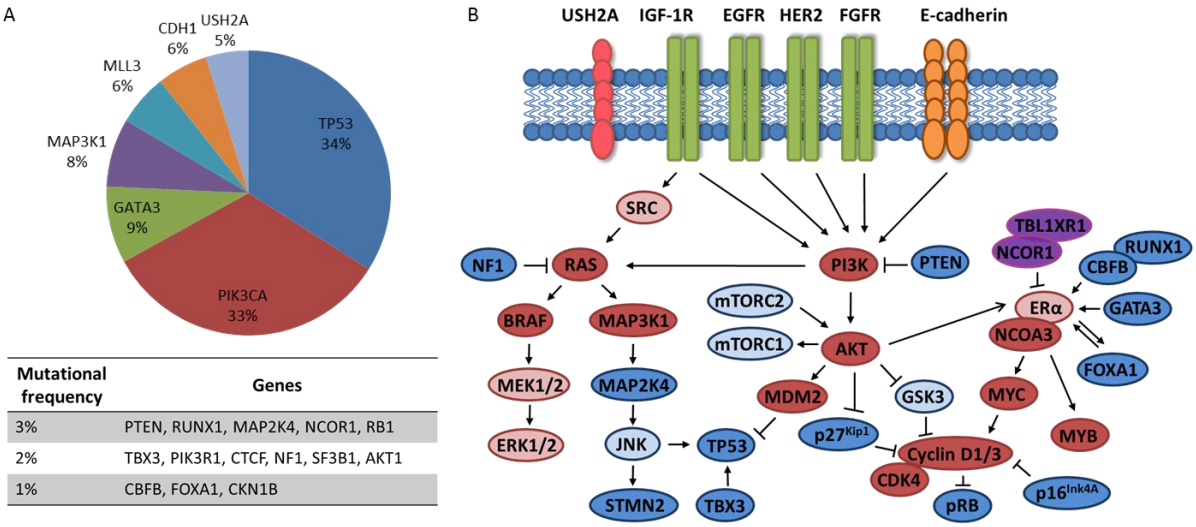

Mutational frequency	Genes
3%	PTEN, RUNX1, MAP2K4, NCOR1, RB1
2%	TBX3, PIK3R1, CTCF, NF1, SF3B1, AKT1
1%	CBFB, FOXA1, CKN1B

Figure 3. Key mutations and altered signaling pathways in breast cancer. A. Most frequently mutated genes. B. Altered signaling pathways based on the mutational landscape. Colors indicate tumor suppressors (blue), oncogenes (red) or mutant genes with unclear roles (purple), and lighter shading marks pathway components in which somatic mutations have not been identified. Adapted from Polyak and Filho[31].

Several studies have identified driver genes in breast tumorigenesis: genes with mutations or gene-expression alterations that are involved in breast cancer progression[32-38] (Appendix 3). Most mutations are infrequent or non-recurrent and only a few genes present a mutational frequency that approaches or exceeds 10%: TP53 (34%), PIK3CA (33%), GATA3 (9%) and MAP3K1 (8%)[39-41] (Figure 3).

1.3.2. Protumorigenic functions of the tumor microenvironment

Tumors are organ-like structures composed not only of cancer cells, but also stromal cells and extracellular-matrix (ECM), which constitute the tumor microenvironment[42]. Stromal cell types present in breast tumors include: endothelial cells, pericytes, mesenchymal stem cells, fibroblasts, adipocytes and several immune cell types (macrophages, monocytes, dendritic cells, neutrophils, natural killer cells, T and B lymphocytes, myeloid-derived suppressor cells, mast cells and platelets)[42-44] (Figure 4). Importantly, cancer cells can educate these cell types to create a tumor-supportive microenvironment[45-48] (Table 2).

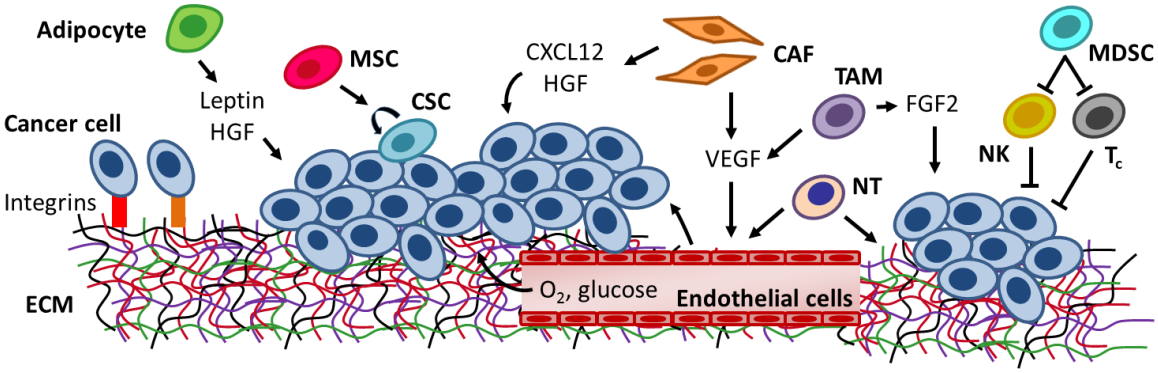

Figure 4. The tumor microenvironment. Components and functions of the tumor microenvironment are indicated. CSC: cancer stem cell; NT: neutrophil.

ECM is composed of several macromolecules such as fibrillar collagens, fibronectin and proteoglycans[42]. It maintains the tissue architecture and stores growth factors and cytokines[42]. The ECM of breast tumors is markedly abnormal. It contains higher amounts of fibrillar type I collagen, which is required for angiogenesis, with architectural changes that promote cancer cell invasion[42,49]. Tenascin C (TNC) and splicing variants of fibronectin are also expressed in tumor ECM and promote angiogenesis[50,51]. Integrins are the major receptors that mediate interactions between ECM and cells in the mammary gland and play an important role in breast tumorigenesis, as has been shown for β1 and β4 integrins[52-54] (Figure 4). Interestingly, the ECM composition correlates with patient outcome[42,46]. Overexpression of protease inhibitors (for example, serpin family members) is associated with good prognosis, while high expression of integrins and metalloproteinases (MMPs) and low expression of several laminins is linked to a poor outcome[42,46].

Breast tumors recruit mesenchymal stem cells (MSCs) from the bone marrow or from normal breast stroma. MSCs secrete several cytokines to stimulate self-renewal of cancer stem cells through the activation of PI3K/AKT and NF-κB pathways[43] (Figure 4). They can also differentiate into adipocytes and tumor-associated fibroblasts (CAFs)[43].

CAFs derived from MSCs or generated by the epigenetic changes induced by cancer cells on the surrounding stromal fibroblasts[43] promote cancer cell growth, angiogenesis and invasion[42-44,55-57]. CAFs are heterogeneous, with a subset of them identified as myofibroblasts expressing alpha smooth muscle actin (αSMA)[58]. CAFs secrete CXCL12 and hepatocyte growth factor (HGF) to promote proliferation of tumor cells that express CXCR4 and c-Met, respectively[58]. CAFs also secrete vascular endothelial growth factor (VEGF), which induces vascular permeability and angiogenesis, and proinflammatory factors that activate NF-κB signaling to promote tumorigenesis[44,46] (Figure 4).

Adipocytes stimulate growth and invasion of breast tumor cells, by secreting leptin, adiponectin, HGF, collagen VI, proteases and proinflammatory cytokines[42,59] (Figure 4). Indeed, obesity has been recently identified as a poor prognosis factor in breast cancer[60].

Endothelial cells and pericytes are essential for the generation of functional new blood vessels (neoangiogenesis), which supply tumors with oxygen and nutrients required for tumor growth. Recently, it has been shown that endothelial cells secrete growth-promoting trophic factors that support cancer cell proliferation and other tumor-promoting functions[44,61] (Figure 4).

Table 2. Tumor-supportive functions of stromal cells.

Cell type	Functions	References
MSCs	Self-renewal of cancer stem cells	43
CAFs	Proliferation of cancer cells, angiogenesis	42-44,46,55-58
Adipocytes	Tumor growth and invasion	42,59,60
Endothelial cells	Angiogenesis, proliferation of cancer cells	44,61
Pericytes	Angiogenesis	44,62
TAMs	Proliferation of cancer cells, angiogenesis, invasion	45,46,63-66
$TIE2^+$ monocytes	Angiogenesis	46,67
Neutrophils	Angiogenesis, invasion, immunosuppression	45,66,68,69
MDSCs	Immunosuppression	45,46,70,71
B cells	Release of pro-tumorigenic cytokines	45,46,63,72
DCs	Immunosuppression	45,46,73
Mast cells	Angiogenesis	74,75
Platelets	Angiogenesis	44,76

Most immune cells show high plasticity and can play tumor-promoting or tumor-suppressive functions[45,46,72]. $CD8^+$ cytotoxic T cells (T_c) and natural killer (NK) cells destroy cancer cells through perforin- and granzyme-mediated apoptosis[45,46] (Figure 4). Macrophages, dendritic cells (DCs) and neutrophils can also play a tumor-suppressive role, however, cancer cells are able to polarize those immune cells into a tumor-promoting state[45]. Tumor-associated macrophages

(TAMs) can secrete a wide range of growth factors such as fibroblast growth factor (FGF2), which directly supports tumor cell proliferation. They can also promote angiogenesis through the secretion of VEGF, prostaglandin E2, FGF2 and IL8, and invasion by the secretion of MMPs and EGF[63-65] (Figure 4). Monocytes expressing TIE2, a receptor for the angiogenic growth factor angiopoietin, promote angiogenesis through a paracrine signaling loop with angiopoietin-expressing endothelial cells[67]. Neutrophils can promote tumor progression by secreting angiogenic factors and ECM-degrading enzymes, and by suppressing the anti-tumor immune response[66,68,69,77] (Figure 4). Myeloid derived suppressor cells (MDSCs) promote tumor progression by inhibiting T_c and NK cells (Figure 4) and inducing polarization of macrophages and DCs into the anti-inflammatory and protumorigenic state. DCs are monocytic antigen-presenting cells that help T_c cells and activation of DCs by MDSCs results in reduced activity of T_c cells[45,46]. B lymphocytes can support tumor progression by secreting protumorigenic cytokines and mast cells activate MMP9 and enhance proliferation of endothelial cells to promote tumor angiogenesis[45,46,63,72]. Platelets can also stimulate angiogenesis through the release of various angiogenesis stimulating factors, such as VEGF and PDGF[76].

1.4. Breast cancer metastasis

Metastasis is responsible for the majority (> 90%) of deaths related to breast cancer. This multistep process requires the dissemination of cancer cells from the primary tumor to distant organs, where they grow and form secondary tumors. This occurs in two major phases: 1) translocation of the cancer cells from the primary tumor to the distant tissue, an event that entails several sequential steps: invasion, intravasation, survival in the bloodstream and extravasation, and 2) colonization of the target organ (Figure 5). This is a very inefficient process in which cancer cells need to overcome the barriers imposed by the organism and the specific constraints dictated by each target organ[78,79].

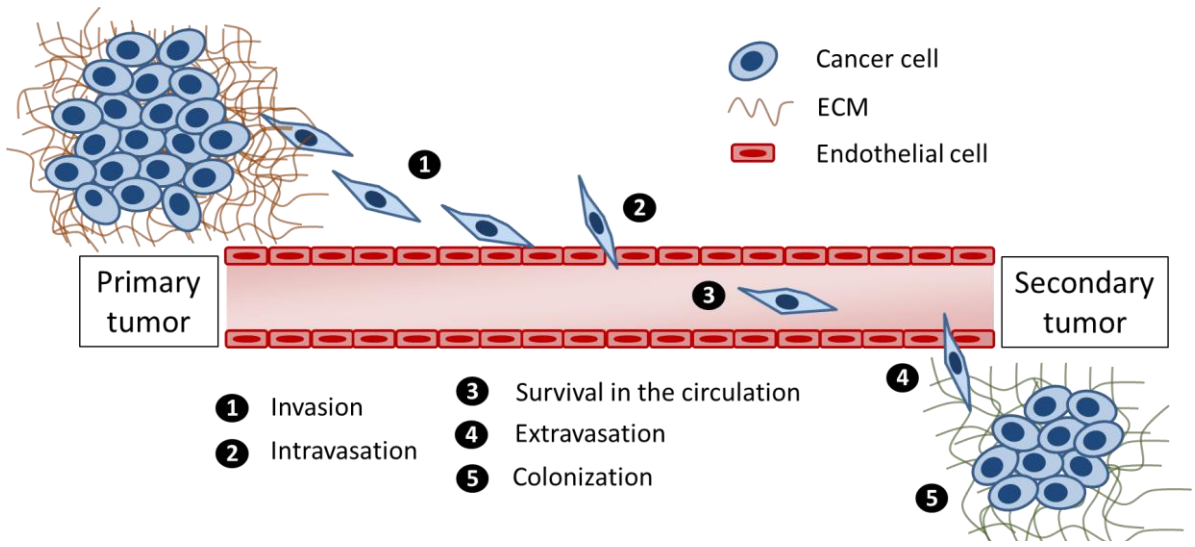

Figure 5. The multistep process of metastasis.

Metastasis, a hallmark of cancer, is an evolutionary process that results from genetic and epigenetic changes in cancer cells as well as microenvironmental cues that modulate tumor cell behaviour[30] (see also section 1.3.2) (Table 3 and Figures 6-7).

In preclinical models, three general classes of metastasis genes have been described: metastasis initiation genes, metastasis progression genes and metastasis virulence genes[80,81] (Figure 6). Metastasis initiation genes provide an advantage in the primary tumor, promoting invasion and intravasation of the cells. Metastasis progression genes exert their functions in both the primary tumor and the target organ. In contrast, metastasis virulence genes participate in colonization but not in primary tumor progression[80,81] (Figure 6).

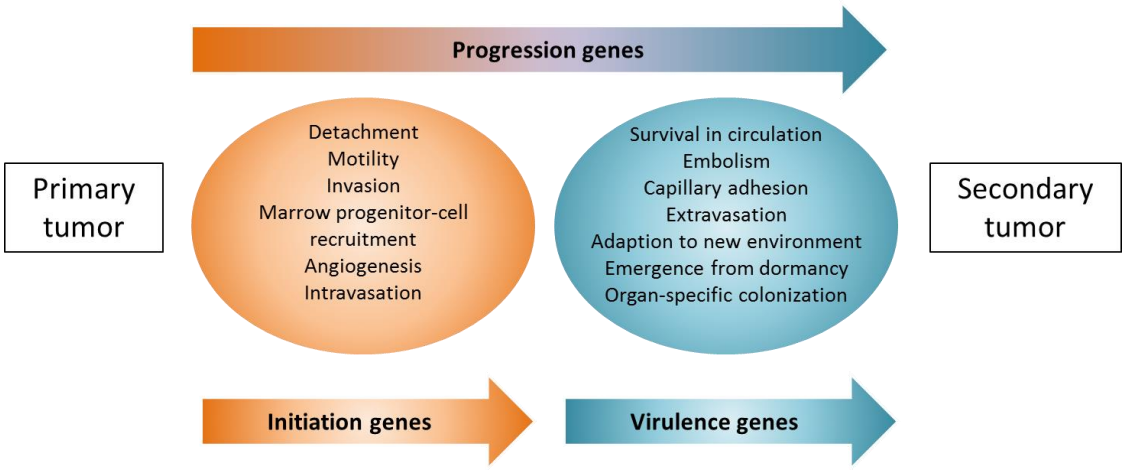

Figure 6. Classification of metastasis genes. Adapted from Nguyen *et al.*[80]

One of the main strategies to search for metastasis genes has been to perform global transcriptomic analysis, comparing parental cell lines to their metastatic subpopulations obtained by *in vivo* sequential passages[82-85].

In clinical models, next-generation sequencing technologies have allowed the comparison of primary and metastatic tumors at the genomic level. Surprisingly, these studies have not revealed metastasis-specific, recurrent, driver mutations. Instead, alterations are found in genes that are commonly mutated in primary tumors[86].

1.4.1. Dissemination of cancer cells to distant organs

1.4.1.1. Invasion and Migration

A major model by which cancer cells are proposed to acquire an invasive phenotype is the so called epithelial-mesenchymal transition (EMT)[87]. In this process, epithelial cells lose their cell polarity and intercellular adhesiveness to become highly motile mesenchymal-like cells. At the molecular level, EMT entails loss of epithelial markers (E-cadherin) and gain of mesenchymal

markers (N-cadherin and vimentin), and occurs upon activation of specific transcription factors (Snail, Twist, Slug, ZEB1, ZEB2)[87-89]. In breast cancer, the core EMT gene signature is associated with the claudin-low molecular subtype[18,87]. In addition, multiple genes promote invasion and metastatic progression without obvious EMT. For example, loss of PAR3 in HER2+ tumors reduced junctional stability and cell cohesion without affecting E-cadherin expression or localization[87,90].

Invasion also requires changes in the ECM and its interaction with cancer cells (see also section 1.3.2). Degradation of the ECM in breast cancer is predominantly mediated by MMPs and the urokinase plasminogen activator (uPA) system[91]. For example, MT1-MMP-expressing breast cancer cells generate micro-tracks that enable migration of trailing cells, and invasion is abolished when MT1-MMP-mediated proteolysis is disrupted[87]. Moreover, in another study lysyl oxidase-like 2 enzyme (LOXL2) promoted invasion of breast cancer cells by regulating the expression and activity of TIMP1 and MMP9[92]. Interaction of uPA with its receptor uPAR activates plasmin, which leads to the degradation of ECM components and the activation of MMPs. Indeed, activation of this system is associated with poor prognosis in breast cancer[91]. Furthermore, introduction of β4 integrin in β4-negative breast carcinoma cells activates signaling from PI3K to Rac and increases the invasive activity of these cells *in vitro*[93].

Migration and invasion also require dynamic cytoskeletal reorganizations and RhoGTPases (mainly Rho, Cdc42 and Rac) have been described as key regulators of these processes[94]. In addition, several other molecules are also involved in this cell motility machinery. For example, it has been reported that RhoA/MRTF-A and JAK/STAT3 signaling pathways synergistically increase migration of breast cancer cells by promoting the expression of migration markers Myl-9 and Cyr-61[95]. In another study, overexpression of podoplanin (a mucin-like protein) in breast cancer cells induced formation of filopodia and cell migration[96]. Recently, SRPK1 (serine/arginine-rich protein-specific kinase 1) has been identified as a breast cancer metastasis determinant through a cell migration screen[97]. Furthermore, stimulation of cAMP through cyclic nucleotide phosphodiesterases was able to inhibit breast cancer cell migration in another model[98].

1.4.1.2. Intravasation

Invasive cancer cells cross the pericyte and endothelial cell barriers and enter into the lumina of lymphatic or blood vessels[99]. Some factors (such as EGF, TGFβ, MENA and NWASP) promote intravasation by increasing breast cancer cell penetration of microvessel walls[99,100]. Other factors, like MMP17 and ADAM12, promote intravasation by disturbing vessel integrity around the primary tumor. In addition, COX2, EREG, MMP1 and MMP2 also promote intravasation of breast cancer cells by stimulating the formation of leaky blood vessels[99,101].

Table 3. Main players involved in the metastatic process in breast cancer.

Category	Function	Molecules	Reference
Invasive motility	EMT	↓ E-cadherin ↑ N-cadherin, vimentin Snail, Twist, Slug, ZEB1, ZEB2	87-89
	↓ Cell cohesion	PAR3 loss	90
	ECM degradation	MT1-MMP, LOXL2, MMP9, TIMP1 uPA-uPAR Cathepsins, MMP2	87,92 91 44,102,103
	Cytoskeletal organization	β4 integrin RhoA/MTRF-A and JAK/STAT3	93 95
	Migration	Podoplanin, SRPK1, cAMP	96-98
Intravasation	Vessel invasion	EGF, TGFβ, MENA, NWASP	100
	Vessel integrity	MMP17, ADAM12 COX2, EREG, MMP1, MMP2	99 99,101
Circulation	Anoikis resistance	CD147, MSLN, IGFBPs	104-106
	Immune evasion	Mucins	72,107
Extravasation	Homing	CXCR4, CXCR7, CXCL12	56,82,108,109
	Vessel barrier opening Transcellular migration	$P2Y_2$ 12(S)hydroxieicosatetraenoic acid Anglptl4 MLC kinase	110 111 112 113
Colonization	Target organ preconditioning	VEGFA, TGFβ, TNFα, LOX	114-116
	Dormancy	uPAR, EGFR, α5β1 BMP, Coco, Src Angpt2	117,118 119,120 121
Bone colonization	Osteolysis	PTHrP, IL6, IL11, IL8, TNFα, RANKL VEGF, OPG, GLI2, RUNX	82,122,123
	Angiogenesis	FGF5, CTGF, TGFβ	82
	Homing	CXCR4	82
Lung colonization	Angiogenesis	EREG, COX2, MMP1, MMP2	84,101
	Tumor initiation	ID1, ID3, TNSC	124,125
	Apoptosis/Survival	VCAM1, CXCL1/2	126,127
	Adhesion and differentiation	RARRES3	128

1.4.1.3. Survival in the circulation

Once in the circulation, cancer cells must overcome shear stress, including physical damage from hemodynamic forces, anoikis (cell death induced by the loss of adhesive supports), and immunosurveillance[79].

CD147, a glycoprotein enriched in the surface of breast cancer cells, confers resistance to anoikis through inhibition of Bim[104]. Mesothelin (MSLN), another glycoprotein, also prevents anoikis in breast cancer cells through the activation of ERK1/2 signaling and Bim suppression[105]. Importantly, the relevance of anoikis in circulating tumor cells is closely related to the time spent by cancer cells in the circulation, which is so far not understood[79,99].

Circulating cancer cells are protected from shear forces and immune cells by platelets, which surround and coat cancer cells through the interaction of P-selectin and mucins present at the surface of platelets and cancer cells, respectively. Tumor cells induce the formation of these aggregates by expressing tissue factor (TF), which initiates the coagulation cascade[62,104].

Metastasis-promoting activity of platelets also involves secretion of TGFβ and induction of NF-κB signaling in cancer cells[129] (Figure 7).

1.4.1.4. Extravasation

Extravasation into a target organ occurs in two steps: 1) attachment of cancer cells to endothelial cells; and 2) transendothelial migration (TEM) or rupture of vessels by tumors grown in their lumen[100].

Attachment of cancer cells to endothelial cells is mediated by E-selectin initially, and by integrins later on. Chemokines are also involved in the regulation of extravasation and homing to specific organs[100] (Figure 7). For instance, CCL2 produced by breast cancer cells interacts with its receptor CCR2 in endothelial cells to increase extravasation and metastasis in the lung[130,131].

Two routes of TEM have been described: paracellular TEM (migration of cancer cells through the interendothelial junctions) and transcellular TEM (migration of cancer cells directly through the body of endothelial cells)[100]. For example, MCF7 breast cancer cells induce retraction of endothelial cells by secreting a lipid (12(S)hydroxieicosatetraenoic acid)[111]. Angiopoietin-like protein 4 (Anglptl4) expressed by breast cancer cells also induces opening of interendothelial junctions[112]. Interestingly, since endothelial cells in the vasculature of different organs express different cell-surface receptors, Anglptl4 did not increase extravasation of the same breast cancer cells to bone[99,132]. Breast cancer cells were also reported to use a transcellular route through the activation of MLC kinase in endothelial cells, leading to phosphorylation of MLC and myosin contraction[113].

1.4.2. Tumor growth in secondary organs

1.4.2.1. Organ tropism

The target organ is determined based on two principles: 1) the vascular architecture and pattern, which can influence the dissemination of cancer cells to the target organ. For example, the sinusoid capillaries in the bone marrow, designed to facilitate the normal trafficking of hematopoietic cells, present little resistance to cancer cell extravasation[78]; and 2) the cancer cell-microenvironment compatibility, also known as the “seed and soil” hypothesis, first established by Stephen Paget, which postulates that only cancer cells (the “seed”) which display functions or capabilities to adapt to and grow in the new microenvironment will colonize the target organ (“the soil”)[132,133]. Therefore, each organ will select the cancer cells more adapted to grow in its microenvironmental conditions.

In breast cancer, bone and lung are the most common metastatic sites, followed by brain and liver[8,99].

1.4.2.2. Premetastatic niche

Primary tumors precondition the microenvironment of the target organ before the arrival of disseminated cancer cells[134]. This adapted microenvironment is called the "premetastatic niche" and is created in response to several factors secreted by the primary tumor[134] (Figure 7). In breast cancer, expression of lysyl oxidase (LOX), a major target of hypoxia-inducible factor (HIF) signaling, can facilitate myeloid cell recruitment and subsequent tumor cell colonization to the lung[114].

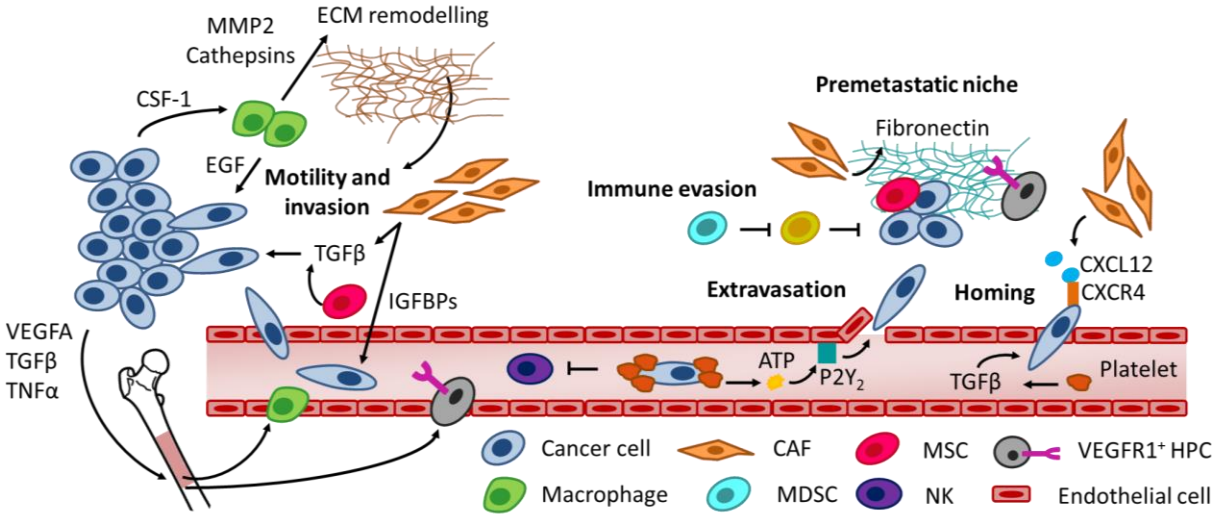

Figure 7. Microenvironmental regulation of metastasis. TAMs facilitate tumor cell invasion through a paracrine signaling loop that involves tumor-derived colony-stimulating factor 1 (CSF-1) and macrophage-derived EGF[47]. TAMs are also a major source of proteases, such as cysteine cathepsins and MMP2, which cleave laminin-5 γ2 chains that mimic EGFR ligands and induce cell motility and invasion[44,102,103]. CAFs secrete TGFβ and insulin-like growth factor-binding proteins (IGFBPs) to induce EMT and inhibit anoikis, respectively[44,106]. Platelets protect cancer cells in the circulation and promote their extravasation through ATP-dependent activation of the endothelial $P2Y_2$ receptor, which opens the vessel barrier[110]. CXCL12 secreted by stromal cells in distant organs (lung, bone) attracts breast cancer cells that express CXCR4 and CXCR7 receptors and stimulates extravasation[56,82,108,109]. Bone marrow (BM)-derived $VEGFR1^+$ hematopoietic cells (HPC) colonize premetastatic sites before tumor cell arrival in response to factors such as VEGFA, TGFβ and TNFα, released by the primary tumor and induce the deposition of fibronectin, which can be a docking site for cancer cells[115,116]. Adapted and modified from Quail *et al.*[46]

1.4.2.3. Dormancy

Once cancer cells have seeded into the target organ, they have to survive, adapt to the new microenvironment and expand to develop macrometastases. Most cancer cells that reach the target organ die within 24 hours of extravasation and adaptation of the survivors to the new microenvironment can take a variable period of time depending on each cancer type[135]. In breast cancer, for example, macrometastases can develop several years after resection of the primary

tumor[8]. This pause in metastasis progression, called dormancy, is mediated by several mechanisms: angiogenic dormancy (insufficient tumor vascularization, balance between proliferation and apoptosis), cellular dormancy (cells are arrested in G0) and immune dormancy (tumor cell division is balanced by the immune system)[46,117,118].

Cellular dormancy or quiescence can be mediated by microenvironmental-mediated signals. For example, loss of uPAR, EGFR or α5β1 integrin from the surface of cancer cells can induce low FAK-Ras-ERK signaling and high Cdc42-p38 activity, leading to cell cycle arrest[117,118]. In breast cancer, bone morphogenetic protein (BMP) signaling maintains cancer cells in a quiescent state, while COCO, a secreted BMP antagonist, reactivates the proliferation of these cells[119]. Once cells emerge from quiescence and the tumor reaches a certain size, tumor growth can be limited due to insufficient vascularization. In this context, tumor size is maintained through a balance between proliferation and cell death, stimulated by nutrient deprivation and hypoxia, for example[46,117,118]. In bone metastasis of breast cancer cells, Src mediates AKT regulation and survival of cancer cells in response to CXCL12 and TNF-related apoptosis inducing ligand (TRAIL)[120]. The ability of cancer cells to respond to hypoxia promotes neovascularization and interrupts angiogenic dormancy, an event also known as the angiogenic switch[117,118]. Consistently, Angpt2 facilitates the metastatic colonization of mammary carcinomas by promoting the capacity of infiltrating myeloid cells to support the vascularization of metastatic nodules[121]. Finally, immune dormancy is mediated by the immunosurveillance mechanisms that have been previously described (Figure 7).

1.4.2.4. Colonization

Several genes associated with specific metastasis to bone[82], lung[84], brain[85] and liver[136] have been identified in breast cancer cells. These genes endow cancer cells with the abilities to overcome the demands imposed by particular foreign tissue microenvironments[99].

Bone colonization

Bone metastases occur in 65-80% of patients with metastatic breast cancer, generating pathological bone fractures, pain, metabolic alterations, and spinal cord and nerve-compression syndromes[122].

Bone, composed of organic and mineralized ECM and specific cell types (osteoblasts, osteoclasts, osteocytes), is a dynamic tissue undergoing constant remodelling with consecutive cycles of bone formation and resorption[122,137]. Breast cancer cells disrupt this balance by inducing changes in the activity of osteoclasts (bone resorption) and/or osteoblasts (bone formation), resulting in typical bone lesions with lytic or sclerotic appearance[122,137]. Human osteolytic breast cancer cells secrete different cytokines such as PTHrP, IL6, IL8, IL11, VEGF and TNF which stimulate RANKL production by osteoblasts and stromal cells. RANKL binding to its receptor

RANK, expressed by osteoclasts, triggers a signaling cascade that leads to the differentiation and activation of osteoclast progenitors into mature osteoclasts that mediate bone resorption[122,123,137] (Figure 8). Consequently, matrix-derived TGFβ and IGF1 growth factors and calcium are released from bone. Growth factors bind to tumor cell receptors and activate signaling pathways such as SMAD and MAPK, whereas calcium activates calcium pump[122,123,137]. Signaling through these pathways promotes tumor cell proliferation and release of PTHrP, which further exacerbates osteoclasts and bone resorption, creating a perpetuated vicious cycle[122,123,137] (Figure 8). Platelet-derived lysophosphatidic acid (LPA) and ADP can also induce the production of IL6 and IL8 by cancer cells (Figure 8). In addition, hypoxia-inducible factor 1α (HIFα) in conjunction with TGFβ can increase tumor production of VEGF and CXCR4 to increase angiogenesis and tumor homing[122,123,137] (Figure 8). MMPs have also been implicated in osteolysis by increasing amounts of active RANKL, through cleavage of RANKL and EGF-like ligands that further decrease osteoprotegerin (OPG) and subsequent RANKL sequestration[122,123,137] (Figure 8). Jagged-1 (JAG1) expressed in breast cancer cells activates Notch signaling in bone cells, inducing IL6 production that further participates in osteolysis and promotes cancer cell proliferation (Figure 8). GLI2 and RUNX2 transcription factors are also involved in osteolysis, inducing PTHrP and MMP9 expression, respectively[122,123,137] (Figure 8). Interestingly, MDSCs can also respond to RANKL to form mature osteoclasts and promote osteolysis in murine models of breast cancer[138].

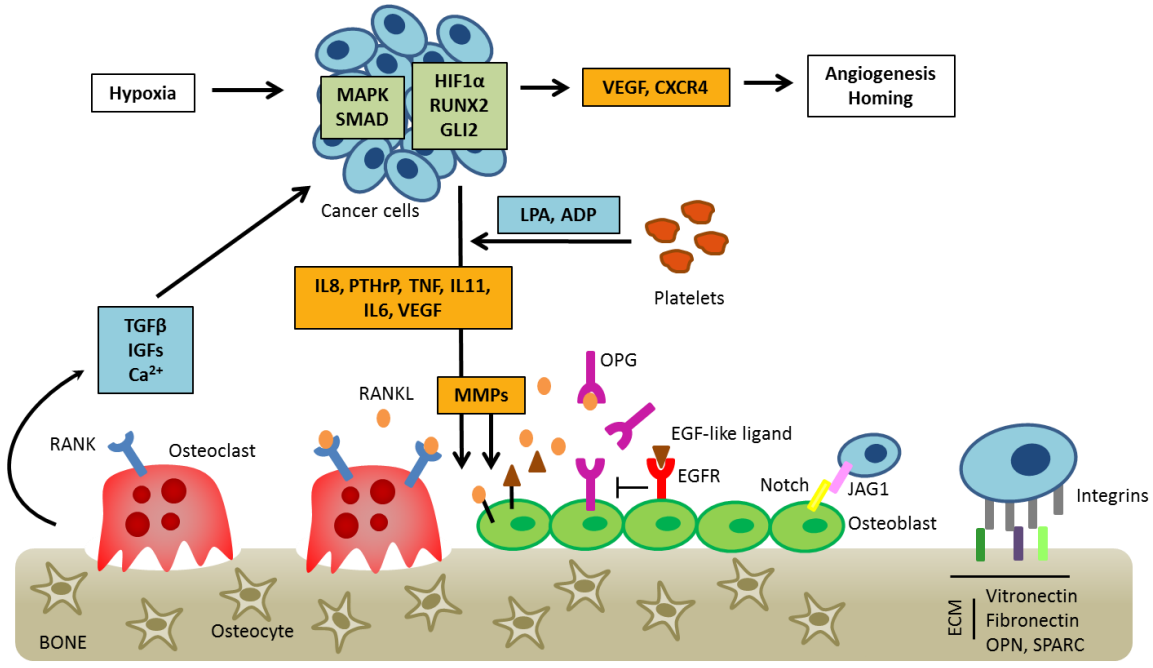

Figure 8. Bone colonization and the osteolytic "vicious cycle". Adapted from Weilbaecher *et al.*[122]

Cancer cells also interact with ECM and other cell types present in the skeleton. Breast cancer cell surface αvβ3 integrin interacts with bone-derived osteopontin (OPN), fibronectin, vitronectin

and SPARC (secreted protein acidic and rich in cysteine) and β1 integrin family members interact with fibronectin, collagen I and VCAM1 in the bone marrow stroma (Figure 8). These interactions further promote bone colonization of breast cancer cells[122,123,137]. Bone marrow also contains MSCs and adipocytes, which also promote bone colonization through similar mechanisms[138].

Consistently, the bone metastasis promoting gene signature described by Kang *et al.*[82] included genes involved in bone marrow homing and extravasation (CXCR4), pericellular proteolysis and invasion (MMP1, ADAMTS1), angiogenesis (FGF5 and CTGF) and osteoclastogenesis (IL11). Functional analyses also revealed that IL11, CTGF, CXCR4 and OPN had a causal role in osteolytic metastasis[82].

Lung colonization

Transcriptomic comparison between parental and lung-metastatic breast cancer cells identified several genes highly enriched in cells able to metastasize to the lungs[84]. These genes include: secreted factors (EREG, CXCL1, SPARC), cell surface receptors (VCAM1, IL13Rα2), extracellular proteases (MMP1 and MMP2), and intracellular effectors (ID1 and COX2)[79,84]. Significantly, the expression of these genes correlated with lung metastatic relapse in a cohort of breast cancer patients[79]. Interestingly, the lung metastasis genes identified in this study were largely distinct from genes previously associated with metastasis to bone, reflecting that different functions are necessary to colonize the distinct lung and bone microenvironments[79].

Importantly, the implication of some of these genes in lung mestastasis has been validated in several *in vivo* models. For example, one study showed that EREG, COX2, MMP1 and MMP2 cooperate to mediate tumor angiogenic progression and extravasation of breast cancer cells to seed pulmonary metastases[101]. In another study, transcriptional inhibitors of differentiation ID1 and ID3 were required for tumor initiating functions of TN breast cancer cells, both in the primary tumor and during lung colonization[125]. It has been reported that expression of TNC by breast cancer cells enhances stem cell signaling in metastasis-initiating cells to support lung colonization[124]. VCAM1 can also promote lung metastasis through AKT activation and apoptosis prevention upon interaction with integrins at the surface of macrophages[127]. Notably, VCAM1 was also able to promote osteolytic bone metastasis in an experimental metastasis model[139]. CXCL1/2 could also increase lung metastasis by recruiting myeloid cells to metastatic sites, which secrete cytokines to enhance cancer cell survival[126]. RARRES3 was also shown to suppress breast cancer lung metastasis by regulating adhesion and differentiation[128].

2. ENDOTHELIAL PROTEIN C RECEPTOR (EPCR)

2.1. EPCR structure and localization

EPCR is a protein of 238 amino acids and approximately 46 kDa, encoded by the human EPCR gene (*PROCR*), which is located on chromosome 20q11.2 and consists of four exons and three introns[140,141]. EPCR is a type 1 transmembrane protein with sequence and 3D structural homology with the major histocompatibility class 1 (MHC)/CD1 family of proteins, particularly CD1d[140,142]. It contains an extracellular region, a transmembrane region and a short cytoplasmatic tail. The extracellular region consists of an eight-strand β-sheet and two anti-parallel α-helical domains (α1 and α2), which fold forming a hydrophobic groove that is occupied by a lipid[140,142]. It also contains four potential N-glycosylation sites[143] (Figure 9). Phosphatidylcholine (PCh) is the major phospholipid bound to human EPCR and it is required for ligand binding. EPCR can also bind lysophosphatidylcholine and platelet-activating factor (PAF), generated by the enzymatic action of secretory group V phospholipase A2. However, they impair the ability of EPCR to interact with its ligands protein C (PC) and factor VII (FVII)[144]. The cytoplasmatic tail only contains three aminoacids (Arg-Arg-Cys)[140] and can be palmitoylated, which contributes to the membrane localization and intracellular trafficking of EPCR[145-147].

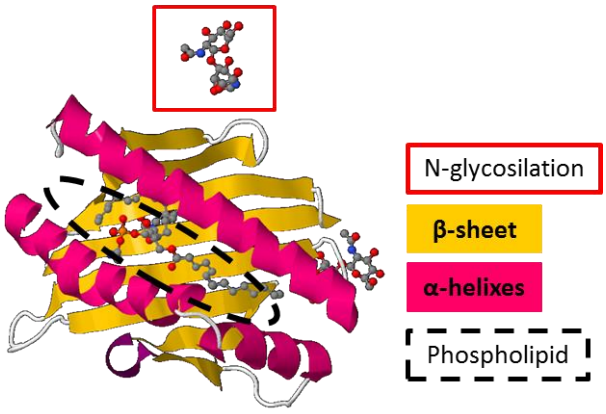

Figure 9. EPCR structure. Only the extracellular domain is represented. Adapted from 1L8J, PDB. Deposited by Oganesyan V *et al.*[142]

The majority of EPCR on cells is localized on the cell surface in lipid rafts positive for caveolin-1 (CAV1)[145]. A small fraction is also localized in the recycling compartment, since ligand binding to EPCR promotes its endocytosis[145]. EPCR can also be shed from the cell surface, at least in part by TACE/ADAM17-mediated cleavage between 192-200 amino acids[148]. The sensitivity of EPCR to this cleavage is increased when Ser-219 in the transmembrane domain of EPCR is substituted by glycine[149]. EPCR shedding generates a soluble form of EPCR (sEPCR)[150] that retains the ability to bind PC/APC and FVII/FVIIa[151,152].

EPCR expression was first reported in endothelial cells, mainly in large blood vessels[151,153,154]. More recently, it has been shown that EPCR is also expressed in monocytes[155,156], neutrophils[157], smooth muscle cells[158], keratinocytes[159], placental trophoblasts[160], cardiomyocytes[161], osteoblasts[162], chondrocytes[163], fibroblasts[164], and hematopoietic[165,166], neuronal[167] and mammary[168] progenitor cells.

2.2. EPCR ligands

2.2.1. PC/APC and FVII/FVIIa

EPCR was originally identified as a receptor for PC and activated protein C (APC), which bind EPCR with similar affinity[140,151]. This interaction occurs between the N-terminal γ-carboxyglutamic acid rich (Gla) domain of PC/APC and α chains of EPCR, in presence of calcium and magnesium ions[143,151,169]. All residues of the PC/APC Gla domain involved in modulating EPCR binding are fully conserved in FVII/FVIIa and it has been shown that FVII/FVIIa bind EPCR with a similar affinity as PC/APC[170-172]. In addition, whether factor X (FX) and FXa bind EPCR is an issue of controversy and remains an open question[147,173]. Interestingly, murine PC/APC bind murine EPCR, whereas murine FVII/FVIIa do not[174,175]. Importantly, murine PC/APC and FVII/FVIIa can bind human EPCR[147,173].

More recently, novel EPCR ligands have been found: proteinase-3/Mac-1, γδ T-cell antigen receptor and *Plasmodium falciparum* erythrocyte membrane protein I[147,176].

2.2.2. Proteinase-3/Mac-1

On the surface of neutrophils, sEPCR binds to heterocomplexes formed by proteinase-3 (PR3) and Mac-1 (also known as Cd11b). Antibodies that block APC-EPCR binding were not able to impair sEPCR binding to neutrophils, suggesting that the region of EPCR involved in this interaction is distinct from the APC binding site[177]. Interestingly, PR3 is able to cleave and degrade EPCR[178]. Also, human monocytes bind to sEPCR and endothelial cells directly through Mac-1. This interaction was inhibited by APC and antibodies that block APC-EPCR binding[179].

2.2.3. γδ T-cell antigen receptor

A specific T cell antigen receptor ($V_\gamma 4V_\delta 5$) was able to bind to the β-sheet of EPCR independently of glycosylation and lipid binding status of EPCR. This interaction allowed T cells to recognize both endothelial cells targeted by cytomegalovirus and epithelial tumors[180,181].

2.2.4. *Plasmodium falciparum* erythrocyte membrane protein I (PfEMP1)

In malaria, sequestration of *Plasmodium falciparum*-infected erythrocytes in blood vessels occurs through the interaction of the members of the PfEMP1 family with receptors on the vascular endothelium. PfEMP1 subtypes containing domain cassettes (DCs) 8 and 13 are associated with

severe malaria. Recently, EPCR was identified as the endothelial receptor for DC8 and DC13 PfEMP1. Interestingly, PfEMP1 bound EPCR near or at the same region as APC[182-185].

2.3. EPCR signaling and functions

2.3.1. Regulation of coagulation

EPCR enhances the activation of PC by the thrombin (IIa)-thrombomodulin (TM) complex on the surface of endothelial cells, by lowering K_m for the activation[186]. When APC dissociates from EPCR and binds to phospholipid membranes exerts anticoagulant activity. It inactivates FVa and FVIIIa, assisted by cofactors protein S (PS) and FV, leading to reduced thrombin formation[187-189] (Figure 10). Some studies have shown that FVIIa binding to EPCR has no effect on FVIIa activation of FX[170,190], while another study revealed that EPCR attenuates TF-FVIIa activation of FX[172]. At present, the phsysiological significance of EPCR interaction with FVIIa in hemostasis remains unclear[147].

2.3.2. Cytoprotection

When APC remains bound to EPCR, it cleaves and activates protease-activated receptor 1 (PAR1) and mediates cytoprotective processes, such as anti-inflammatory and anti-apoptotic activities, and endothelial barrier stabilization[189,191,192] (Figure 10). APC downregulates proapoptotic p53 and Bax proteins and stabilizes anti-apoptotic Bcl-2 protein levels[193]. It also inhibits activation of caspase-3 and caspase-8, preventing apoptosis of endothelial cells[193,194] (Figure 10). APC modulates the release of inflammatory mediators (downregulates IL6, MCP-1 and TNFα and upregulates IL10) and downregulates vascular adhesion molecules, reducing leukocyte adhesion and infiltration of tissues[155,195-197] (Figure 10). Barrier stabilization results from APC-induced sphingosine kinase-1 (SK1) stimulation, which phosphorylates sphingosine to produce sphingosine-1-phosphate (S1P). Activation of sphingosine-1-phosphate receptor 1 (S1P1) by S1P reduces endothelial permeability and stabilizes the cellular cytoskeleton by modulating Rac1, and PI3K and ERK signaling pathways[198,199] (Figure 10). In addition, APC stimulates Ang1/Tie2 axis on endothelial cells, leading to SK1 activation and barrier protection[200]. Upregulation of zonula occludens-1 (ZO-1) and VE-cadherin has also been implicated in this function[201].

PAR1 was originally identified as a thrombin receptor[202]. It is a G-protein coupled transmembrane receptor that carries its own ligand, which remains cryptic until unmasked by receptor cleavage[203]. Thrombin induces proinflammatory responses and apoptosis, and enhances the barrier permeability in endothelial cells. Since thrombin activates PAR1 much more efficiently than APC, and thrombin is needed to produce APC, how APC could induce relevant PAR1-mediated signaling and opposite responses, has remained unclear[147,173].

It was suggested that the differences in PAR1-mediated signaling between thrombin and APC could be explained by the inability of thrombin to transactivate S1P1[199]. In the same line, differences in transactivation of PAR2 and PAR3 by thrombin- and APC-activated PAR1 could also have an influence. For example, PAR1 activation by APC does not stimulate the transactivation of PAR2 observed with thrombin[189]. Other studies demonstrated that co-localization of EPCR and PAR1 in caveolae or CAV1-rich membrane microdomains was necessary for selective PAR1 signaling by APC[204-206]. Subsequent work suggested that occupancy of EPCR by APC determines the type of PAR1 response rather than the protease type that cleaves PAR1[207-209]. APC occupancy of EPCR leads to the dissociation of EPCR from CAV1 and couples PAR1 to $G_{i/o}$ instead of G_q and/or $G_{12/13}$, switching the signaling specificity of thrombin from a permeability-enhancing to a barrier-protective response[207,210]. However, recent studies indicate that APC-activated PAR1 cytoprotective signaling is mediated by β-arrestin recruitment and activation of disheveled-2 (Dvl-2) scaffold in caveolar microdomains, leading to Rac1 activation, which inhibits activation of NF-κB and mediates cytoprotective effects[211]. In contrast, thrombin-activated PAR1 couples to G proteins, leading to RhoA and NF-κB activation[211] (Figure 10).

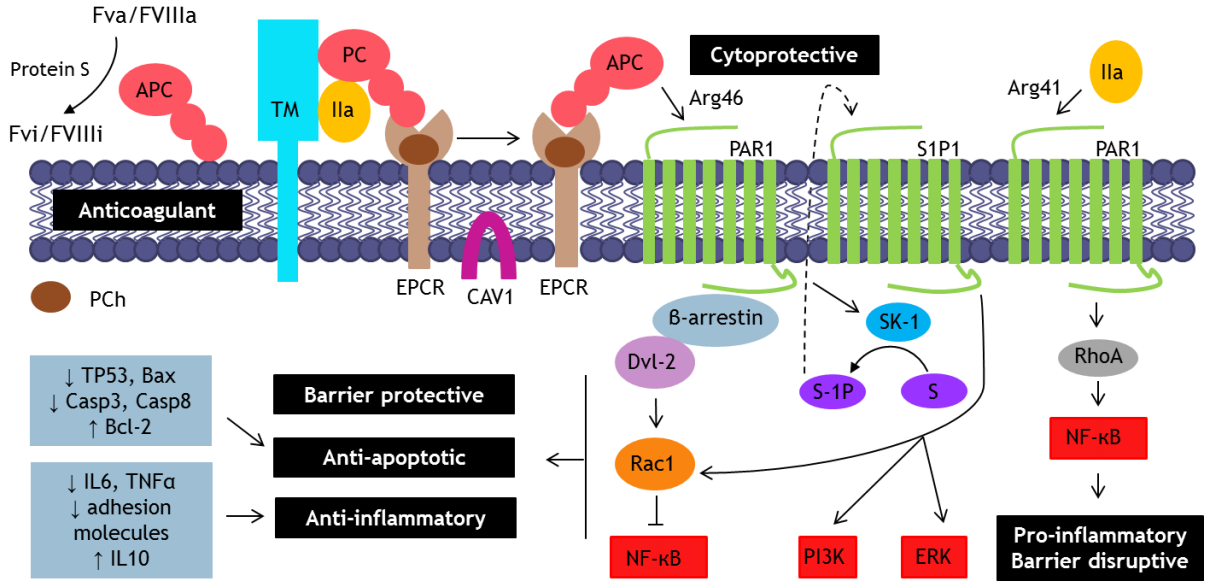

Figure 10. Anticoagulant and cytoprotective signaling through APC-EPCR. EPCR enhances production of APC on the surface of endothelial cells, which inhibits coagulation factors FVa and FVIIIa. EPCR-bound APC cleaves PAR1 at Arg46 and inhibits NF-κB, leading to barrier protection and anti-apoptotic and anti-inflammatory functions. In contrast, thrombin activates NF-κB through cleavage of PAR1 at Arg41, leading to pro-inflammatory and barrier disruptive functions[146,147,212].

Another important discovery was the non-canonical cleavage of PAR1 by APC[213,214]. Thrombin cleaves PAR1 at the canonical Arg41 site, while APC cleavage is produced predominantly at

Arg46[212,213] (Figure 10). Activation of PAR1 at different sites, generating different tethered ligands, probably results in different PAR1 conformations that activate different signaling pathways[147]. It has been shown that thrombin-cleaved PAR1 is rapidly internalized, while APC-activated PAR1 remains on the cell surface[215]. This could explain how APC-PAR1 signaling can be relevant in the presence of thrombin[189].

EPCR-FVIIa also activates PAR1 with the same efficiency as APC, leading to barrier protection. However, the mechanisms mediating this effect remain unknown[147].

2.3.3.Cell stemness

In breast, EPCR has been identified as a marker of multipotent murine mammary stem cells (MaSCs). These $EPCR^+$ cells (accounting for 3-7% of basal cells) exhibited EMT characteristics and enhanced colony-forming ability[168]. In another study, EPCR was shown to be necessary for cell organization and growth of human mammary epithelial cells in 3D culture[216].

2.4. Role of EPCR in cancer

EPCR is expressed in several human cancer cell lines and tumor biopsies, including lung[217], breast[218], ovarian[219] and colon[220] cancer, leukemia[188], glioblastoma[188] and mesothelioma[221].

APC was able to decrease adhesion to endothelium and transmigration of B16-F10 melanoma cells[222]. Moreover, transgenic EPCR-overexpressing mice showed reduced metastasis to lung and liver compared to wild-type (WT) mice. Consistently, APC treatment in WT mice reduced metastasis compared to non-treated mice[222]. Since B16-F10 melanoma cells do not express EPCR, it is concluded that the effects observed were mediated by APC-EPCR signaling in endothelial cells, which led to endothelial barrier protection and reduced metastasis.

In contrast, a study from our group revealed that APC was able to trigger anti-apoptotic signaling in lung cancer cells, through AKT and ERK activation[217]. *In vivo*, silencing of EPCR expression or blocking APC-EPCR binding resulted in reduced prometastatic activity. Since lung tumor cells express EPCR, APC was mediating on tumor cells effects that could overcome the barrier stabilization activity of APC on endothelial cells. Consistently, overexpression of EPCR in other cell lines led to increased metastatic activity. More importantly, EPCR expression correlated with poor prognosis in early stage lung cancer patients[217].

Similarly, EPCR expression correlates with tumor size, lymph node metastasis and TNM stage in lung cancer[223]. In addition, EPCR silencing inhibits cell growth and migration of H1299 lung cancer cells[224]. More recently, it has been shown that EPCR promotes proliferation and migration of MGC803 gastric cancer cells through ERK1/2 activation[225].

In ovarian cancer, plasma levels of sEPCR were positively correlated with CD3 and CD8 levels (markers of Tc cells) and negatively with CD56 levels (marker of NK cells)[219]. These findings

together with the observation of EPCR interaction with a γδ T-cell antigen receptor, implicate EPCR in immunosurveillance.

In another study, EPCR enhanced apoptosis and opposed malignant pleural mesothelioma (MPM) growth driven by TF. Overexpression of EPCR in MPM cells attenuated their growth potential, while EPCR silencing increased their tumorigenicity[221].

In breast cancer, EPCR has been described as a cancer stem cell marker[226,227]. EPCR deficiency attenuates spontaneous breast cancer growth in the polyoma middle T (PyMT) breast cancer model. FACS-sorted mfp-MDA-MD-231 (mammary fat pad enhanced MDA-MB-231) $EPCR^+$ cells showed stem cell-like properties and enhanced tumor-initiating activity, an effect inhibited by APC-EPCR blocking antibodies[227]. Another study showed that overexpression of EPCR in mfp-MDA-MB-231 cells increased tumor growth in the initial stage of tumor progression. However, at the end of the experimental period, tumor size was lower in mice injected with EPCR-overexpressing cells compared to control cells, an effect partially explained by a significant reduction in macrophage infiltration and angiogenesis[228]. In addition, some *in vitro* experiments revealed that APC promotes motility and invasion of MDA-MB-231 cells by activating MMP2 and MMP9, and ERK, AKT and NF-κB signaling pathways[218,229].

II Hypothesis and Objectives

HYPOTHESIS

EPCR was identified as a poor prognosis factor in early stage lung cancer patients in previous studies in our laboratory. In addition, anti-apoptotic APC-EPCR signaling in lung cancer cells enhanced their dissemination to several organs, including the skeleton, in various murine models of metastasis.

Bone represents a preferential organ of metastasis in breast cancer. Furthermore, skeletal metastases are associated with osteolytic lesions, an event also observed in lung cancer metastasis.

Based on the previous statements, we hypothesized that EPCR could be a clinically relevant factor that promotes primary tumor growth and metastasis in breast cancer.

OBJECTIVES

To validate this hypothesis, we established the following objectives:

1. Evaluation of the clinical relevance of EPCR in breast cancer.
2. Functional characterization of EPCR in breast cancer cells *in vitro*.
3. Evaluation of the protumorigenic and prometastatic activity of EPCR in murine models of breast cancer.
4. Identification of the cellular and molecular mechanisms mediating EPCR effects.

III Materials and Methods

1. REAGENTS AND MATERIALS

All flasks, plates, dishes, pipettes, tubes and scrapers used are from BD Falcon™ and Costar®/Corning® (Corning, NY, USA).

All chemical reagents are from Sigma-Aldrich (St. Louis, MO, USA) unless otherwise specified.

Water for molecular biology (Sigma-Aldrich) was used for all techniques involving DNA. RNase-free water was obtained after autoclaving water for molecular biology that had been treated with 0.1% diethylpyrocarbonate (DEPC) at room temperature overnight.

All materials used for western blot (Mini-Protean 3® Cell, Mini Trans-Blot® Cell, accessories and nitrocellulose membrane) are from Bio-Rad (Hercules, CA, USA).

Antibodies are specified in each section and references are listed in Appendix 4.

Kits and other reagents and their references are listed in Appendix 4.

1.1. Activated protein C (APC)

We used a recombinant version of the natural APC, marketed as Xigris® by Eli Lilly (Indianapolis, IN, USA). Aliquots were stored at -80ºC and thawed for each experiment. This drug was licensed for the treatment of severe sepsis and septic shock but it was withdrawn in 2011 due to the negative results obtained in the PROWESS-SHOCK clinical trial[230].

1.2. Anti-EPCR RCR252 and F(ab')$_2$ RCR252 antibodies

The antibodies were produced and purified at the Thrombosis and Haemostasis Laboratory at CIMA, by Eva Molina and José Hermida. RCR252 is a monoclonal rat antibody (IgG1 isotype), derived from an hybridoma produced by the fusion of mouse SP2/0 myeloma cells and cells isolated from the superficial inguinal lymph nodes from Wistar rats inoculated with human EPCR$^+$ RE-1 cells[153]. It is specific to human EPCR and blocks APC-EPCR binding. F(ab')$_2$ RCR252 antibody was generated by digesting 2 mg of whole-body antibody with 125 µl of pepsin immobilized on agarose (Pierce) in 20 mM sodium acetate buffer (pH 2.8), at 37ºC in a stirring bath for 1 h. After centrifugation at 1,500 g for 10 min, the supernatant containing F(ab')$_2$ RCR252 was collected with 1 M Tris, pH 9. The efficiency of this process was monitored by SDS-PAGE in non-reducing conditions showing a 110 kDa band. Functional binding of antibodies to EPCR was demonstrated by Surface Plasmon Resonance (Biacore, GE Healthcare).

1.3. Anti-EPCR RCR1 antibody

It was produced and kindly provided by Dr. Kenji Fukudome (Saga Medical School, Japan). It is an IgG1 isotype antibody that recognizes murine EPCR.

2. CELL CULTURE

2.1. Cell lines

MDA-MB-231

This human breast adenocarcinoma cell line was isolated from a pleural effusion of a 51 years old patient, several years after the resection of the primary tumor[231]. It is classified as a claudin-low TN cell line. It was purchased from the American Type Culture Collection (ATCC HTB-26) and authenticated by sequencing of distinctive mutations in TP53 (c.839G>A) and KRAS (c.38G>A) and detection of a partial deletion in CDKN2A, according to COSMIC database from the Wellcome Trust Sanger Institute.

1833

This is a bone metastatic subpopulation derived from the human cell line MDA-MB-231. 1833 was obtained by *in vivo* selection of bone metastatic cells, after intracardiac inoculation of MDA-MB-231 cells into immunodeficient mice, subsequent isolation of cells from bone metastases, *ex vivo* expansion and reinoculation into the left cardiac ventricle of a new subset of mice. Isolation of bone metastatic cells from these mice (2nd passage) yielded the 1833 subpopulation, which has preferential tropism to bone[82] (Figure 11). 1833 cell line was a kind gift from Dr. Gomis (IRB, Barcelona, Spain) with the authorization of Dr. Massagué (Memorial Sloan-Kettering, NY, USA). It was authenticated using the same approach as for the MDA-MB-231 cell line.

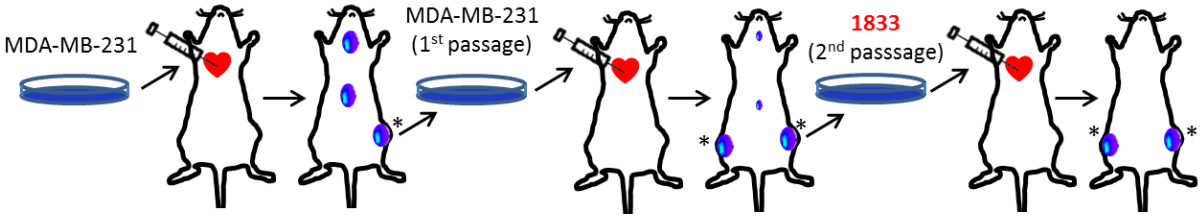

Figure 11. **Isolation of 1833 cells**. Adapted from Kang *et al.*[82] *Bone metastases are shown only in hindlimbs, but 1833 cells also metastasize to other skeletal elements.

MMC

Mouse mammary carcinoma (MMC) cell line is an epithelial cell line established from a spontaneous tumor developed in a Neu-transgenic FVB/N mouse[232]. It was kindly provided by Dr. Santisteban (Clínica Universidad de Navarra, Pamplona, Spain).

ANV

Antigen-negative variant (ANV) cell lines were originally derived from relapsed tumors after subcutaneous inoculation of MMC cells into non-transgenic FVB/N mice[233] (Figure 12). These

cells have undergone EMT and display a mesenchymal-like phenotype[234]. They were generously provided by Dr. Santisteban (Clínica Universidad de Navarra, Pamplona, Spain).

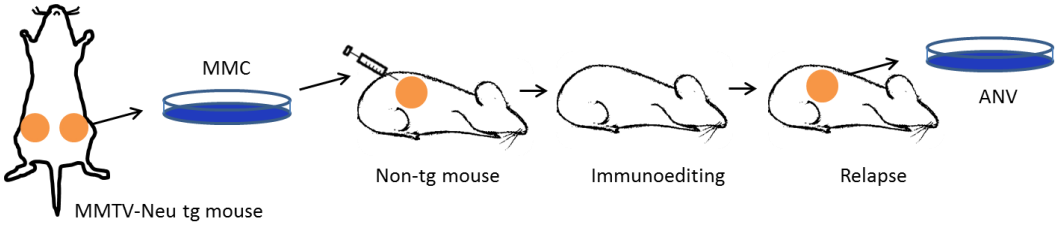

Figure 12. Isolation of MMC and ANV cells. Tg, transgenic.

Amphopack 293

A human embryonic kidney derived cell line transformed with adenovirus type 5 DNA. It contains the viral genes *gag*, *pol* and *4070A env*, and it is used for the production of high-titer replication-incompetent retroviruses. It was obtained from Clontech (631505).

HEK 293T

A human embryonic kidney derived cell line transformed with adenovirus type 5 DNA, that also expresses simian virus 40 (SV-40) large T antigen. It allows replication of plasmids containing the SV40 origin of replication, resulting in enhanced expression of the gene of interest on the plasmid. It was obtained from the ATCC (CRL11268).

ST2

A murine bone marrow stromal cell line established from Whitlock-Witte type long term bone marrow culture of BC8 mice[235]. It was a generous gift from Dr. Civitelli (Washington University, St. Louis, USA).

WI38

A human fibroblast cell line derived by Leonard Hayflick from normal embryonic (3 months gestation) lung tissue. It was obtained from the ATCC (CCL-75).

Panel of human breast cancer cell lines

We used a panel of breast cancer cell lines to study EPCR expression (Figure 19). MCF7, T47D, BT474 and SKBR3 were from Dr. Gomis laboratory (IRB, Barcelona, Spain). CAMA-1, ZR-7530 and BT549 were kindly gifted by Dr. Martínez-Climent (CIMA, Pamplona, Spain).

Luminal A: MCF7 (ATCC HTB-22), T47D (ATCC HTB-133), CAMA-1 (ATCC HTB-21).

Luminal B: ZR-7530 (ATCC CRL-1504), BT474 (ATCC HTB-20).

TN claudin-low: BT549 (ATCC HTB-122), MDA-MB-231 (ATCC HTB-26).

HER2+: SKBR3 (ATCC HTB-30).

2.2. Culture media

MDA-MB-231, 1833, ST2, WI38, HEK293T and Amphopack 293 cell lines were cultured in Dulbecco's Modified Eagle's Medium (DMEM) (Sigma-Aldrich). It contains 4500 mg/L glucose (high), L-glutamine, sodium pyruvate, and sodium bicarbonate.

MMC and ANV cell lines were cultured in RPMI 1640 (Lonza) supplemented with 10 mM HEPES (Lonza), 1% GlutaMAX™ (GIBCO) and 1 mM sodium pyruvate (Lonza).

Medium was supplemented with 10% heat-inactivated (30' at 56°C) fetal bovine serum (FBS) (GIBCO), 100 units/ml penicillin and 100 µg/ml streptomycin (GIBCO). It is referred to as complete medium from now on.

2.3. Culture maintenance

Cells were maintained in complete medium, in a humidified incubator with 5% CO_2, at 37°C. When cells reached 90% confluence, medium was discarded and cells were washed twice with DPBS (Sigma-Aldrich) and incubated with 0.25% trypsin-EDTA (1X) (GIBCO) for 5 min at 37°C. Trypsin-EDTA was neutralized adding the same volume of pre-warmed complete medium and cells were pelleted by centrifugation at 300 g for 5 min. The supernatant was discarded, and cells were resuspended in complete medium and seeded in new flasks. Amphopack 293 cells were cultured in coated plates treated with 30 µg/ml collagen (Inamed Biomaterials), 10 µg/ml fibronectin (Corning) and 100 µg/ml BSA (Sigma-Aldrich) in serum-free DMEM for 30 min at room temperature.

Cells were regularly tested for Mycoplasma infection using MycoAlert™ Mycoplasma Detection Kit (Lonza), following manufacturer's instructions. All experiments were performed in cells negative for Mycoplasma.

2.4. Cell freezing

Cells were frozen in FBS containing 10% DMSO (Sigma-Aldrich) and stored at -80°C or liquid nitrogen (-196°C).

2.5. Cell thawing

Vials of frozen cells were transferred to a 37°C water bath. Cells were rapidly thawed diluted into pre-warmed medium and centrifuged at 300 g for 5 min. The supernatant was discarded to eliminate DMSO and cells were gently resuspended in complete medium and seeded.

3. ESTABLISHMENT OF CELL LINES WITH LUCIFERASE ACTIVITY

Cells with luciferase activity were used for all *in vivo* and co-culture experiments.

3.1. Plasmids

pSFG-Nes-TGL was a kind gift from Dr. Ponomarev (Memorial Sloan-Kettering Cancer Center, NY, USA). This vector contains a triple fusion gene composed of GFP (for FACS sorting), firefly luciferase (for *in vivo* or *in vitro* luminescence measurements) and thymidine kinase (HSV1-tk, for *in vivo* nuclear imaging)[236] (Figure 13A).

pMD2.G was obtained from Addgene (#12259). It contains the viral VSV-G envelope glycoprotein (Figure 13B).

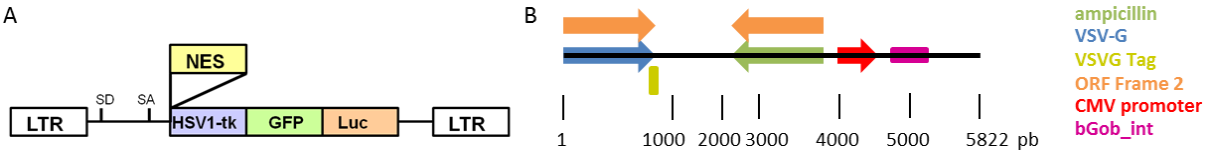

Figure 13. Plasmid maps. A. Linear map of pSFG-Nes-TGL plasmid. From Ponomarev *et al.*[236] B. Linear map of PMD2.G plasmid, adapted from www.addgene.org.

3.2. Production of retroviral particles containing pSFG-Nes-TGL plasmid

Retroviral particles were produced using X-tremeGENE HP DNA Transfection Reagent (Roche). This solution is composed of a proprietary blend of lipids and other components supplied in 80% ethanol. Amphopack 293 cells were seeded into 6-well plates at 600,000 cells/well in complete DMEM. After 24 h, medium was removed and Opti-MEM I (1X) Reduced Serum Medium (GIBCO) with 10% FBS (no antibiotics) was added to the cells. For the production of retroviral particles, the following mixture was prepared (amounts per well): 250 µl of antibiotics- and serum-free Opti-MEM, 2 µg of pSFG-Nes-TGL, 0.8 µg of pMD2.G and 9 µl of X-tremeGENE HP DNA Transfection Reagent. The mixture was incubated at room temperature for 15 min and added drop wise to the cells. Supernatants were collected after 48 h, centrifuged at 300 g for 5 min and filtered through cellulose acetate filters with 0.45 µm pores (VWR International). Viral particles were stored at -80°C.

3.3. Cell infection

1833 and ANV5 cells were seeded in 6-well plates one day before the infection. For the infection, 300 µl of viral particles were added per well, in the presence of 8 µg/ml polybrene (Sigma-Aldrich) to improve infectiveness. After 48 h, medium was replaced and cells were expanded for Fluorescence Activated Cell Sorting (FACS) of infected cells.

3.4. Sorting of infected cells

Cells were washed with DPBS, trypsinized and resuspended at 2 x 10^7 cells/ml in cell sorting buffer (Ca/Mg^{2+} free-DPBS with 1 mM EDTA, 25 mM HEPES, 0.5% heat-inactivated FBS and 1% penicillin-streptomycin). Infected cells were sorted based on GFP expression using a FACSAria II cytometer (BD Biosciences), in the Flow Cytometry Facility at CIMA. Sorted cells (>95% GFP^+) were expanded and frozen.

4. GENERATION OF CELLS WITH STABLE EPCR SILENCING

Control (Vector and shControl) and EPCR-silenced cell lines were generated from cells previously transduced with luciferase, as described in section 3.

4.1. shRNAs

shRNAs cloned into PLKO.1-puro vector and the empty vector (SHC001) were obtained from Mission® (Sigma-Aldrich), as bacterial glycerol stocks. Plasmid map and shRNA sequences are shown in Figure 14. shControl is a scramble shRNA that does not target any known human and mouse genes. shEPCR#1 and shEPCR#2 target human EPCR, while shEPCR#3 and shEPCR#4 target murine EPCR.

A

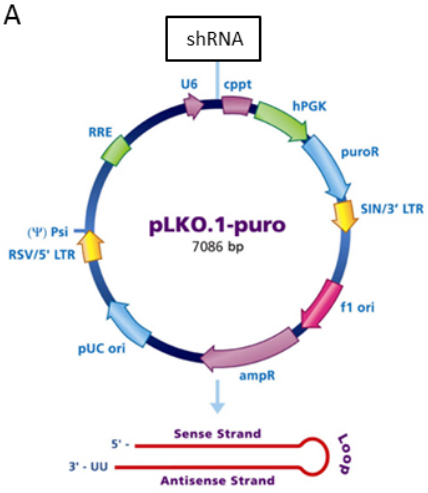

B

shRNA	Sequence (5'→ 3')
shControl (SHC002)	CCGGCAACAAGATGAAGAGCACCAACTCG AGTTGGTGCTCTTCATCTTGTTGTTTTT
shEPCR#1 (TRCN0000061379)	CCGGGCAGCAGCTCAATGCCTACAACTCGA GTTGTAGGCATTGAGCTGCTGCTTTTTG
shEPCR#2 (TRCN0000061380)	CCGGGTGCAGTATGTGCAGAAACATCTCG AGATGTTTCTGCACATACTGCACTTTTTG
shEPCR#3 (TRCN0000374663)	CCGGAGCCAAACAGGTCGCTCTTACCTCGA GGTAAGAGCGACCTGTTTGGCTTTTTTG
shEPCR#4 (TRCN0000323594)	CCGGCGCAAGGAGAACGTGTTCTTTCTCGA GAAAGAACACGTTCTCCTTGCGTTTTTG

Figure 14. A. Map of the vector pLKO.1-puro, adapted from www.sigmaaldrich.com. B. shRNA sequences.

4.2. Isolation of plasmids

Bacteria were grown in Luria Broth (LB) medium (Conda) with 100 µg/ml ampicillin (Sigma-Aldrich) for 20 h at 37°C, on agitation (225 rpm). Plasmid extraction was carried out with ATP Plasmid Mini Kit (ATP Biotech Inc.) following manufacturer's instructions. Briefly, 2 ml of bacterial culture were transferred to a 1.5 ml tube and centrifuged at 15,000 g in a microcentrifuge. The supernatant was discarded and bacteria were lysed in the presence of RNase. The neutralized

lysate was transferred to a spin column containing plasmid DNA binding matrix. After a brief washing step, the purified plasmid was eluted by low-salt elution buffer and stored at -20°C.

4.3. Generation of lentiviral particles

Lentiviral particles were produced using X-tremeGENE HP DNA Transfection Reagent (Roche) and Lentiviral Packaging Mix (Sigma-Aldrich). HEK293T cells were seeded into 6-well plates at 600,000 cells/well in complete DMEM. After 24 h, medium was removed and Opti-MEM medium without antibiotics and with 10% FBS was added to the cells. For the production of lentiviral particles, the following mixture was prepared (amounts per well): 250 µl of antibiotics- and serum-free Opti-MEM, 2 µg of plasmid DNA, 5 µl of Lentiviral Packaging Mix and 9 µl of X-tremeGENE HP DNA Transfection Reagent. The mixture was incubated at room temperature for 15 min and added drop wise to the cells. Supernatants were collected after 48 h, centrifuged at 300 g for 5 min and filtered through cellulose acetate filters with 0.45 µm pores. Viral particles were stored at -80°C.

4.4. Infection of cells and selection of infected cells

1833 and ANV5 cells were seeded into 6-well plates one day before the infection. For the infection, 200 µl of viral particles were added per well, in the presence of 8 µg/ml polybrene. After 48 h, medium was removed and cells were incubated in medium supplemented with 4 µg/ml puromycin for 3 days. Antibiotic-resistant cells were expanded and frozen.

5. GENE EXPRESSION ANALYSIS

5.1. Total RNA extraction

5.1.1. RNA extraction from cell cultures

Total RNA was extracted from cells seeded at 80% confluence in 28 cm^2 plates using TRIzol® reagent (GIBCO), following manufacturer's instructions. Briefly, culture medium was removed and cells were scraped with 1 ml of TRIzol® and collected into 2 ml tubes. Samples were vigorously mixed and incubated for 3 min at room temperature after the addition of 200 µl of chloroform. After centrifugation at 12,000 g for 15 min at 4ºC, the upper aqueous phase was recovered into a 1.5 ml tube and the same volume of 100% isopropanol was added. After 10 min of incubation at room temperature, samples were centrifuged at 10,000 g for 10 min at 4ºC. The supernatant was discarded, and the pellet was washed with 1 ml of 75% ethanol. Samples were centrifuged at 7,500 g for 5 min at 4ºC and the supernatant was discarded. The pellet was air-dried during 5-10 min and resuspended in RNAse-free water. RNA concentration and purity were measured in a NanoDrop spectrophotometer, based on absorbance values at 260 and 280 nm. Samples were stored at -80ºC.

5.1.2. RNA extraction from tumors

Frozen tumors obtained at necropsy were crushed using a mortar and pestle, on dry-ice. Crushed frozen pieces were transferred to a 1.5 ml tube with 1 ml of TRIzol® reagent (GIBCO) and homogenized with a T10 Standard Ultra-Turrax (IKA). At this point, RNA extraction from subcutaneous tumors was performed as detailed in section 5.1.1. For microarray experiments (mammary tumors), samples were vigorously mixed and incubated for 3 min at room temperature after the addition of 200 µl of chloroform and centrifuged at 12,000 g for 15 min at 4ºC. Subsequently, RNA extraction was continued using RNeasy Mini Kit (Qiagen) following manufacturer's specifications. Briefly, lysis buffer containing guanidine-isothiocyanate and ethanol (to provide ideal binding conditions) were added to the samples, which were then loaded onto silica membrane columns. Traces of salts were removed from the columns by washing buffer and 80% ethanol. Finally, purified RNA was eluted in RNase-free water. RNA concentration and purity were measured in a NanoDrop spectrophotometer, based on absorbance values at 260 and 280 nm. Samples were stored at -80ºC.

5.2. Reverse transcription

RNA was reverse transcribed using DyNAmo cDNA Synthesis Kit (Thermo Scientific). This kit includes M-MuLV RNase H^+ reverse transcriptase (RT), 2X RT Buffer (containing dNTP mix and 10 mM $MgCl_2$) and random hexamers (300 ng/µl). The following mixture was set up for each reaction: 5 µl of buffer, 0.5 µl of random hexamers, 1 µl of transcriptase, 500 ng of RNA and RNase-free water up to 10 µl. Samples were subjected to the following incubation steps in a PTC-100 thermal cycler (MJ Research): 10' at 25ºC, 30' at 37ºC and 5' at 85ºC. cDNA was stored at -20ºC.

5.3. Semiquantitative PCR

cDNA was amplified with BIOTAQ DNA polymerase (Bioline). The following mixture was prepared per reaction: 2.5 µl of buffer (10X NH_4-based Reaction Buffer), 0.75 µl of 50 mM $MgCl_2$, 0.5 µl of 10 mM dNTPs, 1 µl of DMSO (Sigma-Aldrich), 0.5 µl of 10 µM forward primer, 0.5 µl of 10 µM reverse primer, 10 ng of cDNA, 0.2 µl of Taq DNA polymerase (5 U/µl) and water up to 25 µl. Primers used are specified in Table 4. Samples were subjected to the incubation steps described in Table 5 in a PTC-100 thermal cycler (MJ Research).

Table 4. Primers used for the detection of the human genes specified.

Gene	Forward primer (5' → 3')	Reverse primer (5' → 3')
EPCR	GTCTGGCTGGGCCTTTTGTA	GGAGATCTGGAGCATATGAAGTCTT
PAR1	GCTGATCATTTCCACGGTCT	CAGCAGCTGACAGGAACAAA
GAPDH	CTGCTCCTCCTGTTCGACAGT	CCATGGTGTCTGAGCGATGT

Amplified cDNA in 1X loading buffer (Promega) was loaded onto 2% agarose gels stained with SYBR® Safe DNA Gel Stain (Invitrogen). Agarose gels were prepared dissolving ultra-low agarose (Conda) in 1X TAE (40 mM Tris, 20 mM acetic acid, 1 mM EDTA). Electrophoresis was performed in 1X TAE buffer at 120 V for 30-60'. 1Kb Plus DNA ladder (Invitrogen) was used as weight marker. DNA was visualized under UV light in a Molecular Imager® Gel Doc™ XR System with Quantity One® software (Bio-Rad).

Table 5. Cycling parameters for PCR.

Segment	Cycles	Step	Temperature (ºC)	Time
1	1	Initial denaturation	94	2'
2	30	Denaturation	94	30''
		Primer annealing	55-60*	30''
		Extension	72	15''
3	1	Final extension	72	10'

* Depending on T_m of primers: T_m – 5ºC

5.4. Real-time quantitative PCR (qPCR)

qPCR was performed in an Applied Biosystems® 7500 Real-Time PCR instrument using FastStart Universal Probe Master (ROX) (Roche) or FastStart SYBR Green Master (Roche).

5.4.1. TaqMan assay

TaqMan® Gene Expression Assays contain a pair of unlabeled primers and a TaqMan® probe with a dye label (FAM™ in our case) on the 5' end and a nonfluorescent quencher (NFQ) on the 3' end. FastStart Universal Probe Master (ROX) contains buffer, dNTPs, DNA polymerase and a reference dye (ROX) for signal normalization. PCR reactions were performed with 0.5 µl of cDNA (20-25 ng), 0.5 µl of TaqMan® Gene Expression Assay, 5 µl of FastStar Universal Probe Master (ROX) and 4 µl of water. Mixes were subjected to the following incubation steps: 2' at 95ºC and 40 cycles of 15'' at 95ºC and 1' at 60ºC. TaqMan® Gene Expression Assays used are Hs00941182_m1 (human EPCR) and Hs03929097_g1 (human GAPDH).

5.4.2. SYBR Green assay

FastStart SYBR Green Master contains reaction buffer, dNTPs, Taq DNA polymerase and SYBR Green I dye (a DNA double-strand specific dye). PCR reactions were performed with 0.5 µl of cDNA (20-25 ng), 0.25 µl of 10 µM forward primer, 0.25 µl of 10 µM reverse primer, 5 µl of FastStart SYBR Green Master and 4 µl of water. Mixes were subjected to the following incubation steps: 2' at 95ºC, 40 cycles of 15'' at 95ºC and 1' at 60ºC and an additional final dissociation step, to calculate Tm of the amplified products in order to evaluate specificity of the reaction. Primers used are specified in Table 6.

Table 6. Primer sequences.

Gene	Forward primer (5' → 3')	Reverse primer (5' → 3')
FLNB	GTGACCCGAAGGGTGACTT	TGTGTGCCATCTCCATTGTC
FLNC	GCCTCCCTCTCGGATGAC	GGCTGGTTCACCTTGAGC
FZD8	CTCTGCTTCGTGTCCACCTT	GAAGCGCTCCATGTCGAT
HSPA1A	CGAGAAGGACGAGTTTGAGC	GCTGATGATGGGGTTACACA
HSPA1B	GGGTCAGGCCCTACCATT	AACAGTCCACCTCAAAGACAAAC
ITGB4	GCGATGACGTTCTACGCTCT	CCATTCACCAGGTGCTCA
ITPR3	CTAAGCCCAACCGGGAAC	CCTTCAGAATGCCAAAGACCT
KRT19	GCCACTACTACACGACCATCC	CAAACTTGGTTCGGAAGTCAT
SPOCK1	AGCACAAGGCAGAAAGGAGT	CGTGGAGAGCTCCAAACC

5.4.3. Data analysis

Data were analyzed using $2^{-\Delta\Delta Ct}$ method for relative gene expression quantification. Gene expression data were normalized with GAPDH (ΔCt = Ct target gene – Ct GADPDH). All ΔCt values were related to the ΔCt value of the reference sample (shControl): ΔCt sample – ΔCt reference sample.

5.5. Microarray hybridization and data analysis

Microarray analysis was performed on mammary tumors grown in athymic nude mice, to compare differentially expressed genes between control and EPCR-silenced cells *in vivo*. RNA extraction from tumors was carried out as indicated in section 5.1.2. RNA quality assessment and hybridization were performed in the Genomics Core Facility at CIMA. Data analysis was performed by Dr. Elizabeth Guruceaga (Genomics Core Facility, CIMA). First of all, RNA quality was analyzed using Experion™ (Bio-Rad) and only RNAs with RQI>7 were included in the experiment. RQI (RNA quality indicator) is a number (on a scale of 1-10) that indicates RNA degradation grade, an RQI of 1 being "highly degraded" and an RQI of 10 being "highly intact". RNAs extracted from 9 tumors (3 tumors per group: shControl, shEPCR#1 and shEPCR#2) were hybridized to Human Gene ST 2.0 microarrays (Affymetrix) and normalized with RMA (Robust Multi-Array Average) approach. Low expression probes were removed by filtering those that did not exceed a level of expression of 32 in at least one of the samples in each condition analysis. To obtain differentially expressed genes between control and EPCR-silenced cells, we independently compared shControl and shEPCR#1 tumors on one side and shControl and shEPCR#2 tumors on the other. Differentially expressed genes were identified using LIMMA (Linear Models for Microarray Data) method. Next, genes with B>0 in shEPCR#2 *vs* shControl analysis and genes with p<0.05 in shEPCR#1 *vs* shControl analysis were compared to obtain differentially expressed genes that were common to both analyses. These genes were analyzed using Ingenuity Pathway Analysis (IPA®, QIAGEN Redwood City, www.qiagen.com/ingenuity) to identify functions and pathways differentially activated between control and EPCR-silenced cells. We used a less stringent statistical criterion in shEPCR#1 *vs* shControl because of the relatively

low number of differentially expressed genes found in shEPCR#1 compared to shEPCR#2, in order to expand the number of common genes to work with.

6. WESTERN BLOT

6.1. Protein extraction

Proteins were extracted when cells reached 80% confluence in 28 cm^2 dishes. Cells were washed twice with cold DPBS, scraped in protein lysis buffer (1% Nonidet P-40, 150 mM NaCl, 50 mM Tris, 1 mM EDTA, 1 mM phenylmethylsulfonyl fluoride, 1 mM sodium orthovanadate, 5 mM NaF, pH 7.4) supplemented with a protease inhibitor cocktail (Roche) and transferred to 1.5 ml tubes. After 1 h of incubation on ice, lysates were centrifuged for 15 min at 15,000 g at 4ºC, to remove residual cellular debris. Supernatants were transferred to new 1.5 ml tubes and stored at -80ºC.

6.2. Protein quantification

Protein quantification was carried out using Pierce BCA Protein Assay Kit (Thermo Scientific). The quantification is based on a colorimetric method where proteins reduce Cu^{2+} to Cu^{+} in alkaline medium, which forms a water-soluble complex with bicinchoninic acid (BCA). This complex exhibits a strong absorbance at 562 nm, which is proportional to protein concentration in a broad concentration range (20-2000 µg/ml). A standard curve was prepared with BSA.

6.3. Electrophoresis and Transfer

Proteins (15-30 µg) were denatured at 99ºC for 10’ in 1X loading buffer (32 mM Tris-HCl pH 6.8, 12% glycerol, 2% SDS, 0.005% bromophenol blue and 1 mM DTT). Denatured samples were electrophoresed in discontinuous polyacrylamide gels, prepared as specified below. Electrophoresis was run under denaturing conditions (SDS-PAGE system) in electrophoresis buffer (25 mM Tris, 192 mM glycine and 0.1% SDS) for 30-60’ at 200 V. Proteins were subsequently transferred to nitrocellulose membranes in transfer buffer (25 mM Tris, 192 mM glycine, 0.05% SDS and 20% methanol) for 2 h at room temperature at 300 mA.

Discontinuous polyacrylamide gels were prepared following manufacturer´s recommendations. In this system, a stacking gel is added to the resolving gel, to compress samples into a thin starting band and finely resolve and separate individual proteins. To prepare 10 ml of monomer solution, the following reagents were mixed: 2.5 ml of gel buffer (1.5 M Tris-HCl, pH 8.8 for resolving gels and 0.5 M Tris-HCl, pH 6.8 for stacking gels), 0.1 ml of 10% SDS, 30% Acrylamide/Bis, 29:1 (Bio-Rad) and deionized water to 10 ml. Stacking gels were always prepared at 4% acrylamide, while resolving gels were prepared at 7-10% acrylamide, depending on protein size. Prior to pouring the gel, the catalysts TEMED and ammonium persulfate (APS) were added to the monomer solution (amounts per 10 ml): 7.5 µl of TEMED and 75 µl of APS for resolving gels and 10 µl of

TEMED and 100 µl of APS for stacking gels. Gels were allowed to polymerize for 30 min at room temperature and used immediately after or stored at 4ºC embedded in electrophoresis buffer for 2-3 days.

6.4. Immunodetection of proteins

Membranes were then blocked in 5% skimmed milk solution (buffered in 0.05% Tween-TBS) for 1 h at room temperature and incubated overnight at 4ºC with primary antibodies (Table 7). After overnight incubation, blots were washed three times for 5 min with 0.05% Tween-TBS and incubated with horseradish peroxidase (HRP)-linked secondary antibodies at 1:4000 dilution (Amersham) against rabbit, mouse or rat immunoglobulins for 1 h at room temperature. Membranes were washed three times for 5 min with 0.05% Tween-TBS and incubated for 1 min with the peroxidase substrate LumiLightPlus (Roche). Blots were exposed to ECL films (Amersham) for 10-60 s and developed in a Curix 60 processor (AGFA Healthcare).

Table 7. Primary and secondary antibodies used for western blot.

Protein	1º Antibody	Manufacturer	Dilution	2º Antibody
PARP	Anti-PARP	Cell Signaling	1:1000	Anti-rabbit IgG-HRP
β-actin	AC-15	Sigma-Aldrich	1:5000	Anti-mouse IgG-HRP
β-tubulin	H-235	Santa Cruz	1:5000	Anti-rabbit IgG-HRP
Human EPCR	1489	Dr. Esmon*	5 µg/ml	Anti-mouse IgG-HRP
Murine EPCR	RCR1	Dr. Fukudome**	5 µg/ml	Anti-rat IgG-HRP

* It was kindly gifted by Dr. Charles T. Esmon (Oklahoma Medical Research Foundation, Oklahoma City, USA. ** It was generously provided by Dr. Kenji Fukudome (Saga Medical School, Japan).

6.5. Stripping and re-probing

Primary and secondary antibodies were removed from the membrane after incubation with Restore Western Blot Stripping Buffer (Thermo Scientific) for 10-15 min at room temperature. Membranes were then washed twice in 0.05% Tween-TBS and re-probed with β-actin or β-tubulin antibodies for loading control, as specified above.

7. EPCR, PAR1, TM and S1P1 detection by flow cytometry

Cells were harvested and resuspended in PBN (DPBS containing 1% BSA and 0.02% sodium azide), at 10^6 cells/ml. One hundred thousand cells were incubated with primary antibodies at 10 µg/ml for 20 min on ice, washed with PBN and incubated with fluorochrome-coupled secondary antibodies at 20 µg/ml for 20 min in the dark. For EPCR expression analysis in the panel of breast cancer cell lines (Figure 19), a FITC-coupled secondary antibody was used. For EPCR, PAR1, TM and S1P1 expression analysis in MDA-MB-231 and 1833 cell lines (Figure 20) and EPCR expression analysis in ANV5 cell line (Figure 45), Alexa Fluor 647 fluorochrome-coupled secondary antibodies were used. After a washing step with PBN, cells were incubated with 7AAD

(BD Biosciences) for 10 min and analyzed in a FACSCalibur cytometer (BD Biosciences) using CellQuest software. 7AAD stained dead cells were excluded from the analysis. For each protein-specific monoclonal antibody used, another sample incubated with the corresponding isotype control was analyzed. Antibodies used are specified in Table 8.

Table 8. Antibodies used for flow cytometry.

Protein	1º Antibody	Isotype control	2º Antibody
Murine EPCR	RCR1	Rat IgG1,κ	Alexa Fluor 647 Goat Anti-rat
Human EPCR	RCR252	Rat IgG1,κ	Alexa Fluor 647 Goat Anti-rat FITC Mouse Anti-rat
Human PAR1	ATAP2	Mouse IgG1, κ	FITC Goat Anti-mouse
Human TM	QBEND-40	Mouse IgG2a, κ	FITC Goat Anti-mouse
Human S1P1	MM0044-7M15	Mouse IgG1, κ	FITC Goat Anti-mouse

All istoype controls and FITC-conjugated secondary antibodies are from BD Pharmigen™. Alexa Fluor 647 Goat Anti-rat antibody is from Invitrogen. RCR1 and RCR252 have been previously described. ATAP2 is from Santa Cruz and MM0044-7M15 is from Abcam.

8. *IN VITRO* PROLIFERATION ASSAY

Cell proliferation was assessed using MTS [3-(4,5-dimethylthiazol-2-yl)-5-(3-carboxy methoxyphenyl)-2-(4-sulfophenyl)-2H-tetrazolium] assay according to manufacturer's recommendations (Promega). This is a colorimetric assay, in which MTS compound is reduced by cells to a soluble colored formazan with absorbance at 490 nm. Cells (1,000 1833 or 500 ANV5) were seeded onto 96-well plates in complete medium and proliferation was assessed every day or every two days, as indicated in each experiment. RCR252, APC or conditioned media (CM) were refreshed every two days. Plates were incubated with MTS (10 µl/well) for 2 h at 37°C and read at 490 nm and 650 nm (reference) using a spectrophotometer. All absorbance values were normalized with the absorbance values from day 0 (5 h after seeding cells). Results are shown as mean values of six replicates ± SD.

9. CELL CYCLE ANALYSIS

Cell cycle analysis was carried out with Click-iT® EdU Flow Cytometry Assay Kit (Invitrogen). EdU (5-ethynyl-2'-deoxyuridine) is a nucleoside analog to thymidine and is incorporated into DNA during active DNA synthesis. It is detected by Alexa Fluor 647 dye, which is coupled to an azide that reacts with EdU in the presence of Cu. 7AAD (BD Biosciences) was used to stain DNA. After incubation, cells in the S-phase are Alexa Fluor 647 positive, cells in G0/G1 phase are stained with 7AAD and cells in G2/M phase show double 7AAD staining.

Cells were seeded in 28 cm^2 plates and maintained in culture for 24 or 48 h (specified in each experiment). At the time points indicated, cells were incubated with 10 µM EdU for 2 h. Next, cells were harvested (around 500,000 cells/well), washed in DPBS containing 1% BSA, and fixed in

formaldehyde (Click-iT® fixative) for 15 min at room temperature. Cells were washed in DPBS containing 1% BSA to remove formaldehyde, and permeabilized in 100 µl of 1X Click-iT® saponin-based permeabilization and wash reagent for 15 min at room temperature. Next, cells were incubated for 30 min at room temperature in the dark, with the Click-iT® reaction cocktail (250 µl/tube), prepared as follows (amounts per tube): 219 µl of DPBS, 5 µl of $CuSO_4$, 1.25 µl of Alexa Fluor 647-coupled azide and 25 µl of 1X Click-iT® EdU buffer additive. After a washing step with 1X Click-iT® saponin-based permeabilization and wash reagent, cells were resuspended in 250 µl of the same reagent and incubated with 0.2 µg/µl RNase A (Sigma-Aldrich) for 1 h at room temperature, in the dark. Ten µl of 7AAD were added to the tubes 10 min before the acquisition of cells in a FACSCanto II cytometer (BD Biosciences). Data were analyzed using FlowJo® software v9.3.

10. APOPTOSIS ASSAYS

We used staurosporine (Sigma-Aldrich) and TRAIL (Sigma-Aldrich) as apoptosis-inducing agents. Staurosporine is a broad-range kinase inhibitor and activates apoptosis by the intrinsic mitochondrial pathway. TRAIL is a ligand for two death domain-containing receptors (DR4 and DR5) and activates apoptosis by the extrinsic death receptor pathway.

Cells were seeded into 24-well plates (for flow cytometry) or 28 cm^2 dishes (for western blot) in complete medium. For the APC-stimulation experiment (Figure 22), 24 h after seeding, cells were washed twice with DPBS and cultured in serum-free medium overnight. Next day, cells were incubated with increasing doses of APC for 4 h, prior to the addition of 2 µM staurosporine for 1 h or 40 ng/ml TRAIL for 3 h. For the EPCR blockade experiment, 700 nM RCR252 was added to the cells 24 h after seeding. Next day, cells were incubated with staurosporine or TRAIL as indicated above. Apoptosis was determined by flow cytometry or western blot as indicated below.

10.1. Flow cytometry annexin-V binding assay

Apoptotic cells were detected by Alexa Fluor 647-conjugated annexin-V (Invitrogen). It binds to phosphatidylserine (PS) exposed on the outer leaflet of the plasma membrane during apoptosis, in the presence of Ca^{2+}. It can also pass through the compromised membranes of dead cells and bind to PS in the interior of the cell. Therefore, we also added 7AAD (a non-permeable dead cell dye) to distinguish necrotic cells from apoptotic cells.

Cells were harvested and resuspended at 10^6 cells/ml in annexin-binding buffer: 10 mM HEPES, 140 mM NaCl and 2.5 mM $CaCl_2$, pH 7.4. One hundred thousand cells were incubated with 3 µl of Alexa Fluor 647-conjugated annexin-V and 15 µl of 7AAD for 15 min at room temperature, in the dark. After adding 400 µl of binding buffer to each tube, cells were acquired in a FACSCanto II cytometer (BD Biosciences) and analyzed using FlowJo® software v9.3.

10.2. Western blot

Protein extraction, quantification and detection were performed as previously described in section 6. Apoptosis was quantified based on cleaved PARP expression. PARP is a nuclear poly(ADP-ribose) polymerase that is involved in DNA repair and is one of the main cleavage targets of caspase-3. Therefore, cleaved PARP is increased during apoptosis.

11. CO-CULTURE OF 1833 CELLS WITH ST2 AND WI38

11.1. Culture conditions

Preliminary experiments were performed to determine the best co-culture conditions. 1833 cells were co-cultured with ST2 cells at 1:5 ratio (1,000 cancer cells and 5,000 ST2 cells) for 72 h and with WI38 cells at 1:1 ratio (8,000 cancer cells and 8,000 ST2 cells) for 48 h, in 24-well plates.

11.2. Conditioned media (CM)

To obtain CM, ST2 and WI38 cells were seeded into 6-well plates. After 48 h, medium was collected and filtered through 0.2 µm pore filters (Sartorius Stedim Biotech), aliquoted and stored at -80ºC.

11.3. Luciferase activity measurements

Luciferase activity was measured using Luciferase Assay System (Promega), following manufacturer's instructions. Briefly, culture medium was removed and cells were washed with DPBS. Cells were lysed in 100 µl of 1X lysis buffer and transferred to 1.5 ml tubes. Samples were centrifuged at 15,000 g for 1 min and 50 µl of supernatant were transferred to test tubes. Thirty µl of luciferin were added immediately before measuring luciferase activity for 10 s in an LB Berthold luminometer. Luminescence values from cells in co-culture were related to luminescence values from cells cultured alone. Fold-increase of luciferase activity from triplicates ± SD is represented in the graphs.

12. MIGRATION AND INVASION ASSAYS

Migration and invasion assays were performed using the Boyden Chamber technique (Figure 15).

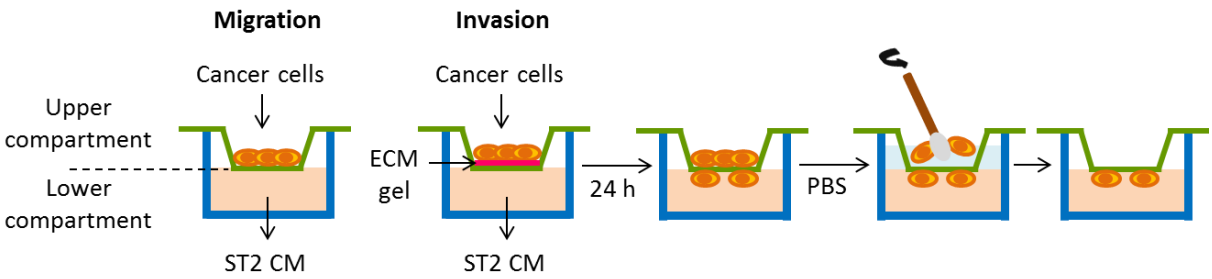

Figure 15. Boyden Chamber technique for migration and invasion assays.

Chambers with 8 µm pores were placed on 24-well plates containing 300 µl of CM from ST2 cells (obtained as detailed in section 11.2), creating an upper and a lower compartment. For invasion assays, chambers were precoated with 0.5 µg/µl ECM gel (Sigma-Aldrich) and dried at room temperature for 6 h, while no coating was added for migration assays. Cells maintained in serum-free medium for 24 h were added into the upper compartment (200,000 cells per well) and incubated at 37ºC. After 24 h, cells in the upper compartment were removed with DPBS and cotton swabs and cells in the lower compartment were fixed in 4% formaldehyde and stained with 0.4% crystal violet. Pictures (5 fields per well) were taken at 10X magnification with an inverted microscope (Leica). Stained areas were quantified using Fiji software[237].

13. *IN VIVO* EXPERIMENTS

All procedures (protocol number 161-14) were approved by the CEEA (Ethical Committee for Animal Experimental Research).

All cell lines injected were transduced with luciferase, as indicated in section 3.

13.1. Animals

Athymic nude mice (*Foxn1*^{nu}) were purchased from Harlan (Barcelona, Spain) and maintained under specific pathogen-free conditions. They are T-cell deficient and therefore, widely used for xenograft models. Five or six week-old female mice were used for all experiments.

MMTV-HER2 mice (FVB/N-TgN(MMTVneu)202Mul), available at The Jackson Laboratory, were a kind gift from Dr. Santisteban (Clínica Universidad de Navarra, Pamplona, Spain). These mice are homozygous for the MMTVneu (rat) transgene and develop spontaneous mammary tumors, which appear at 4 months, and frequently develop metastatic lesions to the lung (from 8th month on). Six week-old female mice were used for the orthotopic experiment.

RAG-2$^{-/-}$ mice were bred at the Animal Core Facility at CIMA. These are immunocompromised mice that lack mature T and B lymphocytes. Six week-old female mice were used for the intratibial experiment.

13.2. Subcutaneous injection

Cells were gently washed twice with DPBS, detached with trypsin and resuspended at 2 x 10^6 cells/ml in sterile PBS. Growth factor reduced matrigel (BD Biosciences) was added at 1:1 ratio to the cell suspension. Fifty µl containing 500,000 cells in DPBS:Matrigel were injected into the right and left dorsal flanks of 6 week-old athymic nude mice (2 tumors per mouse).

13.3. Orthotopic injection

Cells were gently washed twice with DPBS, detached with trypsin and resuspended at 2 x 10^6 cells/ml (1833) or 4 x 10^5 cells (ANV5) in sterile DPBS. Growth factor reduced matrigel (BD

Biosciences) was added at 1:1 ratio to the cell suspension. Fifty µl containing 500,000 cells (1833) or 10,000 cells (ANV5) in DPBS:Matrigel were directly injected into the fourth mammary fat pads of 6 week-old mice (2 tumors per mouse). Mice were anesthetized with isofluorane (Braun) before performing the injections. In the second orthotopic experiment, 1833 cells were injected resuspended in DPBS without matrigel. Bioluminescence imaging (BLI) was performed immediately after injection to confirm the quality of the procedure, as indicated below.

13.4. Primary tumor growth assessment

In subcutaneous and orthotopic experiments, tumor growth was monitored regularly using a digital caliper. Tumor volume was calculated as follows: π x length x width^2 / 6. In the orthotopic experiment with ANV5 cells, tumor growth was monitored by BLI during the first days of the experiment, as indicated below.

13.5. Tumor resection and metastasis follow-up

Orthotopic tumors were resected when their size reached 300 mm^3 (1833 tumors) or 500 mm^3 (ANV5 tumors). Tumors were excised from a small incision made near each mammary gland and cut into two pieces. One piece was snap-frozen in liquid nitrogen and stored at -80ºC. The other half was formalin-fixed and used for histological analysis. Incidence of metastasis was followed-up by BLI once a week until the end of the experimental period, as detailed below. Subcutaneous tumors were resected at sacrifice, snap-frozen and stored at -80ºC.

13.6. Flow cytometry analysis of immune cells infiltrating mammary tumors

This experiment was carried out at Dr. Mikala Egeblad's laboratory, at Cold Spring Harbor Laboratory (NY, USA), with the assistance of Dr. Ana Almeida. The analysis was performed in mammary tumors developed in athymic nude mice, after the injection of 1833 cells into the fourth mammary fat pads of mice (without matrigel), as indicated above. Mice were sacrificed at day 32 post-injection: one tumor was formalin-fixed for histological analysis and the other tumor was used for flow cytometry analysis. Dissection of lymph nodes was carefully avoided during resection of mammary tumors.

13.6.1. Isolation of cells

Tumors were resected and mechanically dissociated with a razor blade in 3 ml of RPMI, on ice. Minced tumors were transferred to 10 ml of collagenase buffer (0.2% (w/v) collagenase (Sigma-Aldrich) and 4 U/ml DNAse I (Roche) in RPMI) and incubated at 37ºC for 1 h, on a gentle shaker. Digested tumors were centrifuged at 300 g for 8 min at 4ºC. Supernatants were transferred to new tubes and centrifuged again at 300 g for 8 min at 4ºC. Pellets obtained in both centrifugations were resuspended in ice-cold R10 (RPMI + 10% heat-inactivated FBS) and ice-cold DPBS (1:1 ratio) and filtered through 100 µm cell strainers. Samples were centrifuged at 300 g for 8 min at 4ºC and pellets were resuspended and incubated for 2 min at room temperature in

5 ml of Red Blood Lysis Buffer (Sigma-Aldrich). Twenty ml of ice-cold DPBS and R10 (1:1 ratio) were added to the samples prior to centrifugation at 300 g for 6 min at 4ºC. Supernatants were discarded and pellets were resuspended in ice-cold R10 (5-10 ml) and filtered through 100 µm cell strainers before cell counting. One or two spleens (depending on the size) were subjected to the same procedure and used as controls, except that digestion with collagenase was omitted and the red blood cell lysis step was performed twice.

13.6.2. Staining

Cells were plated in 96-well round-bottom plates at 10^6 cells/well. Plates were centrifuged at 300 g for 4 min at 4ºC. Supernatant was discarded and cells were resuspended and incubated at 4ºC for 15 min in 50 µl of FACS buffer (1X DPBS, 1% FBS, 0.02% (w/v) sodium azide) with Fc Block™ (BD Biosciences) at 1:50 dilution. Cells were immunostained with antibody solutions (Table 9) for 30 min at 4ºC, in the dark. Cells were washed twice with 150 µl of ice-cold FACS buffer, resuspended in FACS buffer and transferred to test tubes (at a final volume of 500 µl). Ten min before acquisition of the cells, 5 µl of 7AAD (BD Biosciences) were added to the tubes to stain dead cells.

Table 9. Antibodies and isotype controls.

Antibody	Dilution	Manufacturer	Reference
CD45-APC	1:300	BD Pharmigen	559864
CD11b-PE	1:300	BD Pharmigen	557397
CD19-APC-eFluor 780	1:300	eBioscience	47019380
Nkp46-eFluor 450	1:100	eBioscience	48335180
Ly6G-APC-eFluor 780	1:300	eBioscience	47593180
Ly6C- PE-Cy7	1:300	BioLegend	128017
MHCII-eFluor 450	1:200	eBioscience	48532180
Rat IgG2b-APC	1:300	BD Pharmigen	553991
Rat IgG2c-PE-Cy7	1:300	BioLegend	400721
Rat IgG1a-eFluor 450	1:200	eBioscience	48432180
Rat IgG1a-PE	1:300	eBioscience	12432180

Note: we did not have an isotype control for APC-eFluor 780.

Simultaneously, spleen cells were stained with antibodies (positive control) and with the corresponding isotype controls (negative control) following the same procedure already detailed.

OneComp eBeads (BD Biosciences) were used to perform fluorescence compensation. OneComp eBeads contain two populations: a positive population that reacts with antibodies and a negative population that does not. Therefore, after incubation of the beads with fluorochrome-conjugated antibodies, both positive and negative populations were observed. Beads staining was performed according to manufacturer's specifications. Briefly, 50 µl of beads were incubated with each antibody for 30 min at 4ºC, in the dark. Beads were washed with 2 ml of FACS buffer

and centrifuged at 500 g for 4 min. Supernatant was discarded and beads were resuspended in 400 µl of FACS buffer for the acquisition in the cytometer.

13.6.3.Flow cytometry

Cells and beads were acquired in an LSR- II Flow Cytometer (BD Biosciences) in the Flow Cytometry Shared Resource at Cold Spring Harbor Laboratory (NY, USA). FSC/SSC settings and fluorescence detector (PMT) voltages were established with unstained samples and compensations were performed with OneComp eBeads. Around 500,000 cells were acquired per sample. Data were analyzed with FlowJo® software v9.3. 7AAD stained dead cells were excluded from the analysis and cell populations were gated on live cells following the gating strategy shown in Figure 34A.

13.7. Intracardiac injection

Cells at 50% confluence were gently washed with DPBS, detached and resuspended at 10^6 cells/ml in sterile DPBS. Mice were anesthetized with ketamine (100 mg/kg of body weight) and xylazine (10 mg/kg of body weight) before inoculation of 100 µl containing 10^5 cells into the left cardiac ventricle, using a 29G needle syringe. Cell viability was always >95%, otherwise experiment was stopped. Whole-body bioluminescence (BL) was measured immediately after the injection, as indicated below.

13.8. Intratibial injection

Cells at 50% confluence were gently washed with DPBS, detached and resuspended at 3 x 10^6 cells/ml in sterile DPBS. Mice were anesthetized with ketamine (100 mg/kg of body weight) and xylazine (10 mg/kg of body weight) before inoculation of 5 µl containing 15,000 cells into the tibia's bone marrow through the femoro-tibial cartilage using a Hamilton syringe. BL was measured immediately after the injection, as indicated below.

13.9. Intravenous injection

Cells at 50% confluence were gently washed with DPBS, detached and resuspended at 10^6 cells/ml in sterile DPBS. An amount of 100,000 cells in 100 µl of DPBS was injected through the tail vein of 6 week-old athymic nude mice. Lung photon flux was measured immediately after the injection, as indicated below.

13.10. Therapeutic regimens

$F(ab')_2$ RCR252 antibodies were generated as described previously. IgG control antibodies were obtained from Sigma-Aldrich (I4131). Both RCR252 and IgG were resuspended in vehicle (10 mM HEPES, 150 mM NaCl) at 250 µg/ml. Mice were treated with 50 µg of the antibodies daily, administered intraperitoneally in 200 µl of vehicle. Treatment was started the day before the inoculation of cancer cells.

13.11. Bioluminescence imaging (BLI)

BL images were taken after animals were anesthetized and inoculated into the retro-orbital plexus with 50 µl of 15 mg/ml D-luciferin (Promega). Images were taken immediately after the injection of luciferin (Promega) during 1 min with a PhotonIMAGER^{TM} imaging system (Biospace Lab) and analyzed using M3Vision software (Biospace Lab). Photon flux was calculated for each mouse by using a region of interest (ROI) for each hindlimb, lung and mammary gland, or by delineating the mouse for whole-body BL quantification. All BL signals were normalized with values from day 0, except for the metastasis experiment with RCR252 treatment.

13.12. Radiographic analysis

X-ray radiography was performed under anesthesia, with mice placed on the prone position on sensitive radiographic films (Carestream Health). Mice were exposed to X-irradiation at 20 kV for 20 s using a MX-20 Faxitron instrument (Faxitron). Isolated bones were X-irradiated at 18 kV for 10 s. High-resolution X-ray film scans were captured at 1600 ppi using an Epson Expression 1680 Pro scanner (Long Beach, CA, USA) and osteolytic bone area was calculated using Fiji software[237], by manually delineating osteolytic and total bone areas.

13.13. Micro-computed Tomography (Micro-CT)

Micro-CT analysis was performed on formalin-fixed bones at the Imaging Core Facility at CIMA. Whole femoro-tibial joints were analyzed by a micro CAT II scanner (Siemens Preclinical Solutions, TN, USA) at 75.0 kVp and 250.0 uA. The scans were performed at 10 µm resolution. 2D CT images were reconstructed using a standard convolution-back projection procedure with a Shepp-Logan filter (software Amira 4.1). Images were stored in 3D arrays with a voxel size of 21 µm x 21 µm x 21 µm.

14. HISTOLOGICAL ANALYSIS

Mammary tumors, lungs and hindlimbs were formalin-fixed for 24 h and maintained in 70% ethanol after. Mammary tumors were resected as previously explained. Lungs were perfused with formalin before extraction. Tibiae and femurs were excised and cleaned of all soft tissues before decalcification in Osteosoft solution (Merck) for 72 h, on an orbital shaker. All subsequent procedures were conducted at the Morphology Core Facility at CIMA. Tissues were embedded in paraffin and cut into 5 µm sections. Hematoxylin-eosin staining (H&E) and several immunohistochemical stainings were carried out.

14.1. Immunohistochemistry

Ki67, caspase-3, CD31, F4/80, vimentin and EPCR immunostainings were performed at the Morphology Core Facility at CIMA, by Dr. Laura Guembe. pERK immunostainings were

performed at the New Therapeutic Targets Laboratory at CIMA. Briefly, slides were dewaxed with xylene and rehydrated through a graded series of ethanol. Antigen retrieval was carried out as indicated in Table 10 and endogenous peroxidase activity was quenched by incubating slides with 3% hydrogen peroxide for 12 min. Sections were incubated with primary antibodies overnight at 4ºC in a humidified chamber. After washing with TBS-Tween, secondary antibodies were applied. Peroxidase activity was revealed with diaminobenzidine (DAB) and sections were lightly counterstained with Harris hematoxylin. Finally, slides were dehydrated in a graded series of ethanol, cleared in xylene and mounted in Cytoseal XYL (Thermo Scientific).

Table 10. Antibodies used in immunohistochemistry.

Antigen	Antibody	AR	Dilution	Raised in	Detection
Ki67	Neomarkers (RM9106)	TE, pH 9, 95ºC, 30 min	1:100	Rabbit	EnVision anti-rabbit[1]
CD31	Dianova (DIA 310)	TE, pH 9, 95ºC, 30 min	1:50	Rat	Rabbit anti-rat[2] EnVision anti-rabbit[1]
Caspase-3	Cell Signaling (9661)	TE, pH 9, 95ºC, 30 min	1:100	Rabbit	EnVision anti-rabbit[1]
Vimentin	Dako (M0725)	TE, pH 9, 95ºC, 30 min	1:400	Mouse	EnVision anti-mouse[3]
F4/80	eBiosciences (14-4801-82)	PK 20 µg/ml, 37ºC, 30 min	1:400	Rat	Rabbit anti-rat[2] EnVision anti-rabbit[1]
EPCR	HEPCR1489*	TE, pH 9, 95ºC, 30 min	1:200	Mouse	EnVision anti-mouse[3]
pERK	Cell Signaling (9101)	TE, pH 9, 95ºC, 30 min	1:50	Rabbit	EnVision anti-rabbit[1]

*This monoclonal antibody (1.5 mg/ml) was produced and kindly provided by Dr. Charles Esmon. AR: Antigen retrieval. TE: 10 mM Tris, 1 mM EDTA. PK: Proteinase K. [1]Dako K4011, [2]Dako E0468 (1:200), [3]Dako K4007.

14.2. Quantification

All slides were captured using a Zeiss Axioimager M1 (Zeiss) microscope and ZEN (Zeiss) software. H&E stained slides were captured at 2.5X magnification. Tumor area was calculated using Fiji software[237], by manually delineating tumor and total bone or lung areas. For immunohistochemical analyses, random pictures (5-25, depending on tumor size) were taken at 20X magnification and stained areas or cells were quantified using Fiji software[237].

15. *IN SILICO* EXPERIMENTS

15.1. Relapse-free survival analyses

Gene expression and clinical data were obtained from the GSE2034 public database[238]. This cohort includes 286 frozen tumor samples from patients with lymph-node negative breast cancer

treated during 1980-95 at Erasmus Medical Center (Rotterdam, Netherlands). Patients did not receive systemic neoadjuvant or adjuvant therapy. From this cohort, 219 patients had undergone breast-conserving surgery and 67 modified radical mastectomy. A total of 248 patients (87%) received radiotherapy. The proportions of patients who underwent breast-conserving surgery and radiotherapy were normal for lymph-node negative disease. Of the 286 patients, 106 patients relapsed and had distant metastasis (target organ was not specified), of whom 93 showed evidence of distant metastasis within 5 years. The number of tumors in each molecular subgroup is representative of the prevalence of these breast cancer subtypes among patients in general. All samples were evaluated to have >70% tumor and uniform tumor distribution. Patient and tumor characteristics are summarized in Figure 16. Gene expression values were obtained from the Affymetrix oligonucleotide microarray U133a GeneChip. For the construction of Kaplan-Meier curves, gene expression data above median expression value were classified as “High”, whereas gene expression data below median expression value were classified as “Low”. Log-rank test was used in Kaplan-Meier curves to compare differences in relapse-free survival between patients.

A

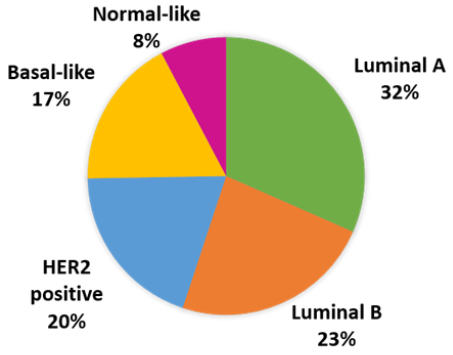

B

Patient and tumor characteristics	Nº patients	Patient and tumor characteristics	Nº patients
Age (years)		**Grade**	
≤ 40	36 (13%)	Poor	148 (52%)
41-55	129 (45%)	Moderate	42 (15%)
56-70	89 (31%)	Good	7 (2%)
> 70	32 (11%)	Unknown	89 (31%)
Menopausal status		**ER status**	
Premenopausal	139 (49%)	Positive	209 (73%)
Postmenopausal	147 (51%)	Negative	77 (27%)
T stage		**PR status**	
T1	146 (51%)	Positive	165 (58%)
T2	132 (46%)	Negative	111 (39%)
T3/4	8 (3%)	Unknown	10 (3%)

Figure 16. GSE2034 cohort. A. Percentages of tumors in each molecular subgroup in the GSE2034 database. B. Patient and tumor characteristics. Total number of patients: 286. Numbers in parenthesis are percentage of patients.

15.2. Validation of the genes obtained in the microarray experiment

Patients were classified into “Low EPCR” or “High EPCR” according to the median expression value of EPCR. Mean gene expression values for the genes indicated (Figure 44) were compared between these two groups.

16. STATISTICAL ANALYSIS

Statistical analysis was performed using SPSS v15.0 for Windows. Prior to each analysis, normality and homoscedasticity were assessed by Shapiro-Wilk and Levene tests, respectively. When data exhibited homoscedasticity, pairwise Student’s t test and Mann-Whitney U test were

used for normally and non-normally distributed variables, respectively. When data did not exhibit homoscedasticity, Welch and Median tests were used for normally and non-normally distributed variables, respectively. ANOVA and posterior Bonferroni tests were used for multiple comparisons of normally distributed variables. Kruskal-Wallis and posterior Bonferroni adjusted-Mann-Whitney U tests were used for multiple comparisons of non-normally distributed variables. Survival curves were compared with long-rank test. Statistical significance was defined as significant ($p < 0.05$, *), very significant ($p < 0.01$, **) and highly significant ($p < 0.001$, ***).

IV Results

1. EPCR EXPRESSION IN THE PRIMARY TUMOR CORRELATES WITH RECURRENCE IN BREAST CANCER PATIENTS

Previous findings indicated that EPCR is a poor prognosis factor in lung cancer patients. To evaluate the potential clinical relevance of EPCR in breast cancer, we obtained clinical and EPCR expression data from a cohort of 286 breast cancer patients (GSE2034 public database[238]) and performed a relapse-free survival analysis. Of the 286 patients, 106 patients relapsed and developed a distant metastasis (target organ was not specified). Patient and tumor characteristics are described in detail in the Material and Methods section. For the construction of Kaplan-Meier curves, EPCR expression data above median expression value were classified as “High”, whereas EPCR expression data below median expression value were classified as “Low”. We found that patients with high EPCR expression levels had very significantly shorter relapse-free survival times; p=0.002 (Figure 17A).

Molecular subtypes of breast cancer correlate with different clinical outcomes. We speculated that differences in survival could be due to higher EPCR expression levels in tumors from poor prognosis molecular subtypes. To explore this possibility, we compared EPCR expression levels among different molecular subsets. The variability of EPCR expression between patients of the same subtype was high. Moreover, HER2+ and basal subsets, which are the ones with the poorest prognosis, had the lowest median expression value of EPCR (Figure 17B). Thus, these results confirm that EPCR is an independent poor prognosis factor in breast cancer patients.

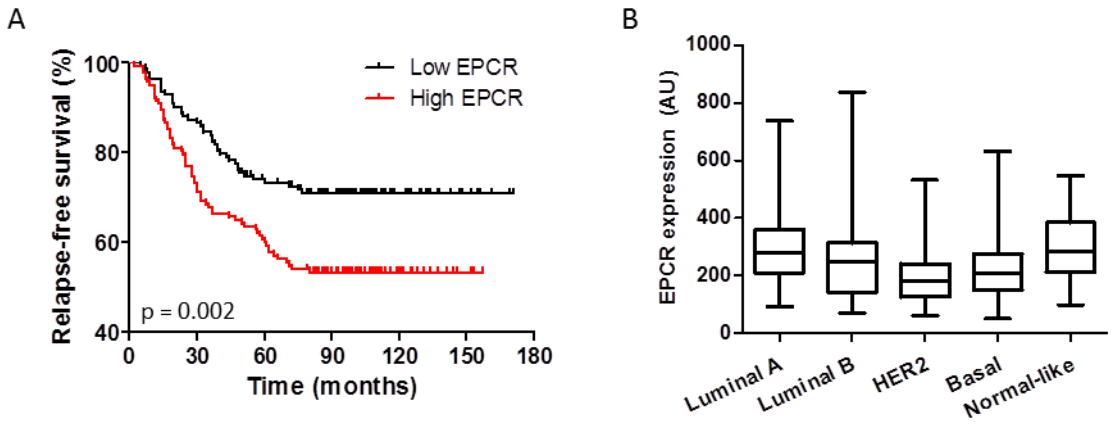

Figure 17. Kaplan-Meier analysis in breast cancer patients based on EPCR expression levels. A. Relapse-free survival curve of all patients included in the GSE2034 cohort (n=286), classified into “High EPCR” and “Low EPCR” based on median expression value of EPCR. Log-rank test was used to determine p value (p=0.002). B. EPCR expression levels in the primary tumors, classified by molecular subtype. Whiskers represent minimum and maximum values. AU, arbitrary units.

Finally, in order to investigate whether EPCR could predict clinical outcome in all the molecular subtypes, we performed the relapse-free survival analysis in each subset. Despite loss of

statistical potency due to the limited number of patients included in each group, survival analysis revealed that EPCR expression correlated with recurrence in HER2+ (p=0.030), basal (p=0.051) and luminal B (p=0.007) subtypes, but not in luminal A subgroup (Figure 18).

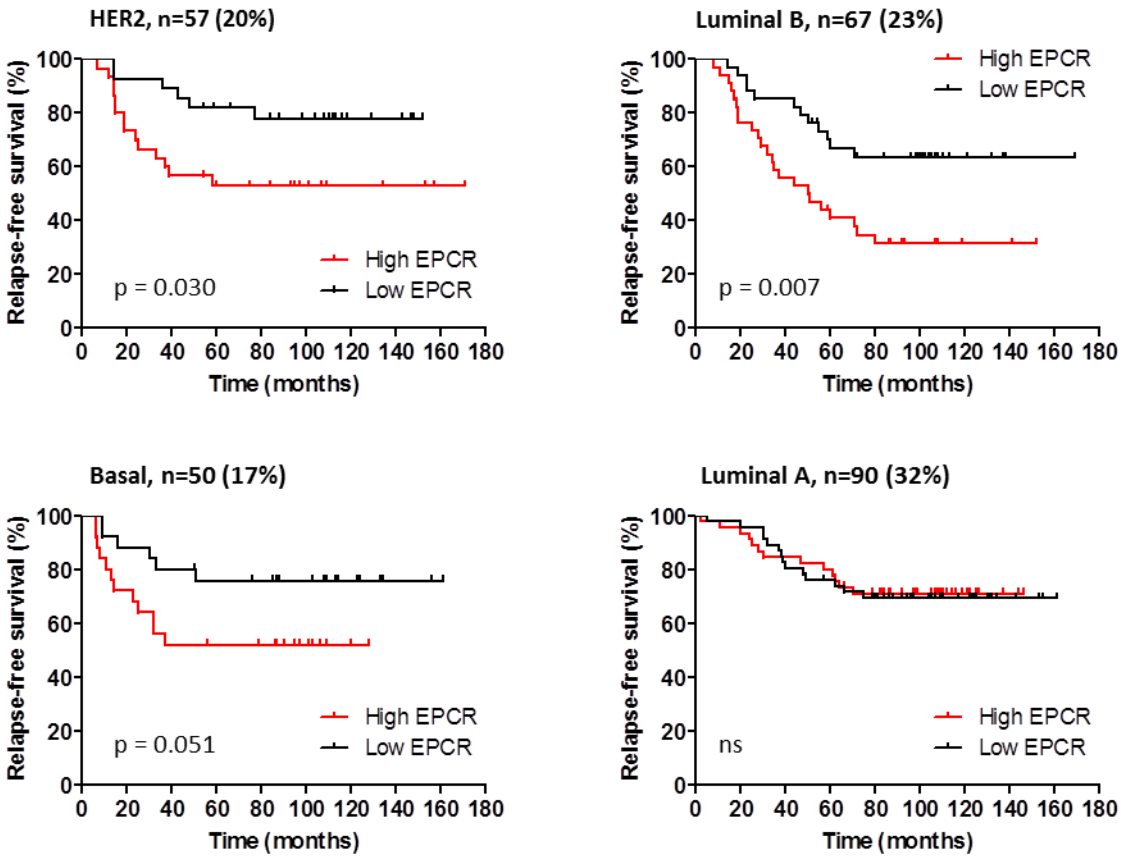

Figure 18. Kaplan-Meier analysis in breast cancer patients based on EPCR expression levels. Relapse-free survival curves for each molecular subtype of breast cancer. Log-rank test was used to determine p values.

Since luminal A is the subtype correlated with better prognosis, these results reveal the clinical relevance of EPCR in breast cancer patients with poor clinical outcome and support a deeper characterization of the role of EPCR in breast cancer.

2. EPCR PROMOTES TUMORIGENESIS AND METASTASIS IN A HUMAN BREAST CANCER MODEL

2.1. MDA-MB-231 #1833 cells express EPCR, PAR1 and TM

To select a model for the characterization of EPCR activity in breast cancer, we first analyzed EPCR expression by flow cytometry in a panel of human breast cancer cell lines: luminal A (T47D, MCF7, CAMA-1), luminal B (BT474, ZR7530), TN claudin-low (BT549, MDA-MB-231) and HER2+ (SKBR3) (Figure 19).

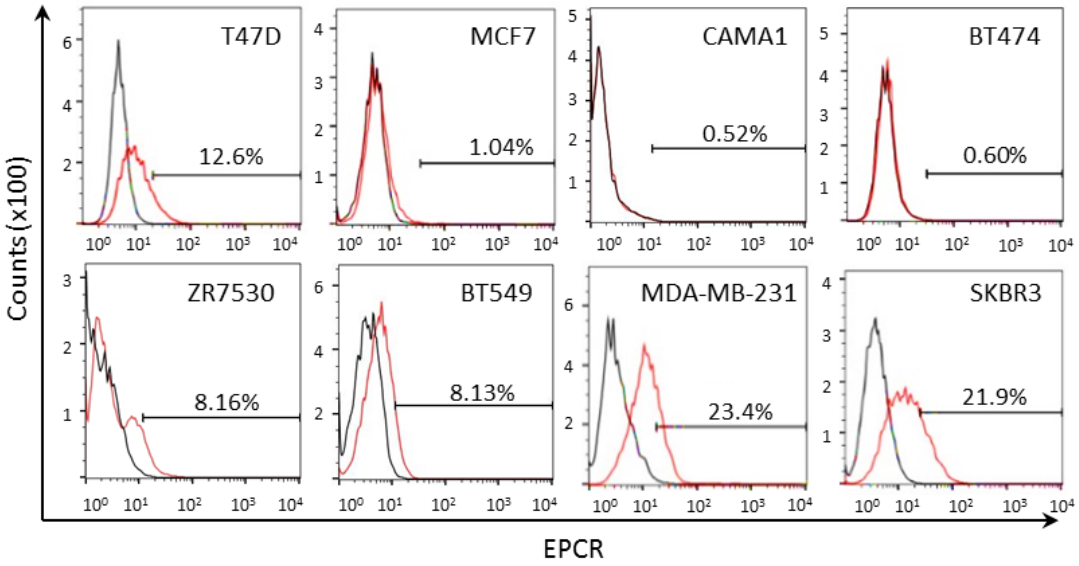

Figure 19. Analysis of EPCR expression levels in a panel of human breast cancer cell lines. EPCR expression levels were determined by flow cytometry. Black lines represent the isotype control while red lines represent EPCR expression. Percentage of cells expressing EPCR is indicated.

We selected MDA-MB-231 cell line since it showed the highest EPCR expression levels and is classified as TN claudin-low, the subtype with the worst clinical outcome in breast cancer patients. Since we were also interested in evaluating the prometastatic activity of EPCR, we used the #1833 bone-seeking metastatic subline (see Material and Methods section).

Parental and metastatic MDA-MB-231 #1833 (from now on 1833) cells showed similar expression levels of EPCR and its co-receptor PAR1, assessed by flow cytometry (Figure 20A), western blot (Figure 20B) and PCR (Figure 20C). Both cell lines expressed thrombomodulin (TM), required for the activation of protein C (PC) on the surface of endothelial cells. This finding indicates that PC could also be activated on the surface of tumor cells. Interestingly, both cell lines were negative for S1P1, which dismisses the possibility of cross-signaling between EPCR and S1P1 pathways in this model.

Of note, according to the flow cytometry data, all cells express EPCR in both parental and metastatic cell lines. MCF7 cells were used as negative control (data not shown). This discrepancy from the previous flow cytometry assay, in which only 23% of cells expressed EPCR in the parental MDA-MB-231 cell line (Figure 19), could be related to the different fluorescent dyes used between experiments. In contrast to FITC, Alexa Fluor 647 is pH-insensitive and has high brightness and photostability.

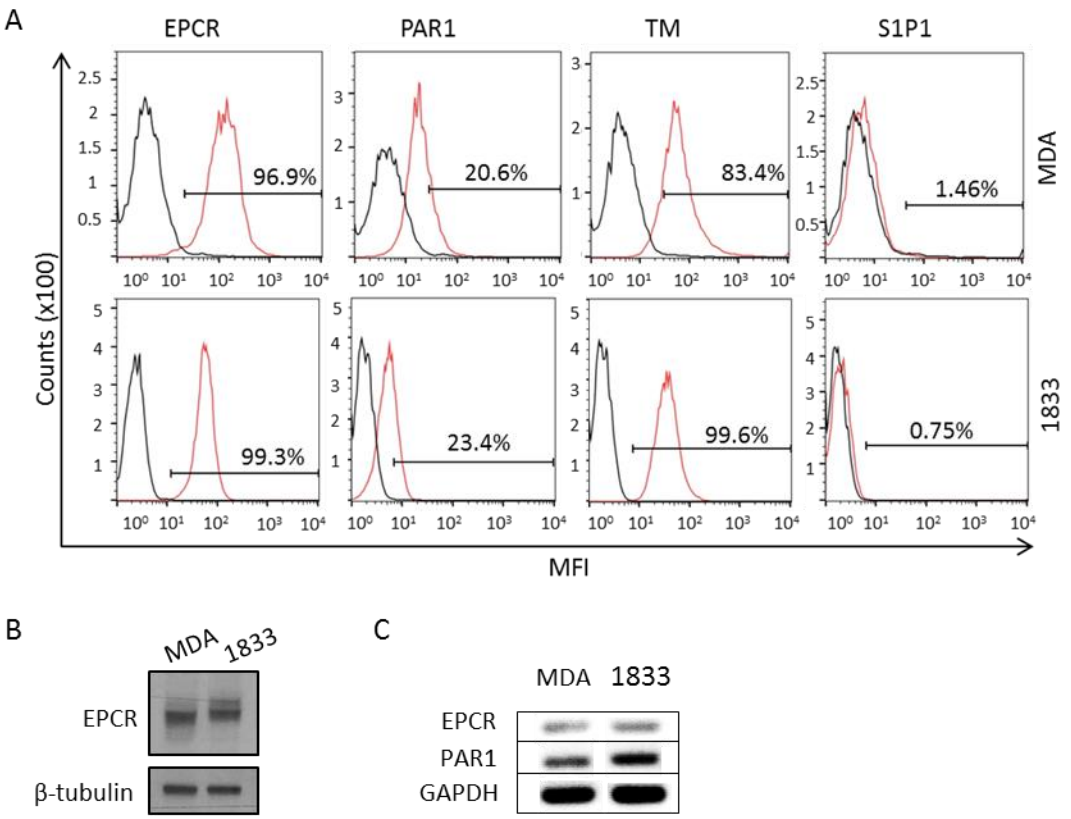

Figure 20. EPCR and its co-receptors PAR1, TM and S1P1 expression levels in MDA-MB-231 (MDA) and its metastatic subclone 1833. A. Flow cytometry assay of membrane-associated EPCR levels. Black lines represent isotype controls and red lines expression levels. Percentages of cells expressing each receptor are indicated. Top: MDA-MB-231. Bottom: 1833. B. Total EPCR protein levels in MDA-MB-231 and 1833 cell lines detected by western blot. β-tubulin was used as loading control. C. EPCR and PAR1 mRNA levels, detected by PCR. GAPDH was used as loading control.

2.2. EPCR does not affect proliferation and apoptosis of 1833 cells *in vitro*

2.2.1. Stimulation of cells with APC

The main known ligand of EPCR is APC, which triggers cytoprotective and anti-apoptotic functions in endothelial cells through EPCR-mediated PAR1 activation[189]. We have previously shown that anti-apoptotic signaling through APC-EPCR interaction also promotes bone metastasis in lung cancer[217]. Therefore, we analyzed whether APC could signal and mediate cellular functions to favor tumor progression in 1833 cells, which express EPCR and its co-receptors.

To evaluate the effect of APC on cell proliferation, we treated 1833 cells with increasing doses of APC, ranging from 5 to 100 nM, for 8 days and their proliferation rate was measured by MTS assay. APC did not have any effect on cell growth kinetics compared to non-treated cells (Figure 21A). During the experiment cells were maintained in medium with 4% FBS, the lowest FBS

concentration that allowed cell proliferation in a preliminary experiment (data not shown). Low FBS concentration was required to avoid APC inactivation by serum components.

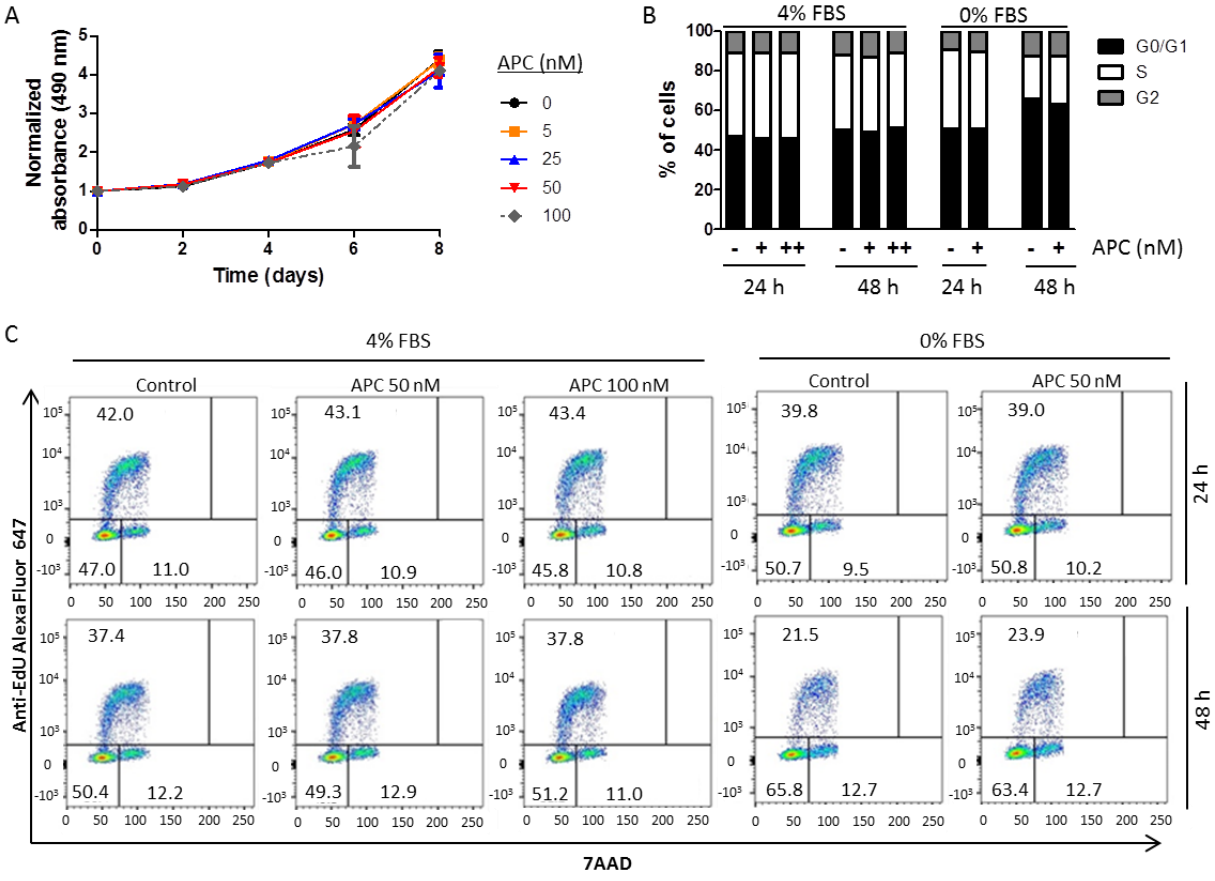

Figure 21. Effects of APC stimulation on proliferation of 1833 cells. A. *In vitro* proliferation of 1833 cells under stimulation with increasing doses of APC, assessed by MTS assay. Data were normalized with the absorbance from day 0. Each dot represents mean ± SD of six replicates from the same experiment. B. Quantification of cells in each phase of the cell cycle, after maintaining cells in culture for 24 and 48 h; +: 50 nM APC, ++: 100 nM APC. C. Flow cytometry graphs showing cells in G0/G1 (lower left), S (upper) and G2/M (lower right) phases of the cell cycle. Numbers indicate the percentage of cells in each phase. Cells in S phase were stained with anti-EdU Alexa Fluor 647 and DNA was stained with 7AAD. Top graphs: 24 h in culture. Bottom graphs: 48 h in culture.

We also performed cell cycle analysis in control and APC-stimulated conditions, using EdU incorporation flow cytometry assay. Cells were maintained in culture for 24 and 48 h in medium with 4% FBS, without APC or with 50 nM and 100 nM APC, and incubated with EdU for 2 h prior to flow cytometry analysis. The percentage of cells in each phase of the cell cycle was similar in all conditions tested (Figures 21B and 21C). We speculated that the amount of FBS present in the medium could still inactivate APC. To overcome this limitation we performed an additional experiment in serum-free medium. Stimulation of cells with 50 nM APC for 24 and 48 h did not alter cell cycle progression compared to non-treated cells (Figures 21B and 21C).

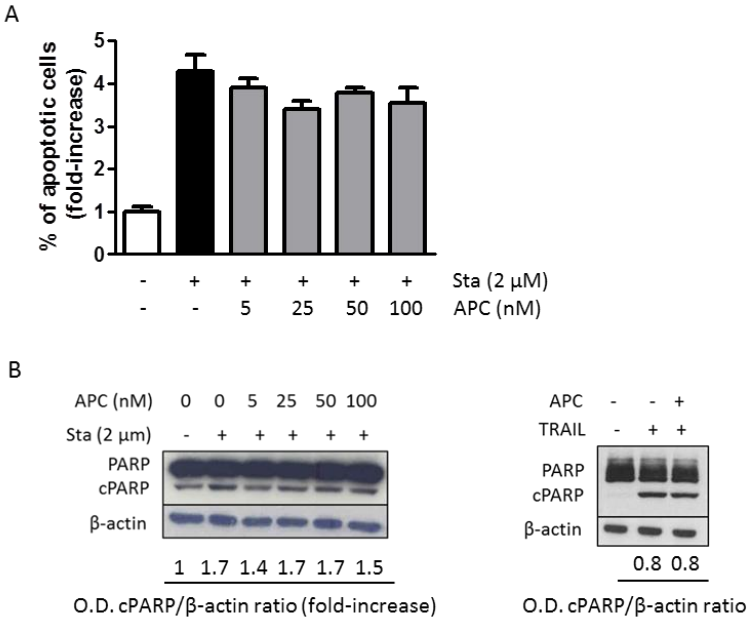

Figure 22. Effects of APC stimulation on apoptosis of 1833 cells. A. Quantification of apoptotic cells by annexin-V binding flow cytometry assay. Data are mean ± SD of triplicates from the same experiment. Data are representative of three independent experiments. E. Detection of staurosporine (left) and TRAIL (right) induced apoptosis in control and APC-stimulated cells by western blot. The amount of apoptosis is proportional to the amount of cleaved PARP (cPARP). β-actin was used as loading control. Numbers indicate quantification of western blot signals by densitometry. O.D., optical density. Sta, staurosporine.

Next, we tested whether APC could prevent staurosporine- or TRAIL-induced apoptosis in 1833 cells. Cells were treated with increasing doses of APC ranging from 5 to 100 nM in serum-free medium for 4 h before adding staurosporine. APC stimulation did not reduce the extent of apoptosis induced by staurosporine alone, assessed by annexin-V binding flow cytometry assay (Figure 22A) and western blot analysis (Figure 22B). Stimulation of cells with 50 nM APC was also not able to prevent TRAIL-induced apoptosis (Figure 22B).

2.2.2. EPCR knockdown

2.2.2.1. EPCR blockade with RCR252

We speculated that the lack of cellular responses in 1833 cells after exogenous administration of APC could be due to endogenous production of APC by 1833 cells. To test this hypothesis, we analyzed the effects of the anti-EPCR antibody RCR252, which blocks APC-EPCR interaction, on the proliferation and apoptosis of 1833 cells.

Increasing doses of RCR252, ranging from 100 to 750 nM, did not reduce proliferation rate of 1833 cells compared to non-treated cells, assessed by MTS proliferation assay for 7 days (Figure 23A).

For cell cycle analysis, cells were maintained in culture for 24 and 48 h, with or without 700 nM RCR252, and incubated with EdU for 2 h prior to flow cytometry analysis. EPCR blockade did not change the percentage of cells in each phase of the cell cycle compared to control cells (Figures 23B and 23C).

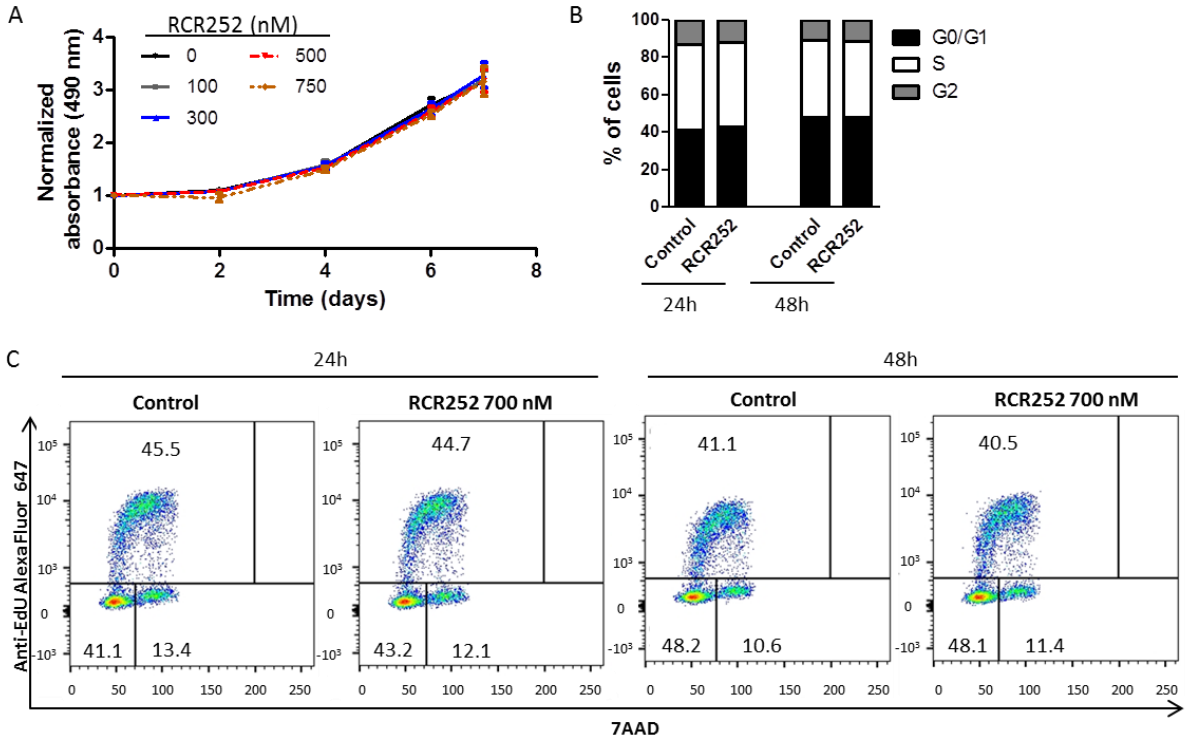

Figure 23. Effects of EPCR blockade by an anti-ECPR antibody (RCR252) on proliferation of 1833 cells. A. *In vitro* proliferation of control and RCR252-treated cells, measured by MTS assay. Data were normalized with the absorbance from day 0. Each dot represents mean ± SD of six replicates from the same experiment. B. Quantification of the percentage of cells in each phase of the cell cycle, by Edu incorporation flow cytometry assay. Cells were maintained in culture for 24 and 48 h. C. Flow cytometry graphs showing cells in each phase of the cell cycle: G0/G1 (lower left), S (upper), G2/M (lower right). Numbers indicate the percentage of cells in each phase.

Accordingly, basal apoptosis levels were not increased when EPCR was blocked (Figure 24). Moreover, RCR252 did not sensitized 1833 cells to TRAIL- or staurosporine-induced apoptosis (Figure 24). IgG-treated cells were included as control in basal and TRAIL-stimulated conditions.

.

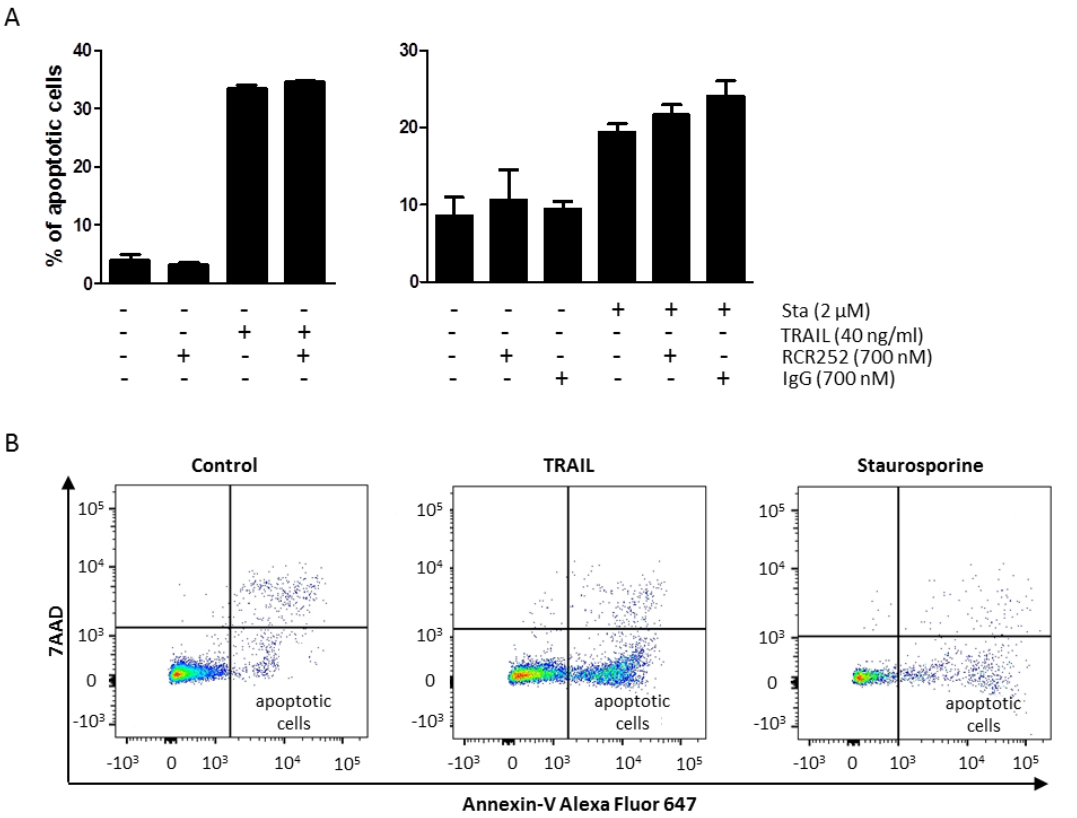

Figure 24. Effects of EPCR blockade by an anti-ECPR antibody (RCR252) on apoptosis of 1833 cells A. Quantification of apoptosis induced by staurosporine and TRAIL in basal and RCR252-treated conditions, determined by annexin-V flow cytometry assay. Data are mean ± SD of triplicates. B. Representative flow cytometry graphs showing gating of apoptotic cells. Apoptotic cells are only stained with annexin-V, while necrotic cells are stained with both annexin-V and 7AAD. Sta, staurosporine.

2.2.2.2. shRNA-mediated EPCR silencing

Next, we silenced EPCR expression levels in the 1833 cell line by lentiviral transduction of different shRNAs (shEPCR#1 and shEPCR#2) targeting EPCR. We also established two control cell lines after lentiviral transduction of empty vector (Vector) and a scramble shRNA that does not target any known human and mouse genes (shControl). EPCR inhibition was assessed by qPCR (Figure 25A), western blot (Figure 25B) and flow cytometry (Figure 25C). EPCR mRNA and protein expression were unaffected by Vector and shControl. In contrast, shEPCR#2 was able to completely inhibit EPCR, while low levels remained after shEPCR#1 transduction.

In agreement with previous findings, control and EPCR-silenced cells showed similar basal and staurosporine-induced apoptosis levels, assessed by annexin-V binding flow cytometry assay (Figure 26A). Moreover, the extent of apoptosis induction by TRAIL was even lower in EPCR-silenced cells, assessed by flow cytometry (Figure 26A) and western blot analysis (Figure 26B).

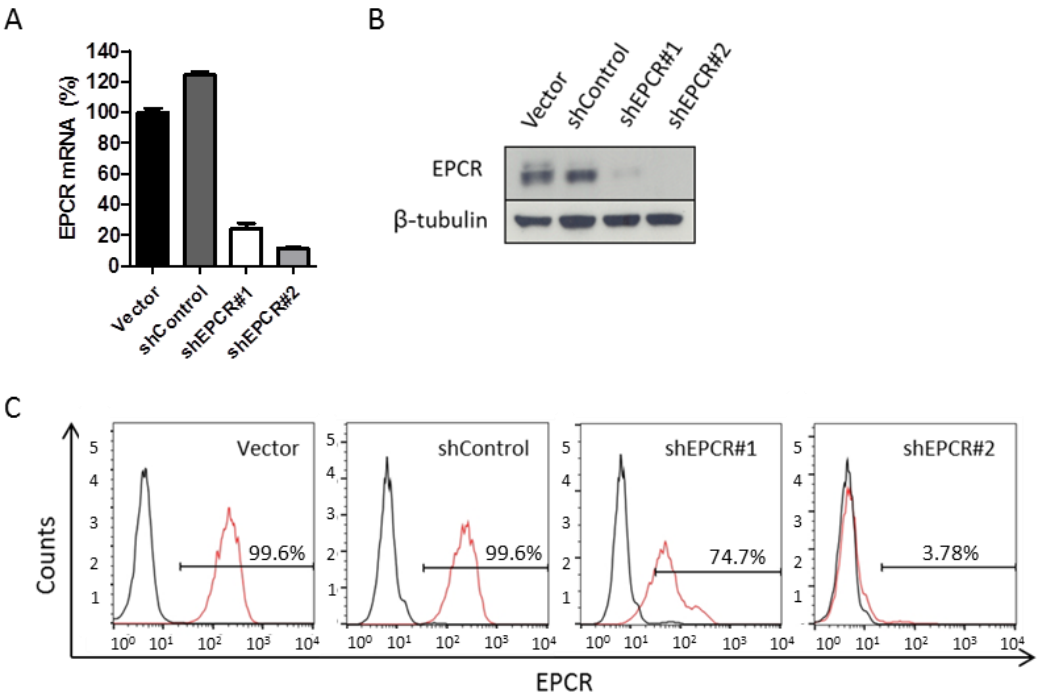

Figure 25. Analysis of EPCR expression in 1833 cells transduced with empty vector (Vector), a scramble shRNA (shControl) and two EPCR-targeting shRNAs (shEPCR#1 and shEPCR#2). A. Detection of mRNA levels of EPCR by qPCR analysis. EPCR expression levels were normalized with GAPDH. B. Detection of EPCR protein levels by western blot. β-tubulin was used as loading control. C. EPCR detection by flow cytometry. Black lines represent the isotype control and red lines EPCR expression. Percentages of cells expressing EPCR are indicated.

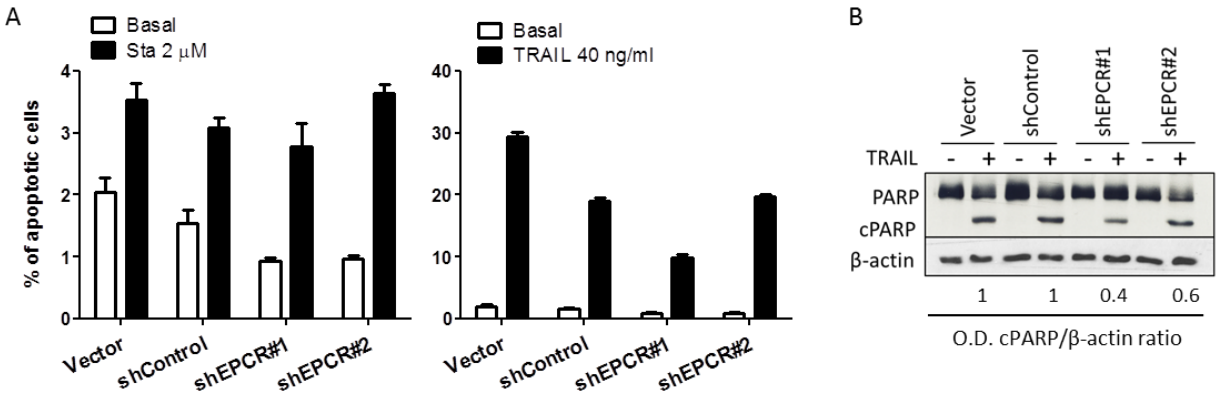

Figure 26. Effects of EPCR silencing on apoptosis of 1833 cells. A. Quantification of apoptosis induced by staurosporine (left) and TRAIL (right), measured by annexin-V binding flow cytometry assay. B. Detection of apoptosis in control and TRAIL-treated cells, by western blot. The amount of apoptosis is proportional to the amount of cleaved PARP (cPARP). β-actin was used as loading control. Numbers indicate quantification (fold-increase) of western blot signals by densitometry. O.D., optical density. Sta, staurosporine.

EPCR knockdown did not reduce growth kinetics of 1833 cells *in vitro*, assessed by MTS proliferation assay for 6 days (Figure 27A). Consistently, cell cycle progression of cells maintained in culture for 24 and 48 h was unaffected by EPCR silencing, assessed by EdU incorporation flow cytometry assay (Figures 27B and 27C).

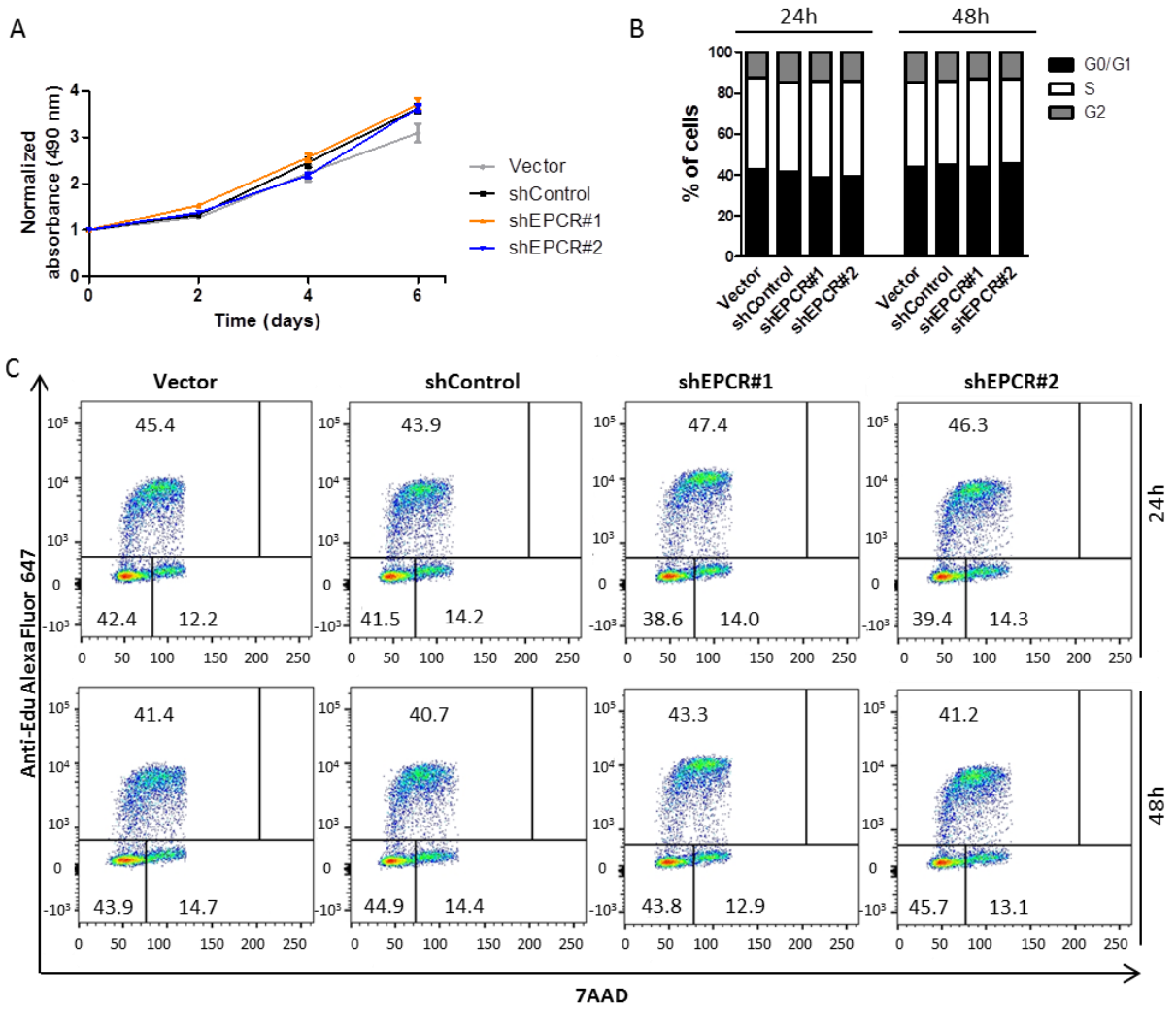

Figure 27. Effects of EPCR silencing on proliferation of 1833 cells. A. MTS *in vitro* proliferation assay. Each dot represents mean ± SD of six replicates of the same experiment. Data are representative of three independent experiments. B. Quantification of cells in each phase of the cell cycle, after maintaining cells in culture for 24 and 48 h. C. Flow cytometry graphs showing cells in each phase of the cell cycle: G0/G1 (lower left), S (upper) and G2/M (lower right). Numbers indicate the percentage of cells in each phase. Top graphs: 24 h in culture. Bottom graphs: 48 h in culture.

2.3. EPCR silencing does not reduce migration and invasion abilities of 1833 cells

To explore the role of EPCR in migration and invasion, 1833 cells were seeded into Boyden chambers with no coating or coated with ECM gel, respectively. EPCR silencing did not reduce the migration and invasion areas after 24 h of incubation (Figure 28).

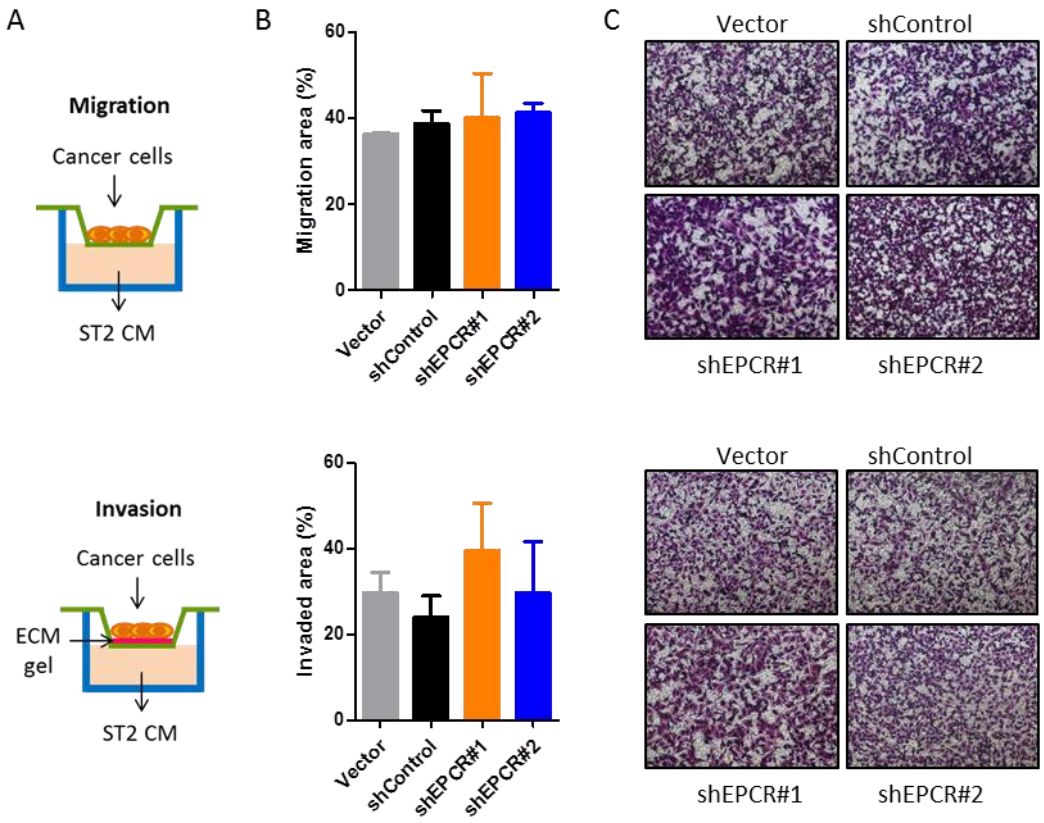

Figure 28. Migration and invasion of control and EPCR-silenced cells. A. Scheme of the migration (top) and invasion (bottom) assays. B. Quantification of migration (top) and invasion (bottom) areas. Data are mean ± SD of triplicates of the same experiment. Data are representative of three independent experiments. C. Representative images of migration (top) and invasion (bottom) areas at 10X magnification.

Overall, these results indicate that EPCR does not mediate cell-autonomous effects on our breast cancer model. Yet, EPCR could be mediating non-cell-autonomous effects *in vivo*.

2.4. EPCR silencing affects tumor growth in a subcutaneous model

In vitro models cannot recapitulate critical heterotypic cellular interactions required for tumor progression[239]. Therefore, we hypothesized that EPCR could be involved in tumor progression *in vivo* by modulating tumor-host interactions.

First, we explored the possible function of EPCR in tumorigenesis. To this end, athymic nude mice (n=6 per group) were subcutaneously inoculated with 500,000 Vector, shControl, shEPCR#1 or shEPCR#2 1833 cells embedded in matrigel. Cells were injected into the right and left dorsal flanks of mice (2 tumors per mouse) and tumor volume was regularly measured using a digital caliper until sacrifice (Figure 29A).

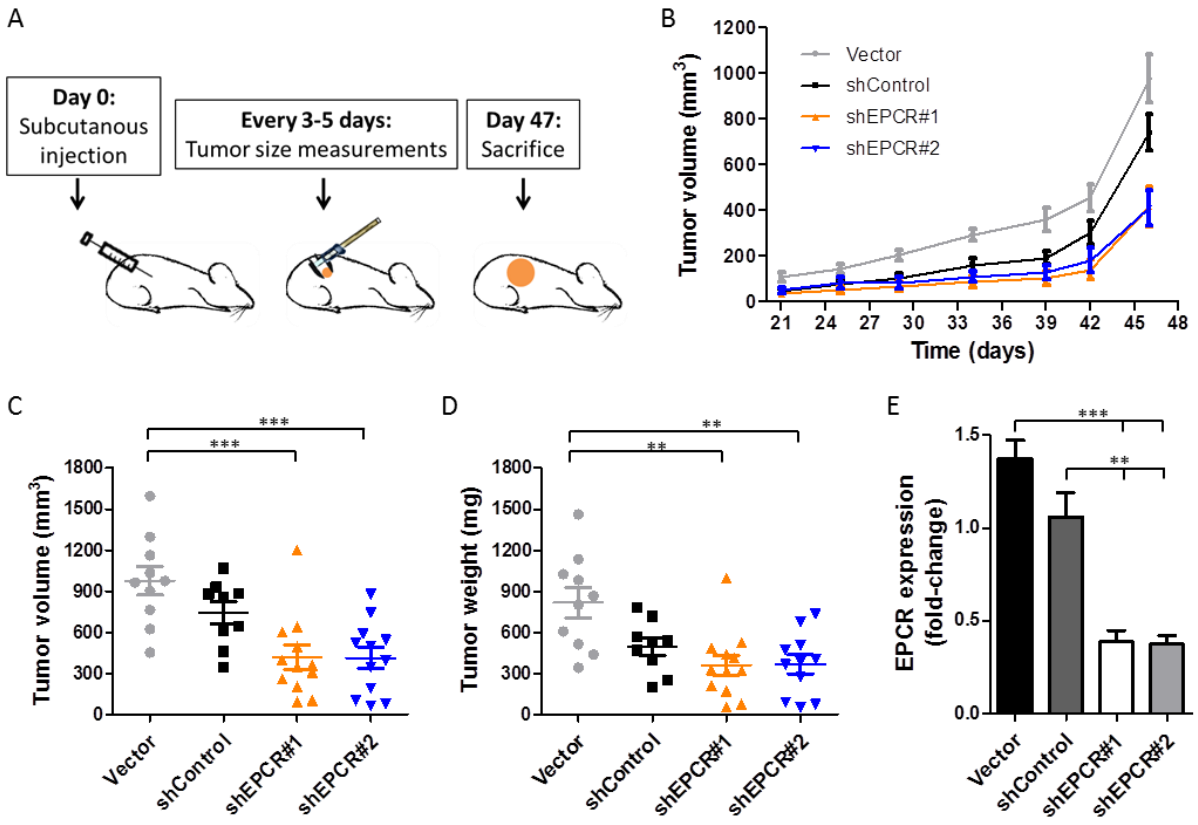

Figure 29. Evaluation of the effect of EPCR silencing in a subcutaneous model. A. Outline of the experiment. B. Tumor volume evolution through the experiment. Each dot represents mean ± SEM. C. Tumor volume at day 47 of the experiment. Each dot represents one tumor. Data are mean ± SEM. D. Tumor weight at day 47 of the experiment. Each dot represents one tumor. Data are mean ± SEM. E. EPCR expression in the tumors (n=9 per group) at the end of the experiment, assessed by qPCR. Normalization was performed with GAPDH. Data are mean ± SEM.

Tumor volume and weight at the final day of the experiment were significantly lower in mice injected with shEPCR#1 and shEPCR#2 cells compared to mice injected with Vector cells (tumor volume: p=0.001; tumor weight: p=0.001 and p=0.003, respectively). Tumors arising from shControl cells were also larger than tumors arising from EPCR-silenced cells, however, those differences were not statistically significant (tumor volume: p=0.087 and 0.079; tumor weight: p=0.68 and p=0.56; for shEPCR#1 and shEPCR#2, respectively) (Figures 26B, 26C and 26D). Necrotic tumors (2 in Vector group and 3 in shControl group) were excluded from the analyses. EPCR silencing was maintained until the end of the experiment (p<0.001, compared to Vector; p=0.003, compared to shControl) (Figure 29E). Interestingly, the two smallest tumors in shControl group had lower EPCR expression levels (data not shown). In the same line, tumor size correlated positively (not statistically significant) with EPCR expression levels in Vector group, where variability in tumor size was high (data not shown). Of note, the largest tumor in shEPCR#1 group maintained EPCR silencing. These results suggest that EPCR silencing affects tumor growth *in vivo*.

2.5. EPCR silencing reduces primary tumor growth and development of spontaneous metastases in an orthotopic model

Next, we explored whether EPCR silencing could reduce tumor growth in an orthotopic model, which better recapitulates the complexity of tumor-host interactions. We also sought to investigate whether EPCR silencing could reduce the incidence of spontaneous metastases. Vector, shControl, shEPCR#1 or shEPCR#2 1833 cells (500,000 cells in matrigel) were injected into the fourth mammary fat pads of athymic nude mice (n=8 per group). Tumor growth was monitored regularly using a digital caliper and tumors were resected at different time points when they reached the established size (V=300 mm^3). Tumors from each mouse were resected at the same time. The development of metastatic events was followed by bioluminescence imaging (BLI) once a week until sacrifice of mice at day 108 post-injection (Figure 30A).

We observed that EPCR knockdown very significantly reduced primary tumor growth ($p<0.001$, compared to shControl; $p=0.005$ and $p<0.001$, compared to Vector for shEPCR#1 and shEPCR#2, respectively) (Figure 30B). Consistently, tumors from mice injected with Vector and shControl cells were resected earlier than tumors derived from EPCR-silenced cells ($p<0.001$), showing that control tumors maintained higher proliferation rates over the course of the experiment (Figure 30C). Moreover, one tumor from shEPCR#1 group and four tumors from shEPCR#2 group did not reach the size established for tumor resection by the end of the experiment (Figure 30C). We started measuring palpable tumors by day 15 post-injection. At that point, the tumor uptake was 31 out of 32 mammary glands in both control groups and 26 out of 32 in both EPCR-silenced groups (non-significant differences). By day 23, only 3 tumors from the shEPCR#1 group remained non-palpable. Indeed, those tumors did not develop during the time course of the experiment (Figure 30D). Overall, these results confirm that EPCR promotes primary tumor growth in our breast cancer model.

After tumor resection, we monitored the regrowth of primary tumors and the development of metastases by BLI once a week. There were not statistically significant differences in the number of relapsed tumors between control and EPCR knockdown conditions (Figure 30D). Tumor relapse could arise from an incomplete resection of the primary tumor or from re-seeding of circulating tumor cells[240], a process that could be favored during tumor resection.

However, the number of mice with metastasis and the number of metastatic foci in mice injected with EPCR-silenced cells was significantly lower compared to control groups, $p=0.011$ and $p=0.028$, respectively (Figure 30D). Since the number of metastatic events was low, we grouped Vector- and shControl-injected mice on one hand, and shEPCR#1- and shEPCR#2-injected mice on the other, for statistical analyses. Based on BLI, metastases were localized mainly into the spine and ribs (Figure 30E). Yet, we did not confirm their localization by histological analysis. We also observed that there was no correlation between primary tumor regrowth and development of

metastases. Therefore, these results indicate that EPCR could participate in the metastatic activity of breast cancer cells.

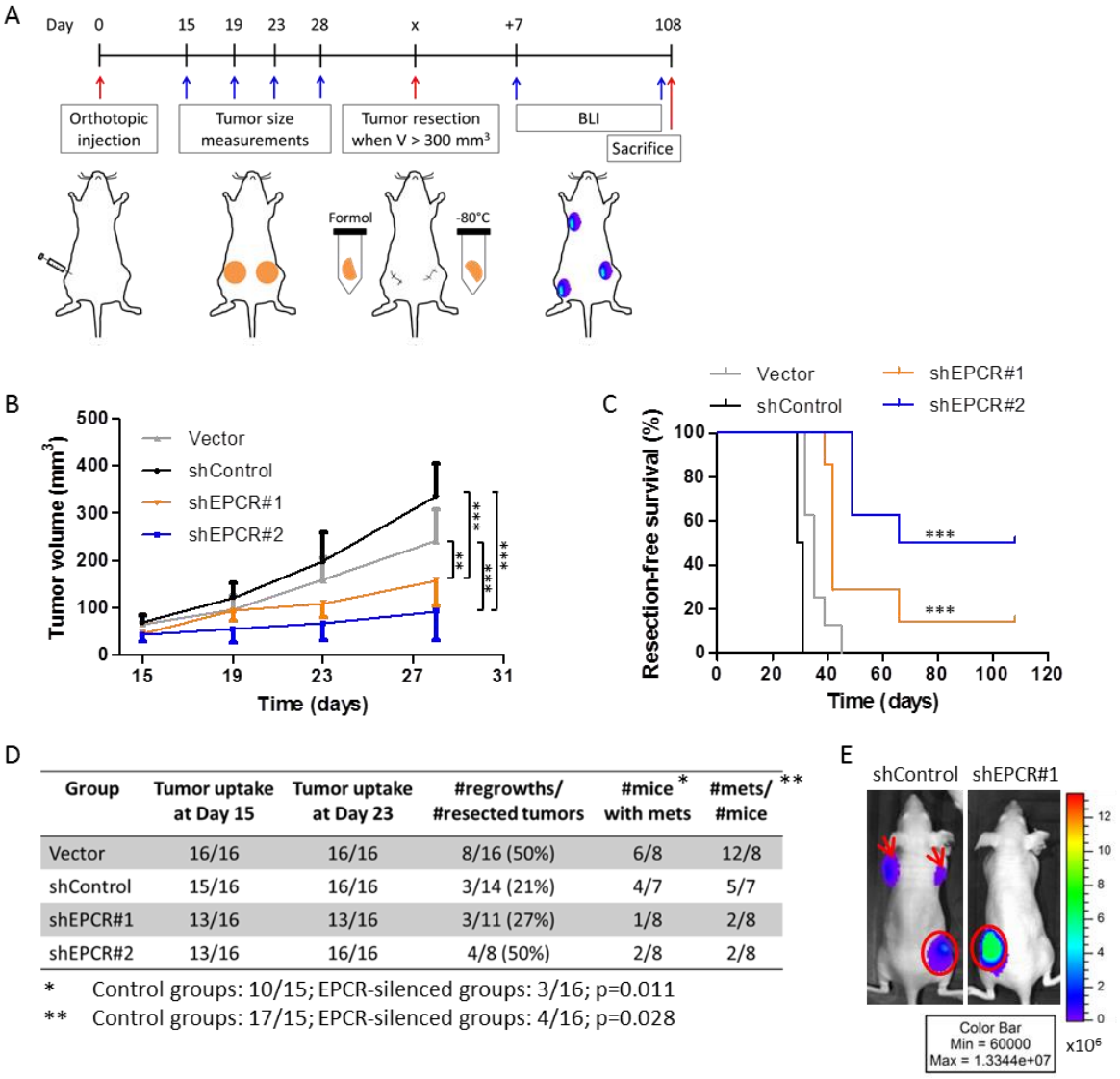

Group	Tumor uptake at Day 15	Tumor uptake at Day 23	#regrowths/ #resected tumors	#mice * with mets	#mets/ #mice **
Vector	16/16	16/16	8/16 (50%)	6/8	12/8
shControl	15/16	16/16	3/14 (21%)	4/7	5/7
shEPCR#1	13/16	13/16	3/11 (27%)	1/8	2/8
shEPCR#2	13/16	16/16	4/8 (50%)	2/8	2/8

* Control groups: 10/15; EPCR-silenced groups: 3/16; p=0.011
** Control groups: 17/15; EPCR-silenced groups: 4/16; p=0.028

Figure 30. Effects of EPCR silencing in primary tumor growth and incidence of metastatic events in an orthotopic model. A. Outline of the experiment. B. Tumor volume quantification until day 28 post-injection. Each dot represents mean ± SEM. C. Kaplan-Meier curves of resection-free survival. D. Incidence of tumor uptake, tumor regrowth and metastatic events. E. Representative images showing tumor regrowth and metastases, assessed by BLI. Arrow, metastatic event. Circle, tumor regrowth.

To explore the cellular mechanisms mediating EPCR-driven primary tumor growth, we performed immunohistochemistry of several markers in fixed tumors. Tumors derived from shControl cells were not included in the analysis (all of them were frozen). We evaluated the following markers: Ki67 (proliferation), cleaved caspase-3 (apoptosis), CD31 (angiogenesis) and F4/80 (infiltration of macrophages). We also quantified necrotic tumor area in H&E sections. Ki67 staining showed

that there were slightly less proliferating cells in tumors derived from shEPCR#2 cells compared to tumors derived from Vector cells. However, those differences were not statistically significant.

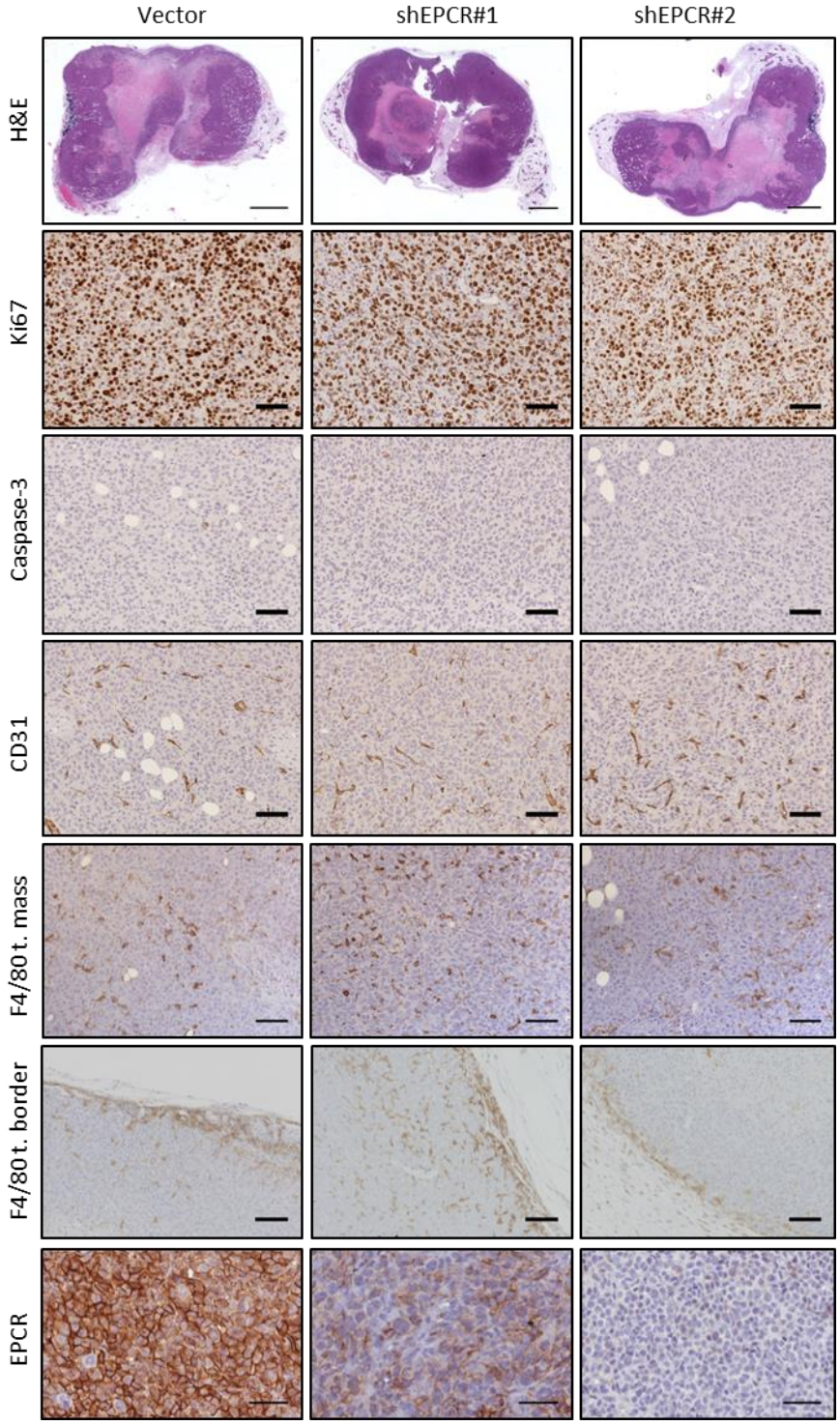

Figure 31. Immunohistochemical analysis of several markers in formalin-fixed mammary tumors. Representative images at 20X magnification showing the staining of H&E, Ki67, caspase-3, CD31, F4/80 in tumor mass (t.mass), F4/80 in tumor border (t. border) and EPCR. Scale bars: 200 mm (H&E), 200 µm (Ki67, caspase-3 and CD31), 70 µm (F4/80) and 100 µm (EPCR).

We also detected more cell death in shEPCR tumors; larger necrotic areas in shEPCR#2 tumors and more cleaved caspase-3 positive cells in shEPCR#1 tumors. Yet, those differences were not statistically significant. We did not find differences in CD31 staining between groups. Finally, we analyzed F4/80 staining in tumor mass and tumor border areas. We found less macrophages in the tumor mass area of shEPCR#2 tumors, but those differences were not statistically significant. Similarly, there were no differences in the infiltration of macrophages into the tumor border area of control and EPCR-silenced tumors. Immunohistochemistry of EPCR revealed that its inhibition by shRNAs was maintained until the end of the experiment, but intriguingly, there were some regions showing EPCR loss in control groups (it is discussed later) (Figures 31 and 32).

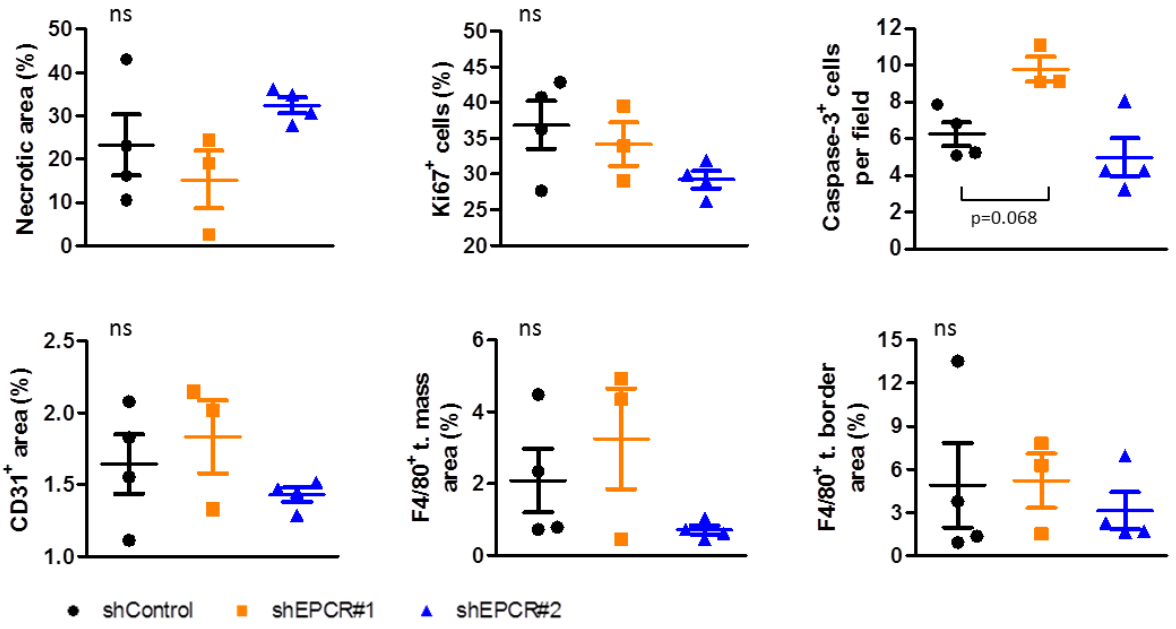

Figure 32. Quantification of the percentage of immunoreactive cells in formalin-fixed mammary tumors. Each dot represents one tumor. Data are mean ± SEM. T. mass, tumor mass. T. border, tumor border.

2.6. Evaluation of the cellular mechanisms mediating EPCR-driven tumorigenesis

Next, we investigated the mechanisms underlying EPCR effects based on the fact that:

- Previous immunohistochemical analyses were carried out in tumors resected at same size but different time points. We hypothesized that more relevant information would be drawn from tumors resected at the same time point, when prominent differences in tumor size were detected.

- Moreover, cancer cells can generate a tumor-supportive microenvironment, in part, by inducing the tumor-promoting role of immune cells recruited into tumors[45,63]. EPCR expressed on endothelial cells exerts anti-inflammatory effects modeling cytokine production and leukocyte

infiltration into damaged organs[241,242]. We speculated that EPCR on cancer cells could be promoting tumor growth by modulating infiltration of immune cells into tumors.

To validate these hypotheses, we injected 500,000 Vector, shControl, shEPCR#1 or shEPCR#2 1833 cells resuspended in PBS into the fourth mammary fat pads of athymic nude mice (n=5 per group). At day 32 post-injection, mice were sacrificed and tumors were collected. From each mouse, one tumor was formalin-fixed for immunohistochemical analyses and the other tumor was FACS-sorted for the characterization of tumor-infiltrating immune cells (Figure 33A). Tumors derived from EPCR-silenced cells were significantly smaller than tumors derived from control cells at the time of resection ($p<0.001$ compared to Vector; $p=0.002$ and $p=0.003$ compared to shControl for shEPCR#1 and shEPCR#2, respectively) (Figure 33B). Of note, tumor growth kinetics was significantly slower in all groups as compared to the previous orthotopic experiment since cells were injected without matrigel.

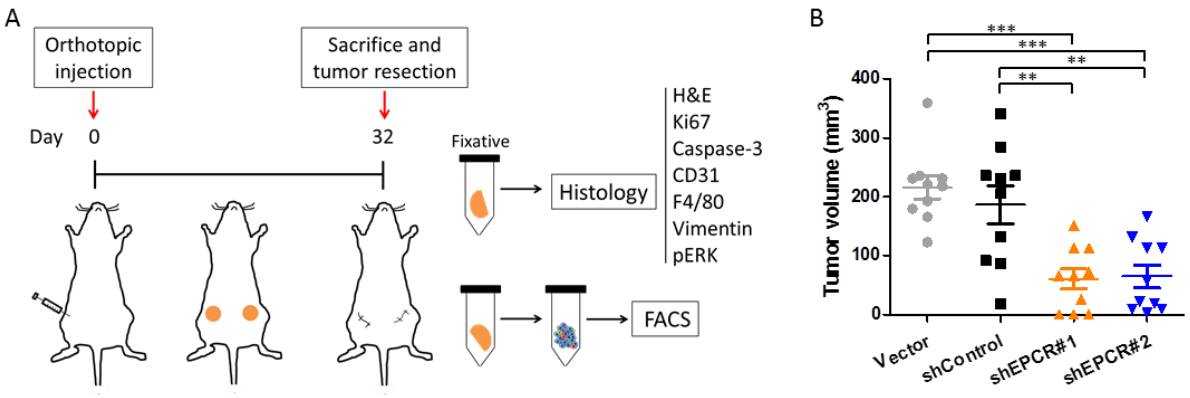

Figure 33. Analysis of immune cells infiltrating mammary tumors derived from control and EPCR-silenced cells. A. Outline of the experiment. B. Tumor volume at the end of the experimental period. Each dot represents one tumor. Data are mean ± SEM.

To dissect tumor-infiltrating immune subpopulations, we used several combinations of antibodies against CD45, CD19, Nkp46, CD11b, MHCII, Ly6G and Ly6C surface antigens. We did not analyze T cell markers since the experiment was performed in athymic nude mice, which lack T cells. Dead cells were excluded of the analysis by 7AAD staining and cell populations were gated on live cells as follows: $CD45^+$ $CD19^+$ (B cells), $CD45^+$ $Nkp46^+$ (NK cells), $CD45^+$ $CD11b^+$ $MHCII^+$ (DCs and macrophages), $CD45^+$ $CD11b^+$ $Ly6G^+$ $Ly6C^-$ (neutrophils), $CD45^+$ $CD11b^+$ $Ly6G^+$ $Ly6C^+$ (inflammatory monocytes) and $CD45^+$ $CD11b^+$ $Ly6G^+$ $Ly6C^+$ (MDSCs) (Figure 34A).

The percentage of $CD45^+$ leukocytes was similar in tumors derived from control and EPCR-silenced cells: around 15%. $CD11b^+$ $MHCII^+$ cells, which can be macrophages and/or DCs, were the most abundant immune cells and accounted for around 50% of leukocytes in tumors from all groups (Figure 34B). Monocytes were the next most abundant immune cell type, followed by

MDSCs. We found more monocytes and MDSCs in tumors from Vector group compared to other groups, but those differences were not statistically significant (Figure 34B). Interestingly, we did not detect neutrophils in the tumors, indicating that they do not play an important role in tumor progression in our model, at least at the time point of the analysis (Figure 34A). NK cells accounted for less than 1% of leukocytes in tumors from all groups and the numbers were similar between groups (quantification not shown). Similarly, we did not detect B cells (Figure 34A). Again, this could indicate that these cell types are not relevant for tumor progression in this model at the time point studied. Overall, these results indicate that EPCR is not significantly involved in the recruitment of immune cells into tumors.

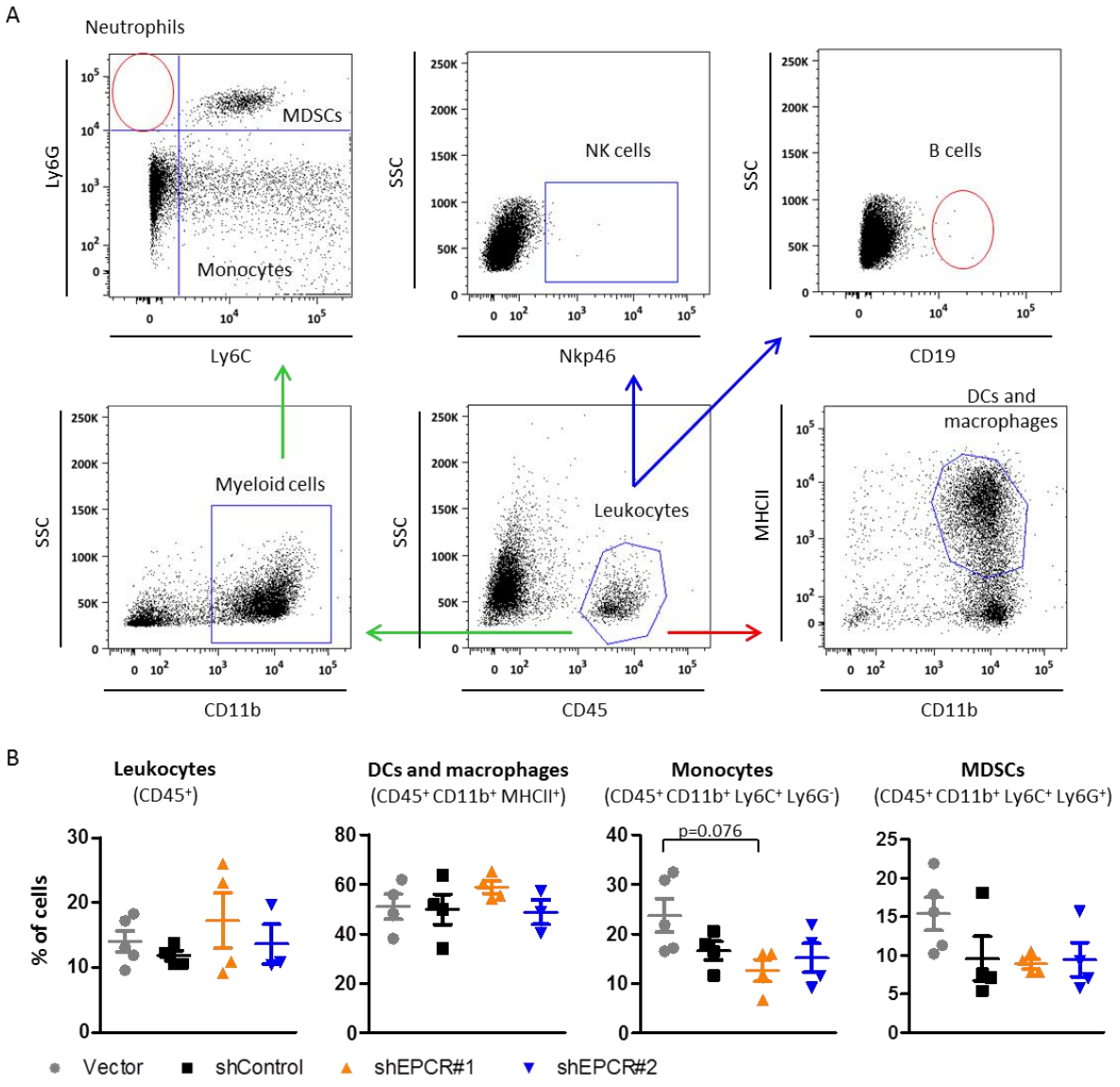

Figure 34. Analysis of immune cells infiltrating mammary tumors derived from control and EPCR-silenced cells. A. Flow cytometry gating strategy. Arrows of the same color indicate simultaneous detection of markers. B. Quantification of the percentage of immune subpopulations infiltrating the tumors. Each dot represents one tumor. Data are mean ± SEM.

On the other hand, we performed an immunohistochemical analysis of several markers in formalin-fixed tumors (Figure 35).

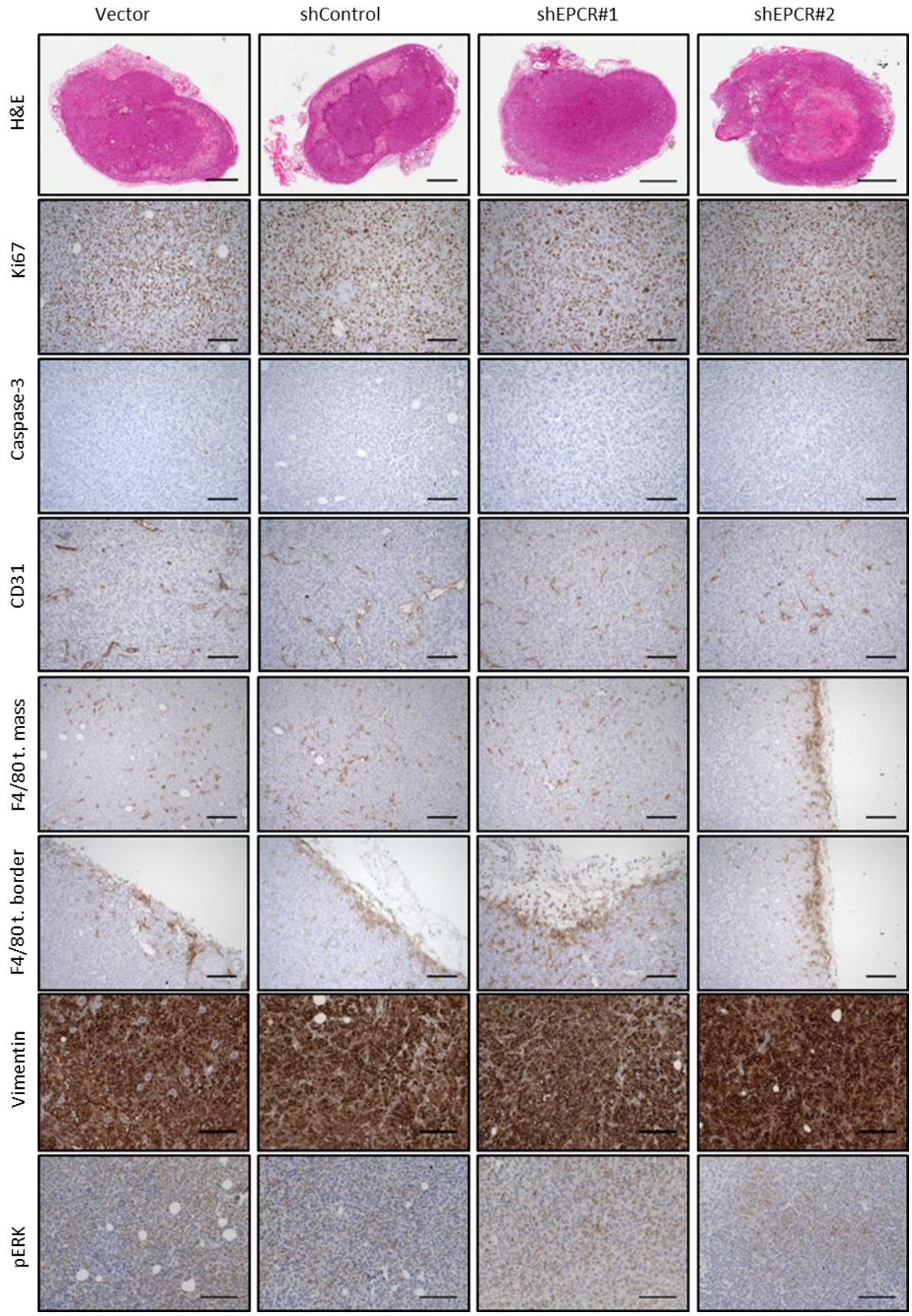

Figure 35 (←). Immunohistochemical analysis of several markers in formalin-fixed mammary tumors. Representative images at 20X magnification showing the staining of H&E, Ki67, caspase-3, CD31, F4/80 in tumor mass (t. mass), F4/80 in tumor border (t. border), vimentin and pERK. Scale bars: 20 mm (H&E), 80 mm (Ki67, caspase-3, CD31, F4/80) and 100 mm (vimentin and pERK).

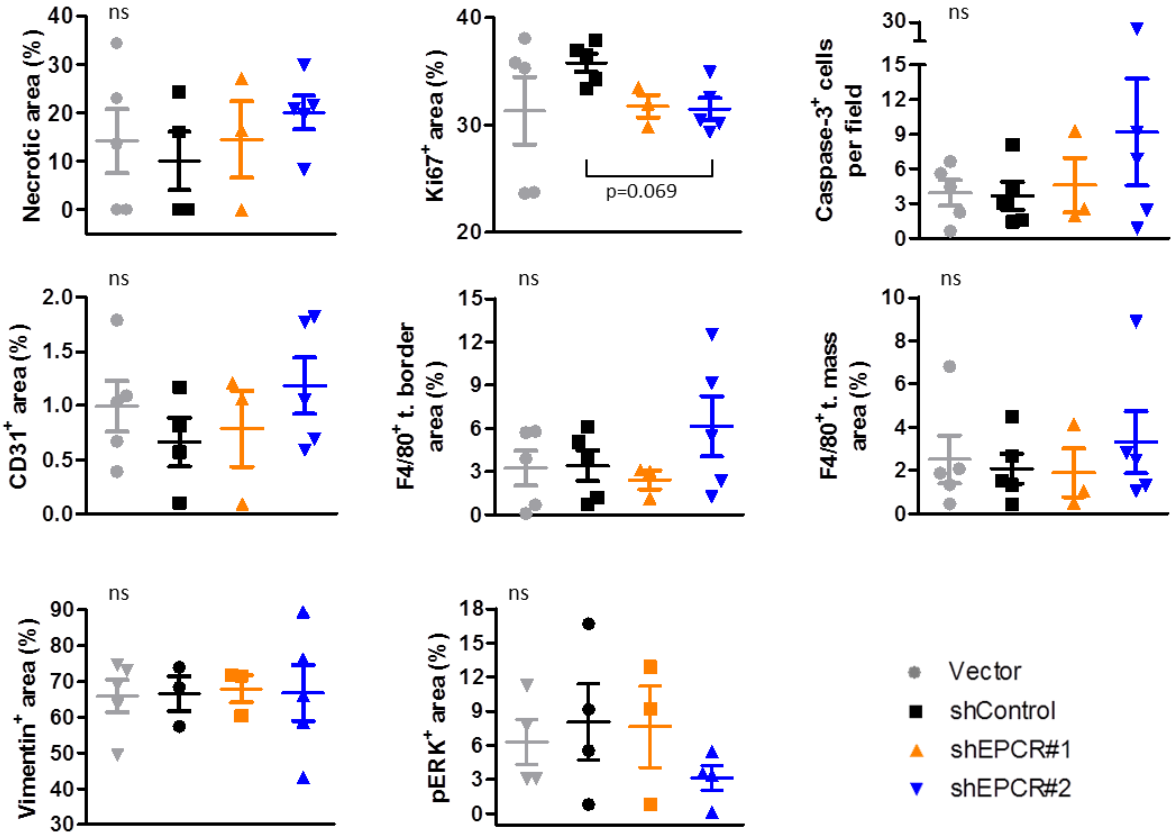

Figure 36. Quantification of the percentage of immunoreactive cells. Each dot represents one tumor. Data are mean ± SEM. T. mass, tumor mass. T. border, tumor border.

Interestingly, we observed less proliferating cells (Ki67 staining) in EPCR knockdown tumors, compared to shControl tumors. However, those differences were not statistically significant. Cell death in tumors was unaffected by EPCR silencing, assessed by quantification of tumor necrotic area in H&E sections and the number of active caspase-3 positive cells. We also analyzed angiogenesis by CD31 staining. Surprisingly, despite the notable difference in tumor size between control and EPCR-silenced groups, we did not find differences in CD31 staining between groups. In agreement with data obtained in the flow cytometry experiment, the number of macrophages (F4/80$^+$ staining) infiltrating the tumor mass and tumor border areas was similar in all groups. Finally, we evaluated vimentin and pERK expression as markers of EMT and tumor dormancy, respectively. We observed no differences between groups for both markers (Figure 36). Importantly, EPCR inhibition by shRNAs was maintained until the end of the experimental period (data not shown).

2.7. Analysis of tumor-stroma interactions in co-culture models *in vitro*

Although EPCR silencing did not have an impact on the recruitment of immune cells into mammary tumors, EPCR could still play a role in the interaction of cancer cells with other stromal components. To explore this possibility, we analyzed proliferation of Vector, shControl, shEPCR#1 and shEPCR#2 1833 cells in co-culture with ST2 murine bone marrow stromal cells or WI38 human fibroblasts. To this end, we determined the luciferase activity of cancer cells (transduced with a luciferase vector) in basal (cancer cells alone) and co-cultured conditions.

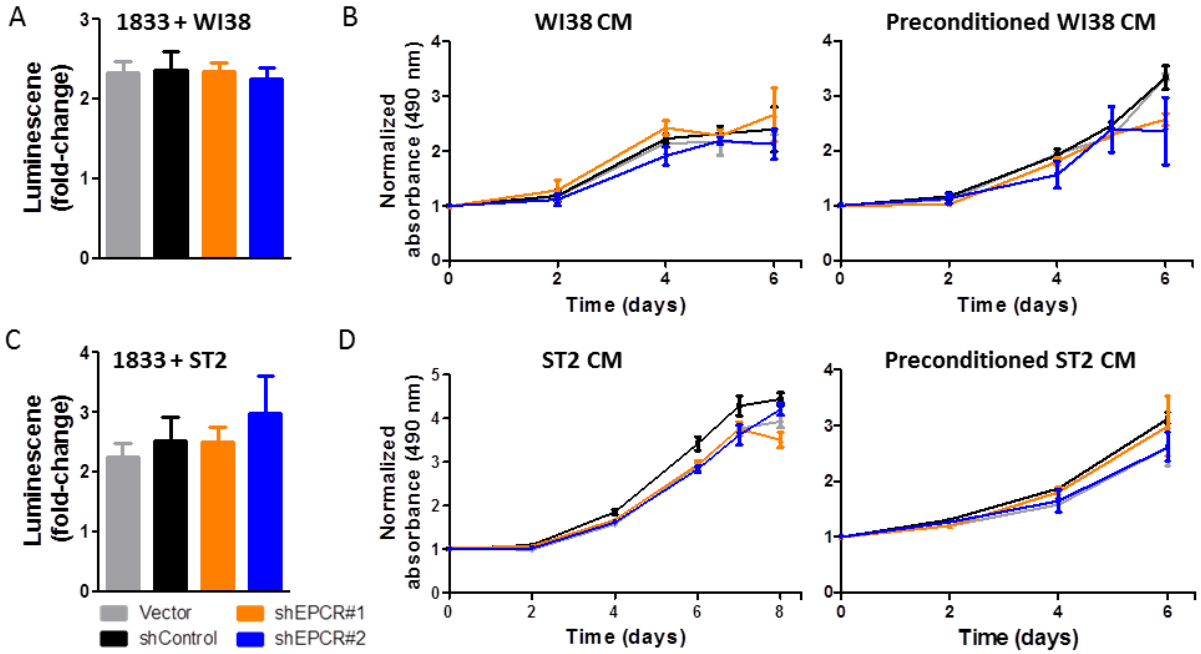

Figure 37. Co-culture experiments of 1833 cells with ST2 murine stromal cells and WI38 human fibroblasts. A. Fold-increase in luciferase activity of 1833 cells co-cultured with WI38 cells for 48 h, as compared to cancer cells alone. Data are mean ± SD of triplicates. B. MTS proliferation assay of 1833 cells cultured in condition medium (CM) derived from WI38 cells (left) or CM from WI38 cells that had been previously incubated with CM from cancer cells (right). Each dot represents mean ± SD of six replicates. C. Fold-increase in luciferase activity of 1833 cells co-cultured with ST2 cells for 72 h, compared to cancer cells alone. Data are mean ± SD of triplicates. D. MTS proliferation assay of 1833 cells cultured in CM from ST2 cells (left) or CM from ST2 previously preconditioned with CM from cancer cells (right). Each dot represents mean ± SD of six replicates.

Co-culturing cancer cells with WI38 fibroblasts at 1:1 ratio for 48 h increased proliferation of cancer cells compared to basal conditions, but to the same extent in both control and EPCR-silenced cells (Figure 37A). We also analyzed proliferation of control and EPCR-silenced cells maintained in conditioned medium (CM) from WI38 cells for 6 days, by MTS assay. All cell lines showed similar cell growth kinetics (Figure 37B). Preconditioning WI38 cells with CM from cancer cells, and culturing cancer cells with CM from those WI38 cells, did not reveal differences in

proliferation between control and EPCR-silenced cell lines maintained in culture for 6 days (Figure 37B).

We performed the same experiments with the ST2 cell line. Cancer cells were cultured alone or with ST2 cells at 5:1 ratio for 72 h. Co-culturing cancer cells with ST2 cells increased proliferation of cancer cells compared to basal conditions, but again, to the same extent in all cell lines (Figure 37C). Consistently, culturing cancer cells in CM from ST2 or preconditioned ST2 cells did not show relevant differences in proliferation between control and EPCR-silenced cells maintained in culture for 6 days, assessed by MTS assay (Figure 37D).

Overall, the lack of mechanistic insights into EPCR function in breast cancer encouraged us to consolidate EPCR effects in additional *in vivo* models.

2.8. shRNA-mediated EPCR silencing results in a dramatic decrease in metastasis

Based on the observation that EPCR silencing reduced the incidence of spontaneous metastases in the orthotopic experiment, we decided to further study the prometastatic activity of EPCR in another *in vivo* model. To this aim, 100,000 shControl, shEPCR#1 or shEPCR#2 1833 cells resuspended in PBS were inoculated into the left cardiac ventricle of athymic nude mice (n=7, n=6 and n=5, respectively) and bone metastases were analyzed by BLI, X-rays, micro-CT scans and histological analysis (Figure 38A). Since 1833 cells have bone tropism, we observed metastases in several skeletal elements of the axial and appendicular skeleton including the spine and long bones. For the sake of simplicity, we focused on the hindlimbs to perform subsequent analyses.

All mice in the shControl group developed metastasis in the hindlimbs (7/7), while 2 mice remained hindlimb metastasis-free in shEPCR#1 (4/6) and shEPCR#2 (3/5) groups (Figure 38B). Moreover, the number of tibiae and femurs with metastasis was significantly lower ($p<0.001$) in mice injected with shEPCR#1 (8/24) and shEPCR#2 (6/20) cells, compared to mice injected with shControl cells (24/27), according to H&E staining of bone sections (Figure 38B).

Consistently, BLI revealed that EPCR silencing significantly reduced the overall extension of metastases ($p<0.001$ and $p=0.002$ for shEPCR#1 and shEPCR#2, respectively) (Figures 38C and 38G) and growth of secondary tumors in hindlimbs ($p<0.001$ and $p=0.016$ for shEPCR#1 and shEPCR#2, respectively) (Figures 38D and 38G). In both cases, those differences were statistically significant from day 13 of the experiment. In contrast, whole-body and hindlimbs bioluminescence (BL) signals were lower in mice injected with shControl cells at day 6 of the experiment (Figures 38C and 38D). This indicates that EPCR promotes tumor growth of cancer cells once they have reached the target organ.

Similarly, tumor area quantification in H&E stained sections of tibiae and femurs revealed that EPCR silencing significantly reduced bone tumor burden ($p=0.005$ and $p=0.017$ for shEPCR#1

and shEPCR#2, respectively) (Figures 38E and 38G). The extension of osteolytic lesions was also significantly reduced in shEPCR groups, quantified in X-ray images from day 28 post-injection (p=0.018 and p=0.043 for shEPCR#1 and shEPCR#2, respectively) (Figures 38F and 38G). Those lesions could also be observed in micro-CT scans (Figure 38G).

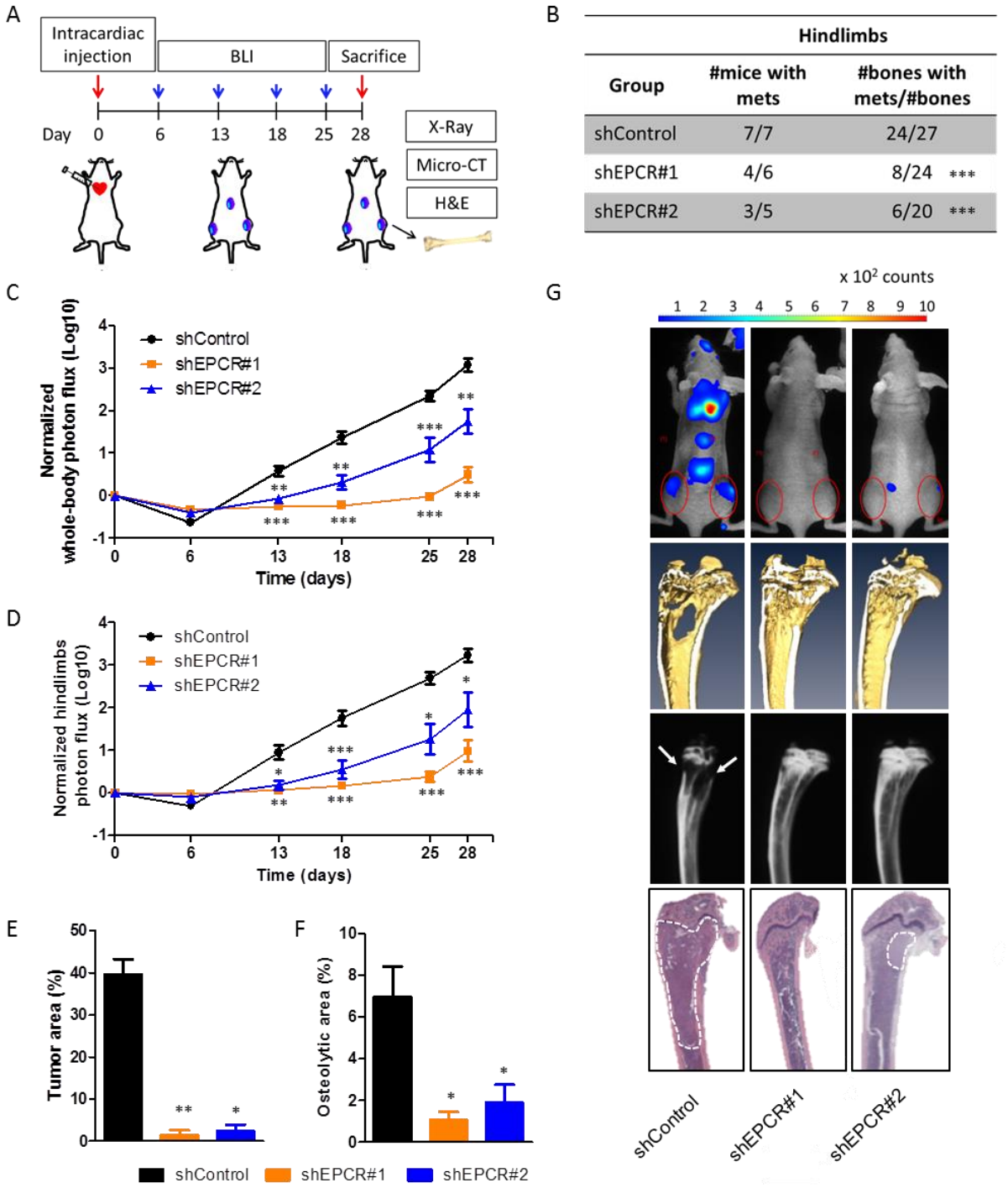

Figure 38. Evaluation of the prometastatic activity of EPCR after intracardiac inoculation of control and EPCR-silenced 1833 cells. A. Outline of the experiment. B. Number of mice and bones with metastasis in each group. C. Whole-body photon flux quantification along the experiment. Data were normalized with BL values from day 0. D. Quantification of BL signals from hindlimbs along the experiment. Data were normalized with BL values

from day 0. E. Tumor area quantification in H&E stained bone sections. F. Osteolytic bone area quantification in X-ray images from day 28 of the experiment. G. Representative images of BLI, micro-CT scans, X-ray scans and H&E staining in bone sections, from top to botton, respectively. All data are mean ± SEM.

Immunohistochemical analysis of bone sections showed no differences in Ki67 and vimentin staining between control and EPCR-silenced tumors (Figure 39). We observed a non-statistically significant increase in the number of active caspase-3 positive cells in shControl tumors (Figure 39). This could be related to the large size of those tumors. We did not perform CD31 staining since the difference in tumor size between groups would preclude obtaining valid conclusions. Importantly, EPCR inhibition by shRNAs was maintained until the end of the experimental period (Figure 39).

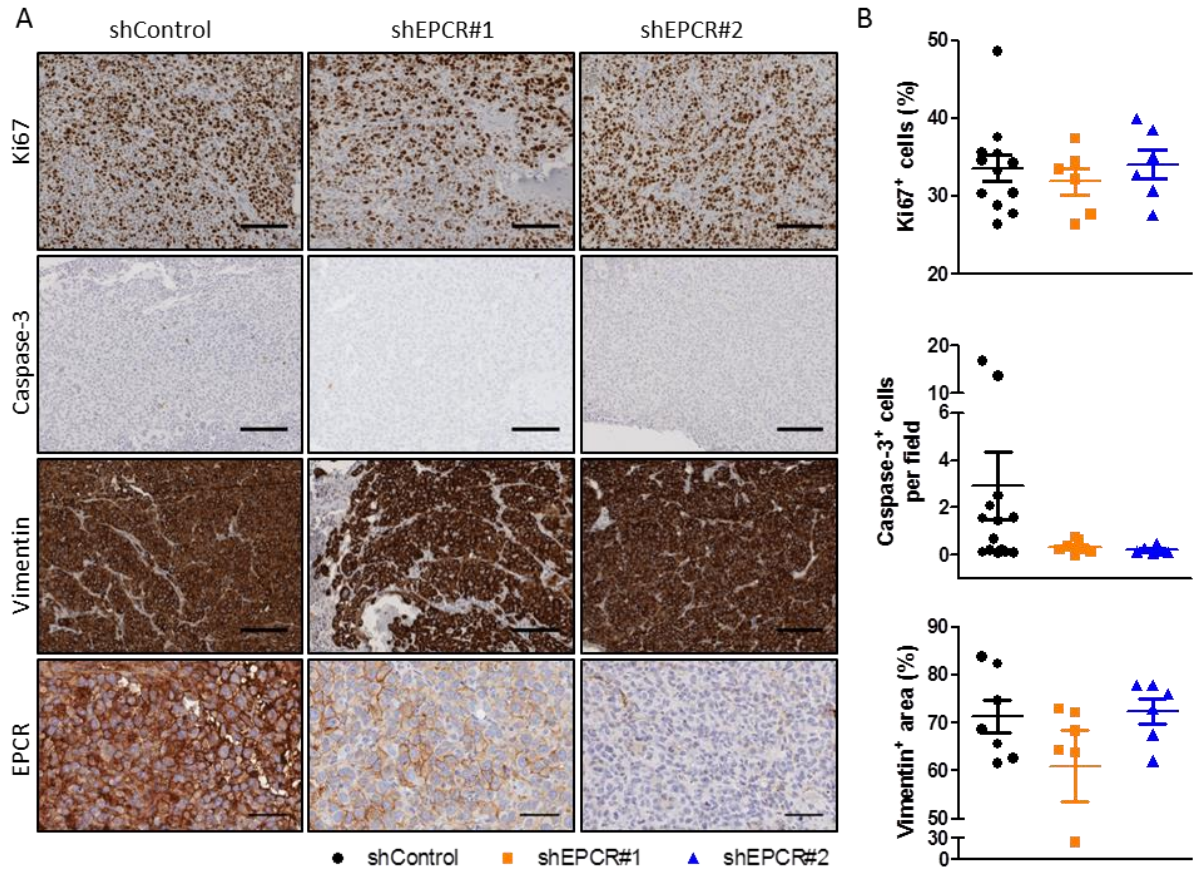

Figure 39. Immunohistochemical analysis in bone sections. A. Representative images at 20X magnification of Ki67, caspase-3, vimentin and EPCR stainings. Scale bars: 100 mm (Ki67, caspase-3 and vimentin) and 100 µm (EPCR). B. Quantification of the percentage of immunoreactive cells. Each dot represents one tumor. Data are mean ± SEM.

These results consolidate the role of EPCR in breast cancer and indicate that EPCR promotes metastatic activity to bone. Moreover, the low incidence of metastatic events in mice injected with shEPCR cells suggests that EPCR is required during metastatic tumor re-initiation.

2.9. shRNA-mediated EPCR silencing reduces bone colonization

Differences in bone metastasis between control and EPCR-silenced cells became more relevant at advanced time points in the previous experiment. To explore the function of EPCR in bone colonization, 15,000 shControl, shEPCR#1 or shEPCR#2 1833 cells resuspended in PBS were inoculated into the tibiae of RAG2$^{-/-}$ mice (n=8 per group). Bone colonization was analyzed by BLI, X-rays and histological analysis (Figure 40).

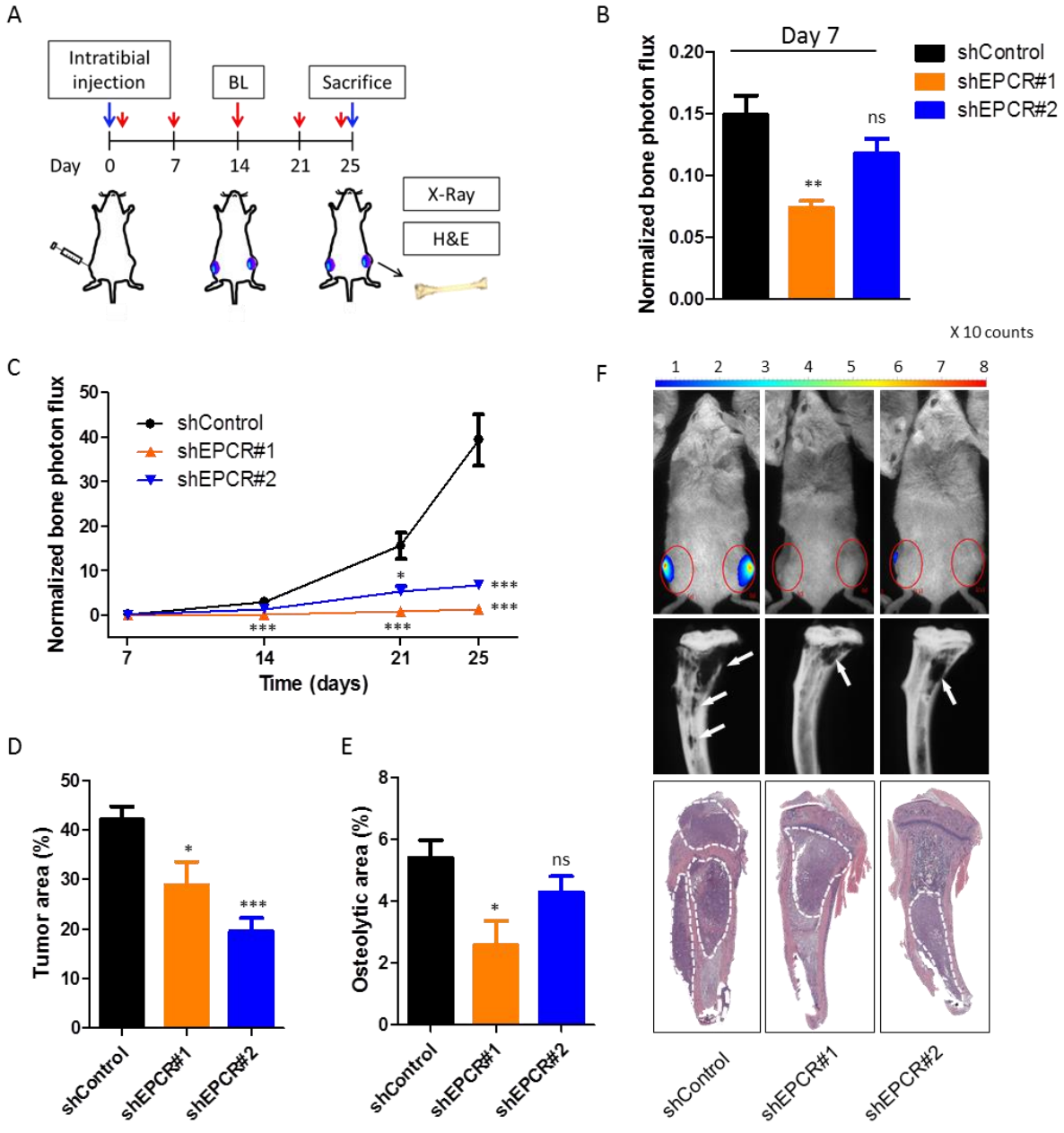

Figure 40. Effects of EPCR silencing in bone colonization. A. Outline of the experiment. B. Quantification of BL in hindlimbs at day 7 post-injection. C. Quantification of BL in hindlimbs along the experiment. D. Quantification of tumor area in bone sections. E. Quantification of osteolytic bone area in X-ray scans from day 25 post-injection. F. Representative images of BLI, X-ray scans and H&E stained bone sections, from top to bottom. All data represented are mean ± SEM.

Tumors developed in all tibiae in shControl and shEPCR#2 mice, while 2 tibiae remained tumor-free in shEPCR#1 group. At day 7 post-injection, there were significant differences in tumor growth between control and shEPCR1 tumors (p=0.001) while a trend was observed in shEPCR2 tumors (Figure 40B). These differences became more relevant at advanced time points of the experiment; p<0.001 for both shEPCR groups at day 25 post-injection (Figures 40C and 40F). Consistently, EPCR silencing resulted in reduced tumor area (p=0.032 for shEPCR#1 and p<0.001 for shEPCR#2), evaluated in H&E stained bone sections (Figures 40D and 40F). Moreover, osteolytic bone area at the end of the experiment was significantly lower in shEPCR#1 group (p=0.01), assessed in X-ray scans (Figures 40E and 40F). These results indicate that EPCR contributes to bone colonization.

2.10. EPCR blockade with RCR252 does not reduce metastasis

To substantiate the role of EPCR in metastasis, we followed a pharmacological inhibition approach to study the prometastatic activity of EPCR.

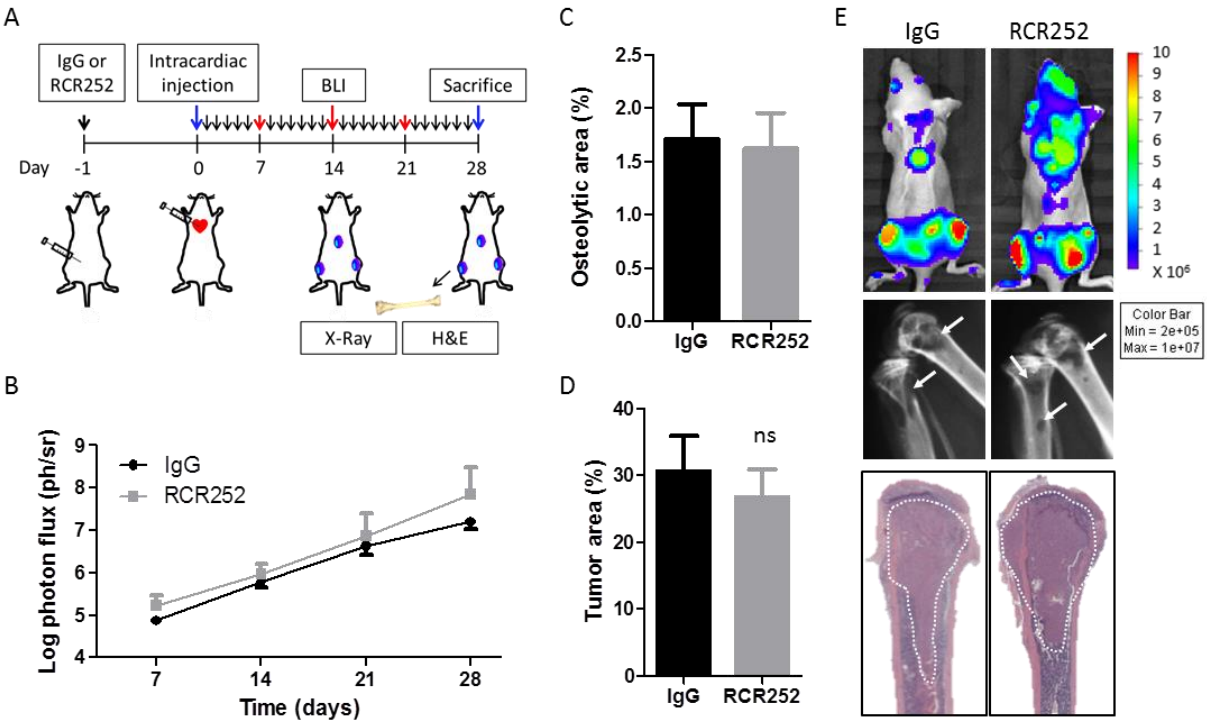

Figure 41. Effects of EPCR blockade in the prometastatic activity of EPCR. A. Outline of the experiment. B. Photon flux quantification in hindlimbs during the course of the experiment. C. Tumor area quantification in H&E stained bone sections. D. Osteolytic bone area quantification in X-ray images from day 28 post-injection. E. Representative images of BLI (top), X-rays (middle) and H&E staining (bottom) at day 28 post-injection. Data are represented by mean ± SEM.

1833 parental cells (100,000 cells in PBS) were intracardiaclly inoculated into athymic nude mice (n=8 per group) treated with control (IgG) or EPCR-blocking (RCR252) antibodies every day from the day before the inoculation of the cells (Figure 41A). As mentioned before, RCR252 blocks APC binding to EPCR and is specific to human EPCR. Of note, *in vitro* binding experiments have shown that murine APC can bind to human EPCR (data not shown). To avoid confounding effects of the complement system, we exclusively used the $F(ab´)_2$ fractions, which retain EPCR blocking properties. EPCR blockade did not reduce bone metastasis, assessed by BLI of hindlimbs during the course of the experiment (Figures 41B and 41E). Consistently, tumor area quantification in H&E sections of tibiae and femurs revealed no differences in bone tumor burden between both groups (Figures 34C and 34E). Osteolytic lesions were also similar in both groups, quantified in X-ray images from day 28 of the experiment (Figures 41D and 41E). These results indicate that EPCR-mediated prometastatic effects are APC-independent.

2.11. Study of the mechanisms involved in the protumorigenic and prometastatic activities of EPCR

Encouraged by the significant effects observed with EPCR silencing in the development of metastasis, we decided to take another approach to explore the mechanisms underlying EPCR effects. To this end, we performed a microarray analysis in shControl, shEPCR#1 and shEPCR#2 tumors from the first orthotopic experiment. These were mammary tumors obtained at different time points and same size. We used the Human Gene 2.0 ST microarray (Affymetrix) to identify genes differentially expressed in control and EPCR-silenced cells *in vivo*. Yet, we cannot discard the possibility that cross-hybridization of murine transcripts from tumor stroma could also occur.

We compared shControl and shEPCR#1 tumors on one hand and shControl and shEPCR#2 tumors on the other, and selected differentially expressed genes that were common to both analyses: 74 upregulated genes and 16 downregulated genes (Figure 42A). Next, we performed functional and pathway analysis on those genes using Ingenuity Pathway Analysis software (IPA®, QIAGEN Redwood City, www.qiagen.com/ingenuity). EPCR-silenced tumors had positive activation scores for death, contact growth inhibition and senescence functions, while had negative activation scores for proliferation, migration, invasion, EMT, angiogenesis, adhesion and lipid metabolism functions. However, only three death-related functions had statistically significant activation scores (z-score <-2 or >2): organismal death, cell death of breast cancer cell lines and necrosis (Figure 42B). In addition, several metabolic pathways were altered in EPCR-silenced cells (Figure 42C). To further analyze the molecular mechanisms that could be mediating EPCR effects, we selected the genes that displayed the highest fold-decrease scores among the genes that have been related to tumor progression in the literature (Figure 42D).

A

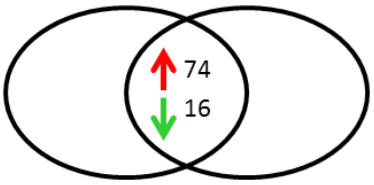

B

Function	p-value	z-score	# genes
Organismal death	1,19E-03	3,26	25
Cell death of breast cancer cell lines	2,47E-02	2,196	5
Necrosis	1,36E-02	2,11	23
Cell death of tumor cell lines	9,73E-03	1,681	16
Cell death	1,95E-03	1,655	31
Apoptosis	9,59E-03	0,382	24
Contact growth inhibition	5,37E-03	1,177	4
Proliferation of tumor cells	1,25E-02	-0,522	7
Tumorigenesis of tumor cell lines	6,37E-03	-0,762	4
Proliferation of cells	4,92E-03	-0,92	32
Growth of tumor	7,42E-03	-1,019	10
Tumorigenesis of cells	6,56E-03	-1,109	5
Growth of organism	1,28E-02	-1,98	10
Senescence of cells	2,88E-02	0,688	4
Migration of tumor cell lines	2,47E-02	-0,729	8
Migration of connective tissue cells	1,06E-02	-1,029	4
Cell movement of tumor cell lines	1,18E-02	-1,354	10
Cell movement	2,33E-03	-1,572	22
Cell spreading	1,26E-02	-1,715	5
Invasion of breast cancer cell lines	5,43E-03	-1,432	5
Binding of cells	1,37E-02	-1,432	7
Epithelial-mesenchymal transition	1,30E-02	-0,686	4
Concentration of lipid	1,42E-02	0,318	10
Synthesis of lipid	1,65E-02	-1,943	9
Fatty acid metabolism	2,92E-02	-1,951	7
Angiogenesis	2,57E-02	-0,992	10

C

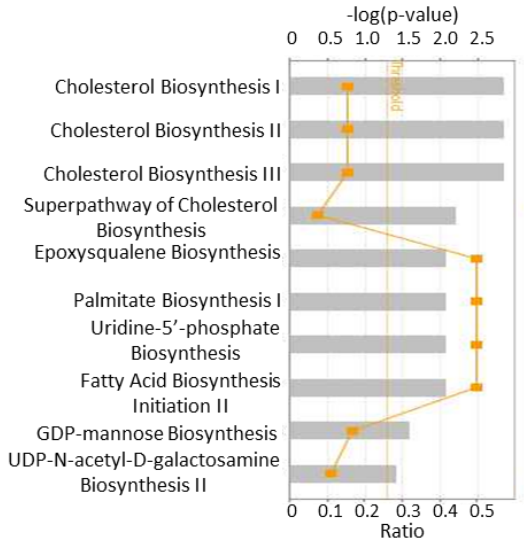

D

Gene	logFC in 1	logFC in 2	Related functions
FZD8	-1.10	-1.25	Angiogenesis, proliferation
ITGB4	-0.47	-1.60	Death, migration, invasion, angiogenesis, binding, proliferation
KRT19	-0.51	-1.11	Invasion, migration, death, proliferation
FLNB	-0.44	-1.29	Migration, angiogenesis, death
FLNC	-1.05	-0.90	Migration, death
SPOCK1	-0.58	-1.33	Death, proliferation
HSPA1A	-0.64	-2.64	Death, proliferation
HSPA1B	-0.60	-2.47	Death, proliferation, migration, senescence
ITPR3	-0.53	-1.72	Death, proliferation

Figure 42. Microarray analysis of mammary tumors derived from mice injected with control and EPCR-silenced cells. A. Number of upregulated (in red) and downregulated (in green) genes in both shEPCR#1 and shEPCR#2 tumors compared to shControl tumors. B. Functional annotations with increased or decreased activation scores in EPCR-silenced tumors. Functions with statistically significant activation scores are highlighted in red. C. Metabolic pathways differentially activated between control and EPCR-silenced tumors. D. A selection of genes that showed the highest fold-decrease values in shEPCR#1 (logFC in 1) and shEPCR#2 (logFC in 2) tumors among the genes related to tumor progression. Functions annotated for these genes in Ingenuity® are also listed.

Next, we analyzed the expression of the selected genes (Figure 42D) *in vitro* (Figure 43A). In addition, in order to validate the expression changes observed in mammary tumors and select the most robust genes, we analyzed the expression of the selected genes in subcutaneous tumors from an independent *in vivo* experiment. SPOCK1 (p=0.038 and p=0.013 for shEPCR#1 and shEPCR#2, respectively) and FZD8 (non-significant) were the only genes that were also downregulated in both EPCR-silenced conditions in these samples (Figure 43B). Interestingly, they were also downregulated *in vitro* (Figure 43A).

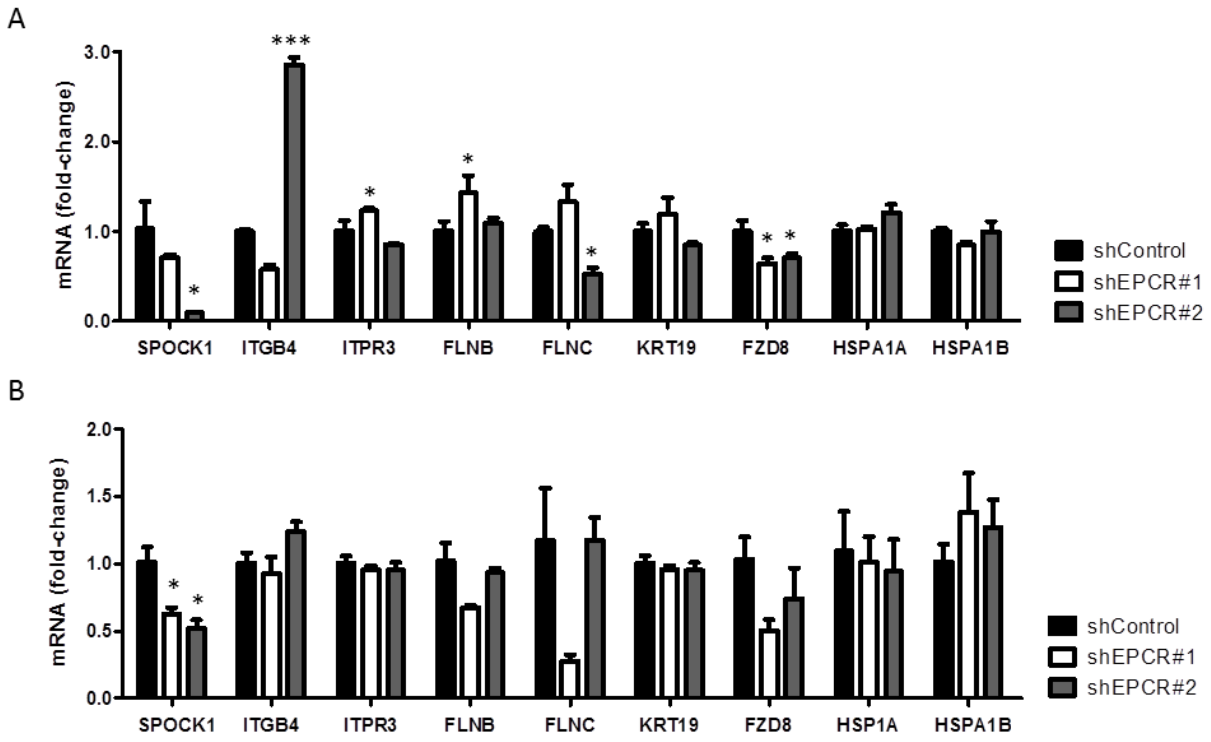

Figure 43. Validation of the genes selected from the microarray analysis, by RT-qPCR. A. Relative expression levels of the genes indicated *in vitro*. Data are mean ± SD of triplicates B. Relative expression levels of the genes indicated in subcutaneous 1833 tumors. Data are mean ± SEM of 3 tumors per group.

We also explored whether patients with high EPCR expression from the GSE2034 cohort had higher expression levels of these genes. We found that patients with high EPCR expression levels also had higher SPOCK1 expression levels ($p<0.001$). However, the expression levels of the other genes were similar or even lower in patients with high EPCR expression levels (Figure 44A).

Therefore, we decided to analyze if SPOCK1 could predict the clinical outcome of patients from the GSE2034 database. We did not observe an statistically significant correlation between SPOCK1 expression levels and clinical outcome when all patients from the GSE2034 database were included in the analysis ($p=0.18$) (Figure 44B). Similarly, SPOCK1 expression levels did not correlate to clinical outcome in luminal A subgroup (Figure 44C). However, patients with high SPOCK1 levels had significantly shorter-relapse free survival times in patients from luminal B, basal-like and HER2 subsets ($p=0.0043$) (Figure 44C). Interestingly, these data are consistent with the predictive potential of EPCR levels in these three subsets, but not in luminal A. This suggests that EPCR could mediate tumor progression in part by upregulating SPOCK1.

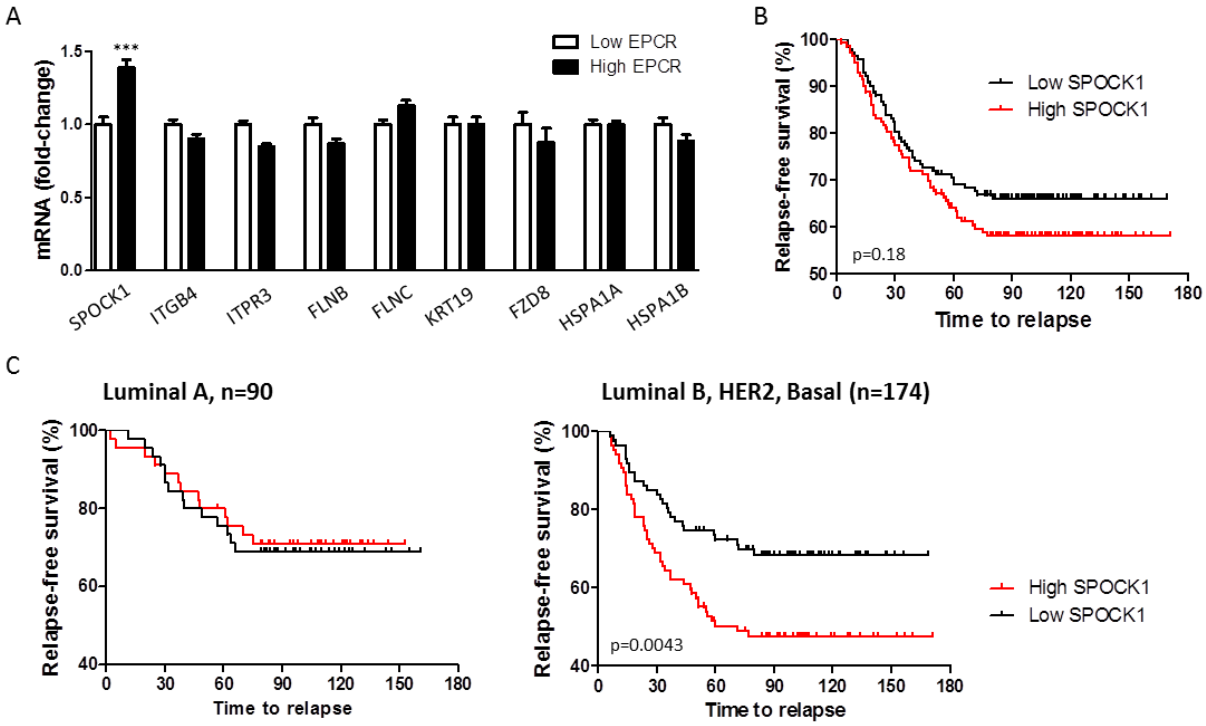

Figure 44. Validation of the genes selected from the microarray analysis, by *in silico* analysis. A. Relative expression levels of the genes indicated in patients with high or low EPCR levels in the GSE2034 cohort. B. Relapse-free survival analysis of the 286 patients based on SPOCK1 expression levels. C. Relapse-free survival analysis in the luminal A subset (left) and in grouped luminal B, HER2, and basal subsets (right).

3. EPCR SILENCING BLOCKS LUNG METASTASIS IN ANV5, A MURINE BREAST CANCER MODEL

Next, we validated the results in a different breast cancer model, using the ANV5 murine breast cancer cell line. ANV5 is a mesenchymal cell line with breast cancer stem cell properties[233,234]. It was obtained from a relapsed tumor, after subcutaneous implantation of epithelial-like cancer cells derived from a MMTV-Neu transgenic mouse (MMC cells) into a non-transgenic mouse[233,234]. We analyzed EPCR expression in MMC and various ANV cell lines by RT-qPCR. We observed that while MMC cells were negative for EPCR, all ANV variants expressed high levels of EPCR (Figure 45A). We decided to select ANV5 cell line for EPCR-inhibition experiments, since it was the variant with less EPCR expression (but still high) and it would be easier to achieve high inhibition levels. We confirmed by flow cytometry that all cells expressed EPCR (Figure 45B). Next, we inhibited EPCR expression by 2 shRNAs targeting murine EPCR and we also transduced ANV5 cells with shControl. Inhibition of EPCR was confirmed by qPCR (Figure 45C) and western blot analysis (Figure 45D). Interestingly, EPCR knockdown did not reduce cell proliferation *in vitro* (Figure 45E).

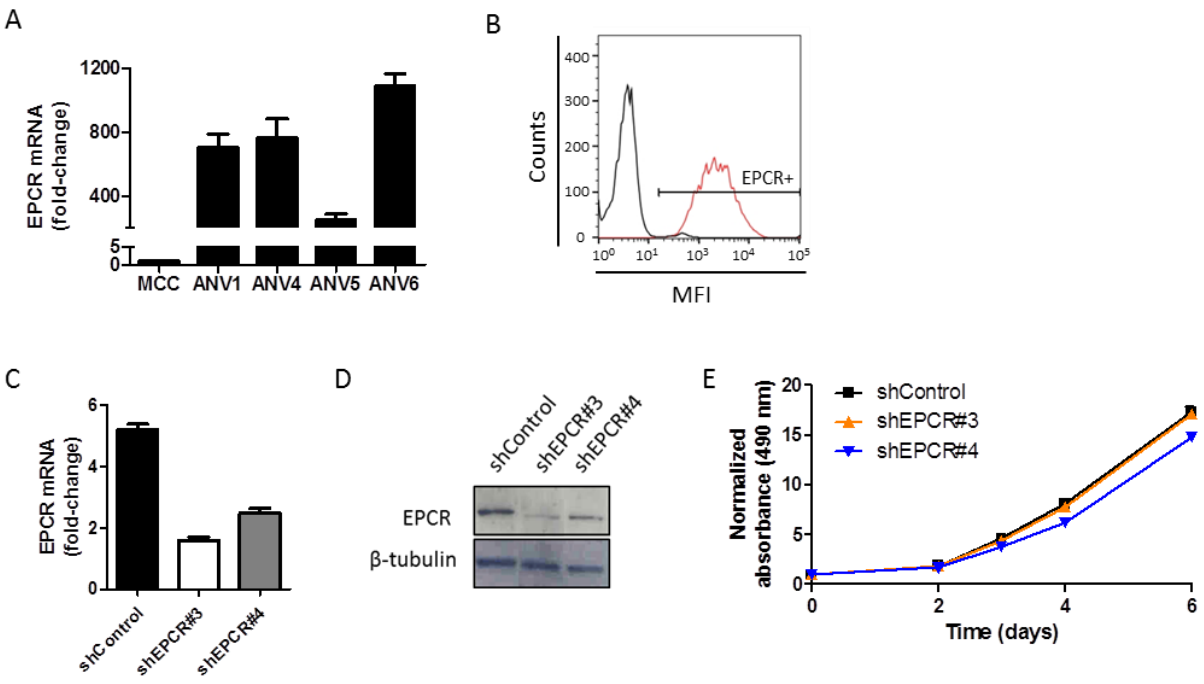

Figure 45. EPCR expression analysis and silencing in ANV5 murine breast cancer cell line. A. EPCR expression, analyzed by qPCR, in MMC and four ANV cell lines. B. EPCR expression in ANV5 cell line, assessed by flow cytometry. The black line represents the isotype control and the red line EPCR expression. MFI: mean fluorescence intensity. C. EPCR expression in ANV5 cells transduced with a random shRNA (shControl) and two shRNAs targeting murine EPCR (shEPCR#3 and shEPCR#4), measured by RT-qPCR. D. EPCR inhibition by shRNAs in ANV5 cell line, detected by western blot. E. MTS *in vitro* proliferation assay of control and EPCR-silenced ANV5 cell lines. Data are mean ± SD of six replicates.

To explore whether EPCR silencing could affect primary tumor growth and development of spontaneous metastases in this model, we carried out an orthotopic experiment. We injected 10,000 shControl, shEPCR#3 and shEPCR#4 ANV5 cells embedded in matrigel into the fourth mammary fat pads of MMTV-Neu mice (n=6 per group). We followed tumor growth by BLI and subsequent evaluation of tumor volume. Tumors were resected when their size reached 500 mm^3 and mice were followed-up for development of metastatic events until day 45 post-injection (Figure 46A). Photon flux quantification at mammary glands revealed that EPCR silencing increased primary tumor growth during the first days of the experiment, although the differences were not statistically significant (Figure 46B). At day 13 post-injection, all mice in shControl and shEPCR#3 groups had developed tumors in both mammary glands, while tumor uptake was 6 out of 12 mammary glands in shEPCR#4 group. At day 15, all mice had palpable tumors in both mammary glands. Tumors from mice injected with shEPCR#3 cells were larger than shControl tumors (p=0.189), while shEPCR#4 tumors were smaller than shControl tumors (p=0.002) (Figure 46C). Consistently, tumors from shEPCR#3 group were resected significantly earlier than shControl tumors (p=0.012), while shEPCR#4 tumors were resected significantly later than shControl tumors (p<0.001) (Figure 46D).

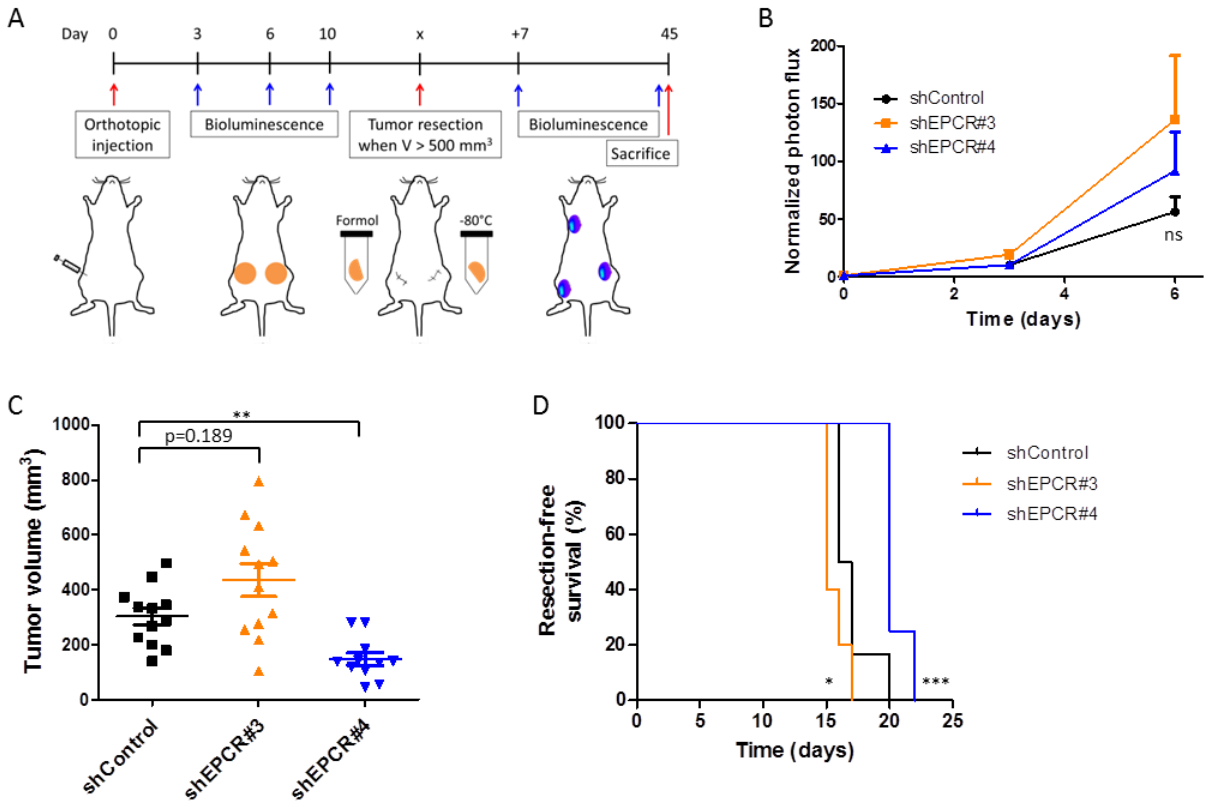

Figure 46. Evaluation of the effects of EPCR silencing in an orthotopic model. A. Outline of the experiment. B. Fold-increase of BL signals in mammary glands assessed until day 6 of the experiment. C. Tumor volume quantification at the end of the experimental period. Each dot represents one tumor. Data are mean ± SEM. D. Resection-free survival analysis of mice.

After tumor resection, we evaluated the development of primary tumor regrowths and metastases by BLI. Almost all tumors relapsed in shControl and shEPCR#3 groups, 11 out of 12 and 6 out of 6, respectively. However, the number of relapsed tumors was significantly lower in shEPCR#4 group (2/8) compared to shControl group (p=0.0092). Of note, three mice from shEPCR#3 group and two mice from shEPCR#4 group died after tumor resection and could not be included in the analysis. We did not observe metastatic events over the course of the experiment, which could not be continued further based on the large size of relapsed tumors.

Finally, we evaluated the prometastatic activity of EPCR in an intratail injection model. For this purpose, we injected 100,000 shControl, shEPCR#3 and shEPCR#4 ANV5 cells resuspended in PBS intravenously through the tail vein of athymic nude mice (n=8 per group) and analyzed lung metastases at the end of the experiment (Figure 47A). Of note, we performed the experiment in athymic nude mice since we observed few metastatic events in a preliminary experiment in MMTV-Neu mice. EPCR knockdown blocked lung metastasis in this model, assessed by BLI (p=0.021 and p=0.004 for shEPCR#3 and shEPCR#4, respectively) (Figures 47B and 47D) and

tumor area quantification in H&E stained lung sections (p=0.077 and p=0.082 for shEPCR#3 and shEPCR#4, respectively) (Figures 47C and 47D).

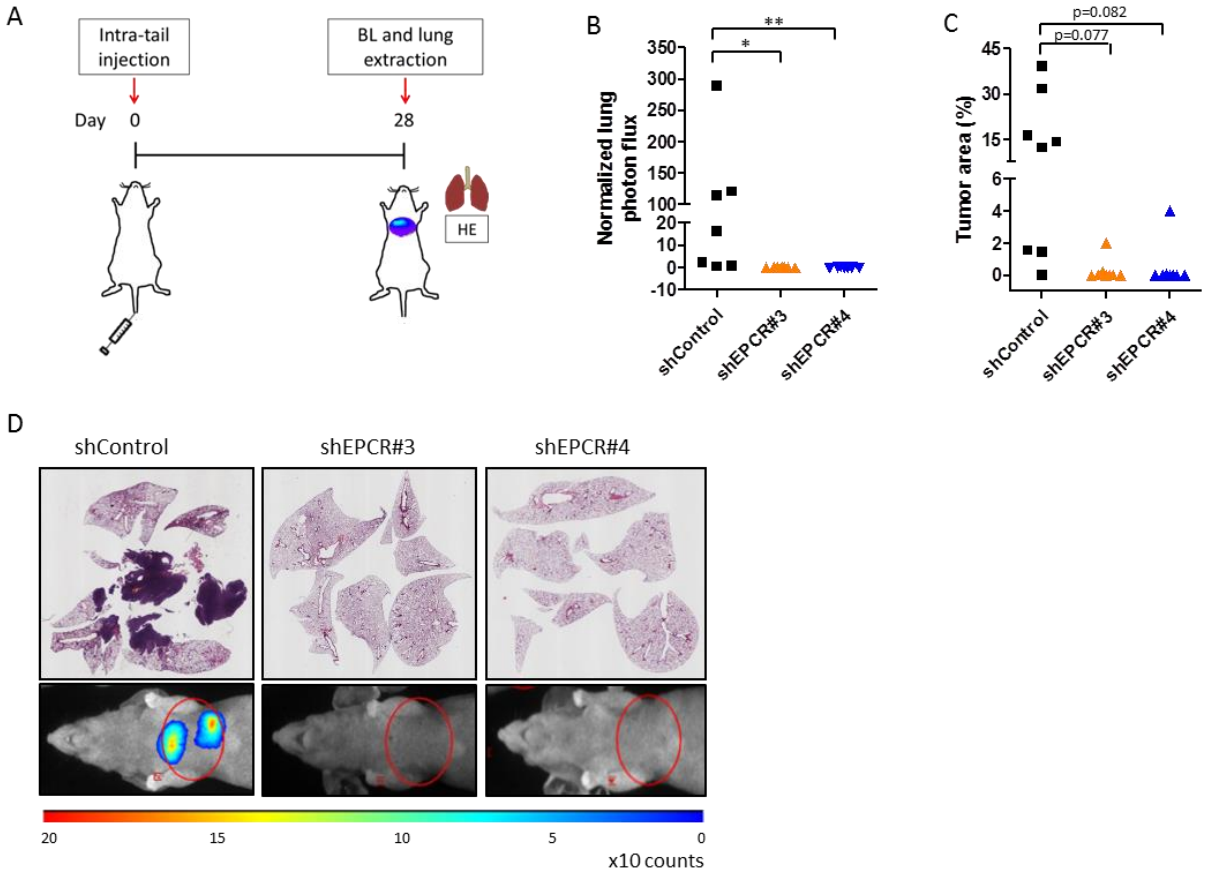

Figure 47. Evaluation of the effects of EPCR silencing (ANV5 cells) in metastasis to the lungs A**.** Outline of the experiment**.** B. Quantification of BL in the lungs, at the end of the experimental period. C. Tumor area quantification in H&E stained lung sections. Each dot represents one mouse. D. Representative images of H&E stainings (top) and BL signals (bottom).

Overall, these results validate the prometastatic activity of EPCR in breast cancer and further indicate that EPCR participates in metastasis to different organs including lung and the skeleton.

V Discussion

In this work, we have identified EPCR as a novel clinically relevant factor in breast cancer. Based on several murine models, we have unveiled the contribution of EPCR to the bone and lung metastatic activities of breast cancer cells. Furthermore, we have also shown that EPCR promotes tumorigenesis in several *in vivo* models. Although further studies are needed to understand the mechanisms underlying EPCR effects, these results suggest that EPCR represents a potential therapeutic target in breast cancer.

1. CLINICAL RELEVANCE OF EPCR

Previously, several prognostic genes and gene-signatures have been described in breast cancer. For instance, MammaPrint® (Agilent), a 70-gene signature, and Oncotype DX (Genomic Health), a 21-gene signature, are prognostic and predictive tools used in clinical practice[24,25]. However, the variability in tumor samples and platforms used to identify prognostic signatures results in almost no overlap across different studies[243,244]. Indeed, EPCR was not present in those transcriptomic analyses associated with poor prognosis. However, the analysis of 286 breast cancer patients revealed that high EPCR expression levels in primary tumors correlate with poor clinical outcome. The predictive potential of EPCR was independent of the molecular subtype, an established prognostic factor, since all different subtypes were well represented in this cohort. GSE2034 includes early stage patients not-receiving chemotherapy, and therefore, we cannot conclude that EPCR levels can also predict clinical outcome in advanced stages of breast cancer and in patients treated with systemic therapy. Future analyses including advanced and treated tumors should address these questions.

An important limitation of the *in silico* analysis derives from the heterogeneity of tumors, which also contain infiltrating non-tumor cells (CAFs, immune cells, endothelial cells, MSCs and adipocytes)[42]. Since EPCR is expressed in endothelial cells[140] and other cell types such as monocytes[155] and neutrophils[157], their contribution to overall EPCR expression levels in the tumor could heavily influence the results. In contrast, immunohistochemical analysis in a panel of tumor biopsies would allow a more detailed quantification of EPCR specifically in tumor cells. Future validation of the results using this approach will also establish a more accurate correlation between EPCR expression and clinical outcome.

2. EPCR AS A PROTUMORIGENIC FACTOR

The use of MDA-MB-231 cells to identify genes involved in tumorigenesis and metastasis is well established in the field of breast cancer research. Therefore, xenograft models using this cell line represent useful tools to explore mechanistic insights related to breast cancer[245].

The protumorigenic activity of EPCR observed in 1833 xenograft models is in agreement with other reports. Schaffner *et al.*[227] showed that PyMT-EPCR$^{Low/Low}$ mice develop small spontaneous mammary tumors as compared to controls. They also revealed that EPCR^{+} mfp-MDA-MB-231

(mammary fat pad-enhanced MDA-MB-231) cells had enhanced tumor-initiating ability compared to $EPCR^-$ cells after orthotopic inoculation into SCID mice. In addition, tumor size was also greater in mice injected with $EPCR^+$ cells compared to mice injected with $EPCR^-$ cells. We did not monitor the emergence of early lesions in our experiment. However, in our orthotopic experiment (Figure 30), 6 tumors remained non-palpable in both shEPCR groups and only 1 tumor in both control groups at day 15 post-injection. Moreover, this tumor had a lower BL signal at day 0. Although these differences were not statistically significant, these results support the role of EPCR in tumor initiation. Nevertheless, differences in tumor size between $EPCR^+$ and $EPCR^-$ tumors became more relevant at later times, indicating that independently of its potential role in tumor-initiation, EPCR could also have a role during tumor progression. Indeed, several tumors in the shEPCR groups remained very small until the end of the experimental period (day 108 post-injection). In contrast, Keshava *et al.*[228] showed that although EPCR overexpression increased initial growth of mfp-MDA-MB-231 cells orthotopically inoculated into nude mice, it resulted in smaller final tumor volumes (day 60 post-injection). Importantly, EPCR staining in tumor sections revealed few EPCR-expressing cells, while the majority of cells were negative for EPCR. It would be interesting to know whether the switch in EPCR role from tumor-promoting to tumor-suppressing was related to the EPCR loss observed. Schaffner *et al.*[227] also showed that tumors derived from inoculation of $EPCR^+$ cells contained both $EPCR^+$ and $EPCR^-$ populations, supporting the view that EPCR could be a cancer stem-cell marker that is only expressed in tumor-initiating cells that give rise to $EPCR^-$ bulk cancer cells. However, this is not a plausible explanation for EPCR loss in the experiment from Keshava at al.[228], which could more probably be related to promoter silencing by *in vivo* methylation of the stably transfected construct. Although we also observed EPCR loss in some tumor areas in control groups, immunohistochemical analysis of EPCR revealed a robust staining. Since flow cytometry data of 1833 cells *in vitro* showed that all cells were positive for EPCR, one possible explanation is that EPCR bound to the membrane could be cleaved by TACE *in vivo*, leading to some regions with EPCR negative staining. Flow cytometry or immunofluorescence analysis of EPCR expression in cells from freshly harvested tumors and cells maintained in culture subsequently could help to discern the mechanisms of EPCR loss *in vivo*.

In contrast, the role of EPCR in tumorigenesis in the ANV5 xenograft model was unclear. ANV5 cells display an aggressive phenotype resulting in accelerated mammary tumor growth, which limits the suitability of this model to unveil differences in primary tumor growth. Although they were originally derived from transgenic mice overexpressing the oncogene Neu, they are characterized by Neu loss[233,234]. However, it is plausible that other oncogenic events could be driving this accelerated tumor growth, and therefore, EPCR signaling could be irrelevant in this context. Importantly, this is a syngenic model, where cancer cells are inoculated into immunocompetent mice. It has been suggested that EPCR could recruit T cells by interacting with

their TCR receptor, which could further eradicate tumor cells[147]. Whether this could occur in our model remains to be addressed.

Overall, clinical data and the results obtained in the different xenograft models support the protumorigenic activity of EPCR in breast cancer.

3. EPCR AS A PROMETASTATIC FACTOR

EPCR silencing resulted in an overt reduction in bone and lung metastases in different xenograft models. Intracardiac and intravenous injection models recapitulate late steps in the metastatic cascade, such as homing, extravasation and colonization of the target organ. However, such models obviate early steps, including invasion and intravasation. In contrast, orthotopic models recapitulate all the steps of the metastatic cascade, and therefore, such models better reflect the course of this process in patients[246].

Since 1833 cells display bone tropism[82], we could evaluate metastasis to bone in xenograft models after intracardiac inoculation of this cell line. Orthotopically inoculated mice also developed spontaneous metastases to diverse skeletal organs. On the other hand, intravenous injection through the tail vein favors the hematogenous spread of cells to the lungs and is a well-established model for the evaluation of lung metastasis[246]. Interestingly, other models could unveil whether the metastatic activity of EPCR extends to other target organs.

The consistent results obtained in both models indicate that EPCR plays an important role in the late steps of the metastatic cascade. After intracardiac injection, EPCR silencing resulted in decreased bone BL signals from day 13 on, and these differences increased over the course of the experiment (Figure 38). In the same line, differences in lung metastasis after intratail injection became relevant at late time points (Figure 47). Furthermore, EPCR silencing reduced bone colonization in an intratibial injection model (Figure 40). These observations strongly suggest that EPCR plays a role in tumor colonization at the target organ (bone and lung).

Of note, BL signals in hindlimbs at day 6 post-injection (intracardiac inoculation, Figure 38) were similar in mice injected with control and EPCR-silenced cells, indicating that EPCR does not affect the survival of cancer cells in secondary outgrowths at early time points. However, in addition to a prominent role during colonization, EPCR may also modulate metastatic tumor re-initiation at the target organ, since the number of tumor nodules in shEPCR mice in both bone and lung metastasis experiments (Figures 38 and 47, respectively) was significantly lower compared to control mice. Thus, we cannot discard the possibility that in addition to tumor growth at secondary sites, re-initiation could also be impared in this setting.

One limitation of the use of shRNAs is the unspecific mRNA inhibition (off-target effects). Since the effects of EPCR silencing are consistent with four different shRNAs (two targeting human EPCR and two targeting murine EPCR), the effects observed are most likely due to specific

EPCR inhibition. Moreover, the clinical correlation between EPCR expression and probability of relapse strongly supports its role in breast cancer progression and metastasis.

Furthermore, the prometastatic activity of EPCR observed in breast cancer was consistent with previous findings in lung cancer, where EPCR silencing or blockade impaired metastasis.

Another limitation of our approach was the partial characterization of the role of EPCR in early steps of metastasis. Future experiments will address this issue using an inducible shRNA construct targeting EPCR silencing at different time points.

In contrast, Schaffner *et al.*[227] did not observe differences in spontaneous lung metastasis between PyMT-EPCR$^{Low/Low}$ and PyMT-WT mice. This could be explained by the simultaneous inhibition of EPCR in both endothelial cells and tumor cells in this genetic model. It has been reported that overexpression or stimulation of EPCR in endothelial cells enhanced barrier stabilization and consequently reduced metastasis of EPCR^{-} B16-F10 melanoma cells[222]. Similarly, the diminished metastatic activity of EPCR^{-} cancer cells could be compensated by the enhanced permeability of EPCR^{-} endothelial barriers in PyMT-EPCR$^{Low/Low}$ mice, resulting in no differences in lung metastasis between PyMT-EPCR$^{Low/Low}$ and PyMT-WT mice.

4. MECHANISMS MEDIATING EPCR EFFECTS

4.1. Role of APC

At the mechanistic level, a previous study from our laboratory revealed that signaling through the APC-EPCR axis in lung cancer cells resulted in the activation of survival signals pERK and pAKT and the induction of an anti-apoptotic gene-signature, leading to an enhanced metastatic activity in these cells. Furthermore, treatment with APC-EPCR-blocking antibodies reduced metastasis of A549 lung cancer cells to bone[217].

In contrast, APC did not affect survival or apoptosis of 1833 cells *in vitro*, although they express both EPCR and PAR1. In addition, EPCR-blocking antibodies could not reduce metastasis of 1833 cells to bone. Although we cannot discard the possibility that the dose and/or therapeutic regimen of the antibodies administered were not the most suitable to achieve maximum EPCR blockade, these results suggest that EPCR promotes metastasis through an APC-independent mechanism in our model. This conclusion is further supported by the recent discovery of new EPCR ligands that bind to the extracellular domain in a different region of the APC-binding site[147]. But how can the same receptor promote metastasis through different mechanisms? Researchers have been able to disrupt the APC-binding ability of EPCR by engineering specific EPCR point-mutations[247,248], but so far, none of these mutations have been described in humans. Interestingly, a 23 bp insertion that abrogates EPCR function[249] and a point-substitution that increases EPCR cleavage[149] have been described in humans. Along the same lines, other unknown mutations that could enhance EPCR affinity for other ligands might also exist. Finally,

high concentrations of other potential ligands in the tumor microenvironment could also explain the APC-independent EPCR-signaling.

Another open question is whether EPCR drives tumorigenesis and metastasis through the same or different cellular and/or molecular mechanisms and therefore, whether anti-EPCR blocking antibodies would also fail to reduce primary tumor growth in the orthotopic model.

Indeed, Schaffner *et al.*[227] revealed that anti-EPCR blocking antibodies (1535) reduced the growth of mfp-MDA-MB-231 cells orthotopically inoculated into SCID mice. Importantly, Schaffner *et al.* employed whole-body antibodies, while we used $F(ab')_2$ fractions of RCR252 antibody. It is well known that antibodies can trigger antibody-dependent, cell mediated-cytotoxicity (ADCC) through the recruitment of NK and T cells[250]. Similarly, their Fc fraction can also activate the complement system, and trigger an innate immune response to induce phagocytosis of antigen-expressing cells[251]. Since we have observed that RCR252 activates the complement system, it is reasonable to speculate that 1535 antibody could also trigger its activation, leading to tumor growth reduction independently of APC-EPCR blockade in tumor cells.

4.2. Role of the microenvironment

An interesting point in our studies was that EPCR inhibition did not alter growth kinetics or apoptosis of breast cancer cells *in vitro*. These results suggest that EPCR could exert its function by non-cell autonomous mechanisms, by modulating tumor-stroma interactions with other cell types or the ECM. Along similar lines, EPCR signaling could become relevant in some specific microenvironmental conditions, such as hypoxia and/or nutrient-deprivation, or during the concomitant activation of other signaling pathways *in vivo*.

4.3. Role of heterotypic cellular interactions

EPCR has been found to be involved in the recruitment of leukocytes to damaged organs[241,242]. However, analysis of immune cell subpopulations in mammary tumors derived from orthotopically injected 1833 cells did not show relevant differences between control and EPCR-silenced tumors. Similarly, *in vitro* co-cultures of 1833 cancer cells and bone stromal cells (ST2) or fibroblasts (WI38) did not reveal a role of EPCR in the modulation of these heterotypic interactions.

4.4. Role of other cellular functions

Transcriptomic analysis of size-matched control and EPCR-silenced tumors revealed several differentially enriched cell functions, such as cell death, proliferation, senescence, EMT, angiogenesis, migration and invasion, and lipid metabolism. However, immunohistochemical analysis in those tumors did not show differences in cell death, proliferation and angiogenesis. In addition, those differences did not become relevant when the analysis was performed in tumors with prominent size differences. These results suggest that EPCR could play a more relevant role

at earlier time points, for instance, during the maintenance of micrometastases and subsequent tumor growth. Similarly, *in vitro* migration and invasion experiments did not reveal differences between control and shEPCR cells.

4.5. Role of lipid metabolism

Altered metabolism is one of the hallmarks of cancer, and recently new roles played by lipids in tumor growth and survival have emerged[252]. For example, hypoxia and oncogenic signals stimulate uptake and utilization of lysophospholipids to supply an intracellular lipid pool for growth. Fatty acid oxidation has been shown to be a preferential pathway for fuel supply in some cancer cells and interestingly, it was found to be responsible in part for the tumor-initiating potential of cancer cells remaining after treatment with kinase inhibitors. Moreover, in ovarian cancer, adipocyte transfer of fatty acids has been shown to activate AMPK and fatty acid oxidation in cancer cells, enhancing cell proliferation[252].

Interestingly, several metabolism-related pathways were altered in EPCR-silenced tumors. But how could EPCR signaling and lipid metabolism be related? EPCR is localized in lipid rafts on the membranes and it also contains a hydrophobic groove that is occupied by a lipid, mostly phosphatidylcholine[144]. EPCR could be involved in the stabilization and/or signaling of these lipids. However, so far, those functions are poorly understood.

4.6. Molecular mechanisms

At the molecular level, several genes that have been related to tumor progression were downregulated in EPCR-silenced mammary tumors.

Signaling components differentially expressed with EPCR include FZD8, HSPA1A and 1B and ITPR3. FZD8 belongs to the Wnt signaling pathway, which has been widely related to cancer progression[253]. HSPA1A and HSPA1B encode proteins of the heat shock 70 kDa protein family, which are involved in the stabilization and folding of proteins and have been related to increased growth of breast and other tumors[254,255]. ITPR3 is a receptor for inositol 1,4,5-trisphosphate, a second messenger that mediates the release of intracellular calcium and is involved in metabolism. It was reported to stimulate breast cancer cell proliferation[256].

Several cytoskeletal proteins were also identified, such as keratin 19 (KRT19) and filamins (FLN). KRT19 is a member of the keratin family, intermediate filament proteins responsible for the structural integrity of epithelial cells and has been associated with poor prognosis of breast cancer patients[257] and tumor initiation[258]. FLNs are actin-binding proteins that link actin filaments to membrane glycoproteins and have been reported to play opposing roles in several types of cancer[259-261].

Importantly, the ECM-related molecules SPOCK1 and ITGB4 were downregulated in EPCR-silenced tumors. SPOCK1 is a secreted proteoglycan that contains chondroitin- and heparan-sulfate chains and was shown to increase EMT and metastasis[262-264]. ITGB4 mediates ECM-cell adhesion and is involved in both mammary gland development and breast cancer progression[52-54].

The cytoskeletal and ECM-related proteins are involved in the structural organization of cells[265]. Therefore, EPCR signaling could be relevant for the maintenance or remodelling of the tumor architecture, which could further support tumor growth. Indeed, EPCR has been recently shown to be necessary for cell organization and growth of mammary epithelial cells in 3D cultures, a finding that could partially explain the absence of effects after EPCR inhibition in cells cultured on plastic plates. Future experiments in 3D *in vitro* models[266,267] could unveil differences in cell proliferation and/or apoptosis between control and EPCR-silenced cells.

Interestingly, patients with high EPCR expression in the GSE2034 cohort also had significantly higher SPOCK1 expression levels. Moreover, high levels of SPOCK1 and EPCR were correlated with significantly shorter relapse-free survival times in the same subsets of patients, indicating that EPCR effects could be mediated at least in part by SPOCK1. Moreover, SPOCK1 downregulation was already observed in cells cultured *in vitro*, suggesting that EPCR silencing could be responsible for its downregulation.

5. EPCR AS A THERAPEUTIC TARGET

The significant impairment of tumorigenesis and metastasis by EPCR silencing suggests that EPCR could be a therapeutic target in breast cancer. However, several points need to be taken into consideration:

1. Cancer is frequently accompanied by venous thromboembolism and inhibiting an anticoagulant factor such as EPCR would raise the complications derived from an altered coagulation system. On the other hand, our results suggest that at least in our model, EPCR-driven tumorigenesis and metastasis are APC-independent and therefore, it would be possible to target EPCR on tumor cells without affecting the anticoagulant function of EPCR expressed on endothelial cells.

2. It would be necessary to identify the region of EPCR important for its protumorigenic and prometastatic activity, in order to design molecules that could target EPCR while preserving APC/EPCR interaction in normal epithelium.

3. Although the relevant differences in tumor volume at advanced experimental time points suggest that EPCR is relevant for tumor progression, whether EPCR would be a relevant driver in patient tumors at the time of diagnosis remains to be addressed. It would be interesting to explore whether induction of EPCR silencing in already established tumors could reduce tumor growth or even induce tumor regression.

In summary, EPCR is a clinically relevant factor in breast cancer, which promotes primary tumor growth and metastatic growth in target organs. Although further mechanistic exploration is needed, EPCR could modulate tumor cell-ECM interactions to enhance tumor progression, in part by upregulating SPOCK1. However, how EPCR signaling is activated in breast cancer cells and how EPCR signaling increases SPOCK1 expression remain unknown. Further characterization of the protumorigenic and prometastatic activity of EPCR could substantiate the role of EPCR as a potential therapeutic target in breast cancer.

VI Conclusions

1. EPCR expression levels are associated with shorter relapse-free survival times in breast cancer patients. EPCR is predictive of clinical outcome in luminal B, HER2+ and basal-like subsets, but not in luminal A subset.

2. *In vitro* cell proliferation rate and resistance to apoptosis of 1833 breast cancer cells are not affected by APC stimulation, blockade of APC-EPCR interaction or EPCR silencing.

3. EPCR silencing impairs primary tumor growth in xenograft models of tumorigenesis, whereas markers of cell growth, apoptosis and angiogenesis are unaffected in tumors. EPCR effects on tumor progression are independent of heterotypic interactions with stromal components, including fibroblasts and immune cells.

4. EPCR silencing reduces metastatic activity to bone and lung in several xenograft models, most likely by an APC-independent mechanism.

5. The most robustly downregulated gene in EPCR-silenced cells and tumors was SPOCK1, related to cytoskeletal organization and cancer cell-extracellular matrix interactions.

6. SPOCK1 expression levels were associated with high EPCR expression in breast cancer patients and correlated with shorter-relapse free survival times in luminal B, HER2+ and basal-like subsets.

VII References

1 Torre, L. A. *et al.* Global cancer statistics, 2012. *CA: a cancer journal for clinicians* 65, 87-108, doi:10.3322/caac.21262 [doi] (2015).

2 Ferlay, J. *et al.* Reprint of: Cancer incidence and mortality patterns in Europe: Estimates for 40 countries in 2012. *European journal of cancer (Oxford, England : 1990)* 51, 1201-1202, doi:10.1016/j.ejca.2015.05.004 [doi] (2015).

3 Siegel, R. L., Miller, K. D. & Jemal, A. Cancer statistics, 2015. *CA: a cancer journal for clinicians* 65, 5-29, doi:10.3322/caac.21254 [doi] (2015).

4 Weigelt, B. *et al.* Refinement of breast cancer classification by molecular characterization of histological special types. *The Journal of pathology* 216, 141-150, doi:10.1002/path.2407 [doi] (2008).

5 Weigelt, B., Geyer, F. C. & Reis-Filho, J. S. Histological types of breast cancer: how special are they? *Molecular oncology* 4, 192-208, doi:10.1016/j.molonc.2010.04.004 [doi] (2010).

6 Weigelt, B. & Reis Filho, J. Histological and molecular types of breast cancer: is there a unifying taxonomy? *Nature Reviews Clinical Oncology* 6, 718-730 (2009).

7 Sinn, H. P. & Kreipe, H. A Brief Overview of the WHO Classification of Breast Tumors, 4th Edition, Focusing on Issues and Updates from the 3rd Edition. *Breast care (Basel, Switzerland)* 8, 149-154, doi:10.1159/000350774 [doi] (2013).

8 Weigelt, B., Peterse, J. & van 't Veer, L. J. Breast cancer metastasis: markers and models. *Nature Reviews Cancer* 5, 591-602 (2005).

9 Dalton, L. W., Page, D. L. & Dupont, W. D. Histologic grading of breast carcinoma. A reproducibility study. *Cancer* 73, 2765-2770 (1994).

10 Elston, C. W. & Ellis, I. O. Pathological prognostic factors in breast cancer. I. The value of histological grade in breast cancer: experience from a large study with long-term follow-up. *Histopathology* 41, 154-161, doi:1489_2 [pii] (2002).

11 Orucevic, A. *et al.* Is the TNM staging system for breast cancer still relevant in the era of biomarkers and emerging personalized medicine for breast cancer - an institution's 10-year experience. *The breast journal* 21, 147-154, doi:10.1111/tbj.12367 [doi] (2015).

12 Rivenbark, A. G., O'Connor, S. M. & Coleman, W. B. Molecular and cellular heterogeneity in breast cancer: challenges for personalized medicine. *The American journal of pathology* 183, 1113-1124, doi:10.1016/j.ajpath.2013.08.002 [doi] (2013).

13 Bertos, N. R. & Park, M. Breast cancer - one term, many entities? *The Journal of clinical investigation* 121, 3789-3796, doi:10.1172/JCI57100 [doi] (2011).

14 Perou, C. M. *et al.* Molecular portraits of human breast tumours. *Nature* 406, 747-752, doi:10.1038/35021093 [doi] (2000).

15 Sorlie, T. *et al.* Gene expression patterns of breast carcinomas distinguish tumor subclasses with clinical implications. *Proceedings of the National Academy of Sciences of the United States of America* 98, 10869-10874, doi:10.1073/pnas.191367098 [doi] (2001).

16 Sorlie, T. *et al.* Repeated observation of breast tumor subtypes in independent gene expression data sets. *Proceedings of the National Academy of Sciences of the United States of America* 100, 8418-8423, doi:10.1073/pnas.0932692100 [doi] (2003).

17 Vuong, D., Simpson, P. T., Green, B., Cummings, M. C. & Lakhani, S. R. Molecular classification of breast cancer. *Virchows Archiv : an international journal of pathology* 465, 1-14, doi:10.1007/s00428-014-1593-7 [doi] (2014).

18 Prat, A. *et al.* Phenotypic and molecular characterization of the claudin-low intrinsic subtype of breast cancer. *Breast cancer research : BCR* 12, R68, doi:10.1186/bcr2635 [doi] (2010).

19 Farmer, P. *et al.* Identification of molecular apocrine breast tumours by microarray analysis. *Oncogene* 24, 4660-4671, doi:1208561 [pii] (2005).

20 Hu, Z. *et al.* The molecular portraits of breast tumors are conserved across microarray platforms. *BMC genomics* 7, 96, doi:1471-2164-7-96 [pii] (2006).

21 Parker, J. S. *et al.* Supervised risk predictor of breast cancer based on intrinsic subtypes. *Journal of clinical oncology : official journal of the American Society of Clinical Oncology* 27, 1160-1167, doi:10.1200/JCO.2008.18.1370 [doi] (2009).

22 Schnitt, S. J. Classification and prognosis of invasive breast cancer: from morphology to molecular taxonomy. *Modern pathology : an official journal of the United States and Canadian Academy of Pathology, Inc* 23 Suppl 2, S60-64, doi:10.1038/modpathol.2010.33 [doi] (2010).

23 Viale, G. The current state of breast cancer classification. *Annals of Oncology : Official Journal of the European Society for Medical Oncology / ESMO* 23 Suppl 10, x207-210, doi:mds326 [pii] (2012).

24 Prat, A., Ellis, M. J. & Perou, C. M. Practical implications of gene-expression-based assays for breast oncologists. *Nature reviews.Clinical oncology* 9, 48-57, doi:10.1038/nrclinonc.2011.178 [doi] (2011).

25 Yersal, O. & Barutca, S. Biological subtypes of breast cancer: Prognostic and therapeutic implications. *World journal of clinical oncology* 5, 412-424, doi:10.5306/wjco.v5.i3.412 [doi] (2014).

26 Guedj, M. *et al.* A refined molecular taxonomy of breast cancer. *Oncogene* 31, 1196-1206, doi:10.1038/onc.2011.301 [doi] (2012).

27 Stratton, M. R., Campbell, P. J. & Futreal, P. A. The cancer genome. *Nature* 458, 719-724, doi:10.1038/nature07943 [doi] (2009).

28 Fernandez-Ramires, R. *et al.* Transcriptional characteristics of familial non-BRCA1/BRCA2 breast tumors. *International journal of cancer.Journal international du cancer* 128, 2635-2644, doi:10.1002/ijc.25603 [doi] (2011).

29 Economopoulou, P., Dimitriadis, G. & Psyrri, A. Beyond BRCA: new hereditary breast cancer susceptibility genes. *Cancer treatment reviews* 41, 1-8, doi:10.1016/j.ctrv.2014.10.008 [doi] (2015).

30 Hanahan, D. & Weinberg, R. A. Hallmarks of cancer: the next generation. *Cell* 144, 646-674, doi:10.1016/j.cell.2011.02.013 [doi] (2011).

31 Polyak, K. & Weinberg, R. A. Transitions between epithelial and mesenchymal states: acquisition of malignant and stem cell traits. *Nature reviews.Cancer* 9, 265-273, doi:10.1038/nrc2620 [doi] (2009).

32 Shah, S. P. *et al.* The clonal and mutational evolution spectrum of primary triple-negative breast cancers. *Nature* 486, 395-399, doi:10.1038/nature10933 [doi] (2012).

33 Shah, S. P. *et al.* Mutational evolution in a lobular breast tumour profiled at single nucleotide resolution. *Nature* 461, 809-813, doi:10.1038/nature08489 [doi] (2009).

34 Banerji, S. *et al.* Sequence analysis of mutations and translocations across breast cancer subtypes. *Nature* 486, 405-409, doi:10.1038/nature11154 [doi] (2012).

35 Ellis, M. J. *et al.* Whole-genome analysis informs breast cancer response to aromatase inhibition. *Nature* 486, 353-360, doi:10.1038/nature11143 [doi] (2012).

36 Stephens, P. J. *et al.* The landscape of cancer genes and mutational processes in breast cancer. *Nature* 486, 400-404, doi:10.1038/nature11017 [doi] (2012).

37 Cancer Genome Atlas, N. Comprehensive molecular portraits of human breast tumours. *Nature* 490, 61-70, doi:10.1038/nature11412 [doi] (2012).

38 Curtis, C. *et al.* The genomic and transcriptomic architecture of 2,000 breast tumours reveals novel subgroups. *Nature* 486, 346-352, doi:10.1038/nature10983 [doi] (2012).

39 Russnes, H. G., Navin, N., Hicks, J. & Borresen-Dale, A. L. Insight into the heterogeneity of breast cancer through next-generation sequencing. *The Journal of clinical investigation* 121, 3810-3818, doi:10.1172/JCI57088 [doi] (2011).

40 Dawson, S. J., Rueda, O. M., Aparicio, S. & Caldas, C. A new genome-driven integrated classification of breast cancer and its implications. *The EMBO journal* 32, 617-628, doi:10.1038/emboj.2013.19 [doi] (2013).

41 Polyak, K. & Metzger Filho, O. SnapShot: breast cancer. *Cancer cell* 22, 562-562.e561, doi:10.1016/j.ccr.2012.06.021 [doi] (2012).

42 Egeblad, M., Nakasone, E. S. & Werb, Z. Tumors as organs: complex tissues that interface with the entire organism. *Developmental cell* 18, 884-901, doi:10.1016/j.devcel.2010.05.012 [doi] (2010).

43 Korkaya, H., Liu, S. & Wicha, M. S. Breast cancer stem cells, cytokine networks, and the tumor microenvironment. *The Journal of clinical investigation* 121, 3804-3809, doi:10.1172/JCI57099 [doi] (2011).

44 Hanahan, D. & Coussens, L. M. Accessories to the crime: functions of cells recruited to the tumor microenvironment. *Cancer cell* 21, 309-322, doi:10.1016/j.ccr.2012.02.022 [doi] (2012).

45 Kees, T. & Egeblad, M. Innate immune cells in breast cancer--from villains to heroes? *Journal of mammary gland biology and neoplasia* 16, 189-203, doi:10.1007/s10911-011-9224-2 [doi] (2011).

46 Quail, D. F. & Joyce, J. A. Microenvironmental regulation of tumor progression and metastasis. *Nature medicine* 19, 1423-1437, doi:10.1038/nm.3394 [doi] (2013).

47 Pyonteck, S. M. *et al.* CSF-1R inhibition alters macrophage polarization and blocks glioma progression. *Nature medicine* 19, 1264-1272, doi:10.1038/nm.3337 [doi] (2013).

48 McAllister, S. S. & Weinberg, R. A. The tumour-induced systemic environment as a critical regulator of cancer progression and metastasis. *Nature cell biology* 16, 717-727, doi:10.1038/ncb3015 [doi] (2014).

49 Erler, J. T. & Weaver, V. M. Three-dimensional context regulation of metastasis. *Clinical & experimental metastasis* 26, 35-49, doi:10.1007/s10585-008-9209-8 [doi] (2009).

50 Oskarsson, T. & Massague, J. Extracellular matrix players in metastatic niches. *The EMBO journal* 31, 254-256, doi:10.1038/emboj.2011.469 [doi] (2012).

51 Lu, P., Weaver, V. M. & Werb, Z. The extracellular matrix: a dynamic niche in cancer progression. *The Journal of cell biology* 196, 395-406, doi:10.1083/jcb.201102147 [doi] (2012).

52 Weaver, V. M. *et al.* Reversion of the malignant phenotype of human breast cells in three-dimensional culture and in vivo by integrin blocking antibodies. *The Journal of cell biology* 137, 231-245 (1997).

53 Weaver, V. M. *et al.* Beta4 Integrin-Dependent Formation of Polarized Three-Dimensional Architecture Confers Resistance to Apoptosis in Normal and Malignant Mammary Epithelium. *Cancer cell* 2, 205-216, doi:S1535610802001253 [pii] (2002).

54 Nistico, P., Di Modugno, F., Spada, S. & Bissell, M. J. Beta1 and Beta4 Integrins: from Breast Development to Clinical Practice. *Breast cancer research : BCR* 16, 459 (2014).

55 Bhowmick, N. A., Neilson, E. G. & Moses, H. L. Stromal fibroblasts in cancer initiation and progression. *Nature* 432, 332-337, doi:nature03096 [pii] (2004).

56 Orimo, A. *et al.* Stromal fibroblasts present in invasive human breast carcinomas promote tumor growth and angiogenesis through elevated SDF-1/CXCL12 secretion. *Cell* 121, 335-348, doi:S0092-8674(05)00237-0 [pii] (2005).

57 Kalluri, R. & Zeisberg, M. Fibroblasts in cancer. *Nature reviews.Cancer* 6, 392-401, doi:nrc1877 [pii] (2006).

58 Place, A. E., Jin Huh, S. & Polyak, K. The microenvironment in breast cancer progression: biology and implications for treatment. *Breast cancer research : BCR* 13, 227, doi:10.1186/bcr2912 [doi] (2011).

59 Dirat, B. *et al.* Cancer-associated adipocytes exhibit an activated phenotype and contribute to breast cancer invasion. *Cancer research* 71, 2455-2465, doi:10.1158/0008-5472.CAN-10-3323 [doi] (2011).

60 Dirat, B., Bochet, L., Escourrou, G., Valet, P. & Muller, C. Unraveling the obesity and breast cancer links: a role for cancer-associated adipocytes? *Endocrine development* 19, 45-52, doi:10.1159/000316896 [doi] (2010).

61 Butler, J. M. *et al.* Endothelial cells are essential for the self-renewal and repopulation of Notch-dependent hematopoietic stem cells. *Cell stem cell* 6, 251-264, doi:10.1016/j.stem.2010.02.001 [doi] (2010).

62 Song, S., Ewald, A. J., Stallcup, W., Werb, Z. & Bergers, G. PDGFRbeta+ perivascular progenitor cells in tumours regulate pericyte differentiation and vascular survival. *Nature cell biology* 7, 870-879, doi:ncb1288 [pii] (2005).

63 Kitamura, T., Qian, B. Z. & Pollard, J. W. Immune cell promotion of metastasis. *Nature reviews.Immunology* 15, 73-86, doi:10.1038/nri3789 [doi] (2015).

64 Noy, R. & Pollard, J. W. Tumor-associated macrophages: from mechanisms to therapy. *Immunity* 41, 49-61, doi:10.1016/j.immuni.2014.06.010 [doi] (2014).

65 Lin, E. Y. *et al.* Vascular endothelial growth factor restores delayed tumor progression in tumors depleted of macrophages. *Molecular oncology* 1, 288-302, doi:10.1016/j.molonc.2007.10.003 [doi] (2007).

66 Galdiero, M. R. *et al.* Tumor associated macrophages and neutrophils in cancer. *Immunobiology* 218, 1402-1410, doi:10.1016/j.imbio.2013.06.003 [doi] (2013).

67 De Palma, M. & Naldini, L. Tie2-expressing monocytes (TEMs): novel targets and vehicles of anticancer therapy? *Biochimica et biophysica acta* 1796, 5-10, doi:10.1016/j.bbcan.2009.04.001 [doi] (2009).

68 Jaillon, S. *et al.* Neutrophils in innate and adaptive immunity. *Seminars in immunopathology* 35, 377-394, doi:10.1007/s00281-013-0374-8 [doi] (2013).

69 Nozawa, H., Chiu, C. & Hanahan, D. Infiltrating neutrophils mediate the initial angiogenic switch in a mouse model of multistage carcinogenesis. *Proceedings of the National Academy of Sciences of the United States of America* 103, 12493-12498, doi:0601807103 [pii] (2006).

70 Yang, L. *et al.* Expansion of myeloid immune suppressor Gr+CD11b+ cells in tumor-bearing host directly promotes tumor angiogenesis. *Cancer cell* 6, 409-421, doi:S1535610804002703 [pii] (2004).

71 Murdoch, C., Muthana, M., Coffelt, S. B. & Lewis, C. E. The role of myeloid cells in the promotion of tumour angiogenesis. *Nature reviews.Cancer* 8, 618-631, doi:10.1038/nrc2444 [doi] (2008).

72 Joyce, J. A. & Pollard, J. W. Microenvironmental regulation of metastasis. *Nature reviews.Cancer* 9, 239-252, doi:10.1038/nrc2618 [doi] (2009).

73 Mayordomo, J. I. *et al.* Bone marrow-derived dendritic cells pulsed with synthetic tumour peptides elicit protective and therapeutic antitumour immunity. *Nature medicine* 1, 1297-1302 (1995).

74 Coussens, L. M. *et al.* Inflammatory mast cells up-regulate angiogenesis during squamous epithelial carcinogenesis. *Genes & development* 13, 1382-1397 (1999).

75 Soucek, L. *et al.* Mast cells are required for angiogenesis and macroscopic expansion of Myc-induced pancreatic islet tumors. *Nature medicine* 13, 1211-1218, doi:nm1649 [pii] (2007).

76 Sabrkhany, S., Griffioen, A. W. & Oude Egbrink, M. G. The role of blood platelets in tumor angiogenesis. *Biochimica et biophysica acta* 1815, 189-196, doi:10.1016/j.bbcan.2010.12.001 [doi] (2011).

77 Schmielau, J. & Finn, O. J. Activated granulocytes and granulocyte-derived hydrogen peroxide are the underlying mechanism of suppression of t-cell function in advanced cancer patients. *Cancer research* 61, 4756-4760 (2001).

78 Chaffer, C. & Weinberg, R. A perspective on cancer cell metastasis. *Science* 331, 1559-1564 (2011).

79 Gupta, G. P. & Massague, J. Cancer metastasis: building a framework. *Cell* 127, 679-695, doi:S0092-8674(06)01414-0 [pii] (2006).

80 Nguyen, D. X. & Massague, J. Genetic determinants of cancer metastasis. *Nature reviews.Genetics* 8, 341-352, doi:nrg2101 [pii] (2007).

81 Chiang, A. C. & Massague, J. Molecular basis of metastasis. *The New England journal of medicine* 359, 2814-2823, doi:10.1056/NEJMra0805239 [doi] (2008).

82 Kang, Y. *et al.* A multigenic program mediating breast cancer metastasis to bone. *Cancer Cell* 3, 537-549 (2003).

83 Gupta, G. P. *et al.* Identifying site-specific metastasis genes and functions. *Cold Spring Harbor symposia on quantitative biology* 70, 149-158, doi:10.1101/sqb.2005.70.018 [doi] (2005).

84 Minn, A. J. *et al.* Genes that mediate breast cancer metastasis to lung. *Nature* 436, 518-524, doi:nature03799 [pii] (2005).

85 Bos, P. D. *et al.* Genes that mediate breast cancer metastasis to the brain. *Nature* 459, 1005-1009, doi:10.1038/nature08021 [doi] (2009).

86 Vanharanta, S. & Massague, J. Origins of metastatic traits. *Cancer cell* 24, 410-421, doi:10.1016/j.ccr.2013.09.007 [doi] (2013).

87 Cheung, K. J. & Ewald, A. J. Illuminating breast cancer invasion: diverse roles for cell-cell interactions. *Current opinion in cell biology* 30, 99-111, doi:10.1016/j.ceb.2014.07.003 [doi] (2014).

88 Kalluri, R. & Weinberg, R. A. The basics of epithelial-mesenchymal transition. *The Journal of clinical investigation* 119, 1420-1428, doi:10.1172/JCI39104 [doi] (2009).

89 Thiery, J. P., Acloque, H., Huang, R. Y. & Nieto, M. A. Epithelial-mesenchymal transitions in development and disease. *Cell* 139, 871-890, doi:10.1016/j.cell.2009.11.007 [doi] (2009).

90 Xue, B., Krishnamurthy, K., Allred, D. C. & Muthuswamy, S. K. Loss of Par3 promotes breast cancer metastasis by compromising cell-cell cohesion. *Nature cell biology* 15, 189-200, doi:10.1038/ncb2663 [doi] (2013).

91 Mego, M., Mani, S. A. & Cristofanilli, M. Molecular mechanisms of metastasis in breast cancer--clinical applications. *Nature reviews.Clinical oncology* 7, 693-701, doi:10.1038/nrclinonc.2010.171 [doi] (2010).

92 Barker, H. E. *et al.* LOXL2-mediated matrix remodeling in metastasis and mammary gland involution. *Cancer research* 71, 1561-1572, doi:10.1158/0008-5472.CAN-10-2868 [doi] (2011).

93 Guo, W. & Giancotti, F. G. Integrin signalling during tumour progression. *Nature reviews.Molecular cell biology* 5, 816-826, doi:10.1038/nrm1490 [doi] (2004).

94 Orgaz, J. L., Herraiz, C. & Sanz-Moreno, V. Rho GTPases modulate malignant transformation of tumor cells. *Small GTPases* 5, e29019, doi:10.4161/sgtp.29019 [doi] (2014).

95 Liao, X. H. *et al.* MRTF-A and STAT3 synergistically promote breast cancer cell migration. *Cellular signalling* 26, 2370-2380, doi:10.1016/j.cellsig.2014.07.023 [doi] (2014).

96 Wicki, A. *et al.* Tumor invasion in the absence of epithelial-mesenchymal transition: podoplanin-mediated remodeling of the actin cytoskeleton. *Cancer cell* 9, 261-272, doi:S1535-6108(06)00086-9 [pii] (2006).

97 van Roosmalen, W. *et al.* Tumor cell migration screen identifies SRPK1 as breast cancer metastasis determinant. *The Journal of clinical investigation* 125, 1648-1664, doi:10.1172/JCI74440 [doi] (2015).

98 Dong, H., Claffey, K. P., Brocke, S. & Epstein, P. M. Inhibition of breast cancer cell migration by activation of cAMP signaling. *Breast cancer research and treatment* 152, 17-28, doi:10.1007/s10549-015-3445-9 [doi] (2015).

99 Valastyan, S. & Weinberg, R. A. Tumor metastasis: molecular insights and evolving paradigms. *Cell* 147, 275-292, doi:10.1016/j.cell.2011.09.024 [doi] (2011).

100 Reymond, N., d'Agua, B. B. & Ridley, A. J. Crossing the endothelial barrier during metastasis. *Nature reviews.Cancer* 13, 858-870, doi:10.1038/nrc3628 [doi] (2013).

101 Gupta, G. P. *et al.* Mediators of vascular remodelling co-opted for sequential steps in lung metastasis. *Nature* 446, 765-770, doi:nature05760 [pii] (2007).

102 Giannelli, G., Falk-Marzillier, J., Schiraldi, O., Stetler-Stevenson, W. G. & Quaranta, V. Induction of cell migration by matrix metalloprotease-2 cleavage of laminin-5. *Science (New York, N.Y.)* 277, 225-228 (1997).

103 Pirila, E. *et al.* Gelatinase A (MMP-2), collagenase-2 (MMP-8), and laminin-5 gamma2-chain expression in murine inflammatory bowel disease (ulcerative colitis). *Digestive diseases and sciences* 48, 93-98 (2003).

104 Yang, J. M. *et al.* Extracellular matrix metalloproteinase inducer (CD147) confers resistance of breast cancer cells to Anoikis through inhibition of Bim. *The Journal of biological chemistry* 281, 9719-9727, doi:M508421200 [pii] (2006).

105 Uehara, N., Matsuoka, Y. & Tsubura, A. Mesothelin promotes anchorage-independent growth and prevents anoikis via extracellular signal-regulated kinase signaling pathway in human breast cancer cells. *Molecular cancer research : MCR* 6, 186-193, doi:10.1158/1541-7786.MCR-07-0254 [doi] (2008).

106 Weigel, K. J. *et al.* CAF-secreted IGFBPs regulate breast cancer cell anoikis. *Molecular cancer research : MCR* 12, 855-866, doi:10.1158/1541-7786.MCR-14-0090 [doi] (2014).

107 Gay, L. J. & Felding-Habermann, B. Contribution of platelets to tumour metastasis. *Nature reviews.Cancer* 11, 123-134, doi:10.1038/nrc3004 [doi] (2011).

108 Balkwill, F. R. The chemokine system and cancer. *The Journal of pathology* 226, 148-157, doi:10.1002/path.3029 [doi] (2012).

109 Smith, M. C. *et al.* CXCR4 regulates growth of both primary and metastatic breast cancer. *Cancer research* 64, 8604-8612, doi:64/23/8604 [pii] (2004).

110 Schumacher, D., Strilic, B., Sivaraj, K. K., Wettschureck, N. & Offermanns, S. Platelet-derived nucleotides promote tumor-cell transendothelial migration and metastasis via P2Y2 receptor. *Cancer cell* 24, 130-137, doi:10.1016/j.ccr.2013.05.008 [doi] (2013).

111 Uchide, K. *et al.* Cancer cells cause vascular endothelial cell (vEC) retraction via 12(S)HETE secretion; the possible role of cancer cell derived microparticle. *Annals of surgical oncology* 14, 862-868, doi:10.1245/s10434-006-9225-3 [doi] (2007).

112 Padua, D. *et al.* TGFbeta primes breast tumors for lung metastasis seeding through angiopoietin-like 4. *Cell* 133, 66-77, doi:10.1016/j.cell.2008.01.046 [doi] (2008).

113 Khuon, S. *et al.* Myosin light chain kinase mediates transcellular intravasation of breast cancer cells through the underlying endothelial cells: a three-dimensional FRET study. *Journal of cell science* 123, 431-440, doi:10.1242/jcs.053793 [doi] (2010).

114 Erler, J. T. *et al.* Hypoxia-induced lysyl oxidase is a critical mediator of bone marrow cell recruitment to form the premetastatic niche. *Cancer cell* 15, 35-44, doi:10.1016/j.ccr.2008.11.012 [doi] (2009).

115 Kaplan, R. N. *et al.* VEGFR1-positive haematopoietic bone marrow progenitors initiate the pre-metastatic niche. *Nature* 438, 820-827 (2005).

116 Hiratsuka, S., Watanabe, A., Aburatani, H. & Maru, Y. Tumour-mediated upregulation of chemoattractants and recruitment of myeloid cells predetermines lung metastasis. *Nature cell biology* 8, 1369-1375, doi:ncb1507 [pii] (2006).

117 Sosa, M. S., Bragado, P. & Aguirre-Ghiso, J. A. Mechanisms of disseminated cancer cell dormancy: an awakening field. *Nature reviews.Cancer* 14, 611-622, doi:10.1038/nrc3793 [doi] (2014).

118 Aguirre-Ghiso, J. A. Models, mechanisms and clinical evidence for cancer dormancy. *Nature reviews.Cancer* 7, 834-846, doi:nrc2256 [pii] (2007).

119 Gao, H. *et al.* The BMP inhibitor Coco reactivates breast cancer cells at lung metastatic sites. *Cell* 150, 764-779, doi:10.1016/j.cell.2012.06.035 [doi] (2012).

120 Zhang, X. H. *et al.* Latent bone metastasis in breast cancer tied to Src-dependent survival signals. *Cancer cell* 16, 67-78, doi:10.1016/j.ccr.2009.05.017 [doi] (2009).

121 Mazzieri, R. *et al.* Targeting the ANG2/TIE2 axis inhibits tumor growth and metastasis by impairing angiogenesis and disabling rebounds of proangiogenic myeloid cells. *Cancer cell* 19, 512-526, doi:10.1016/j.ccr.2011.02.005 [doi] (2011).

122 Weilbaecher, K. N., Guise, T. A. & McCauley, L. K. Cancer to bone: a fatal attraction. *Nature reviews.Cancer* 11, 411-425, doi:10.1038/nrc3055 [doi] (2011).

123 Ell, B. & Kang, Y. SnapShot: Bone Metastasis. *Cell* 151, 690-690.e691, doi:10.1016/j.cell.2012.10.005 [doi] (2012).

124 Oskarsson, T. *et al.* Breast cancer cells produce tenascin C as a metastatic niche component to colonize the lungs. *Nature medicine* 17, 867-874, doi:10.1038/nm.2379 [doi] (2011).

125 Gupta, G. P. *et al.* ID genes mediate tumor reinitiation during breast cancer lung metastasis. *Proceedings of the National Academy of Sciences of the United States of America* 104, 19506-19511, doi:0709185104 [pii] (2007).

126 Acharyya, S. *et al.* A CXCL1 paracrine network links cancer chemoresistance and metastasis. *Cell* 150, 165-178, doi:10.1016/j.cell.2012.04.042 [doi] (2012).

127 Chen, Q., Zhang, X. H. & Massague, J. Macrophage binding to receptor VCAM-1 transmits survival signals in breast cancer cells that invade the lungs. *Cancer cell* 20, 538-549, doi:10.1016/j.ccr.2011.08.025 [doi] (2011).

128 Morales, M. *et al.* RARRES3 suppresses breast cancer lung metastasis by regulating adhesion and differentiation. *EMBO molecular medicine* 6, 865-881, doi:10.15252/emmm.201303675 [doi] (2014).

129 Labelle, M., Begum, S. & Hynes, R. O. Direct signaling between platelets and cancer cells induces an epithelial-mesenchymal-like transition and promotes metastasis. *Cancer cell* 20, 576-590, doi:10.1016/j.ccr.2011.09.009 [doi] (2011).

130 Wolf, M. J. *et al.* Endothelial CCR2 signaling induced by colon carcinoma cells enables extravasation via the JAK2-Stat5 and p38MAPK pathway. *Cancer cell* 22, 91-105, doi:10.1016/j.ccr.2012.05.023 [doi] (2012).

131 Qian, B. Z. *et al.* CCL2 recruits inflammatory monocytes to facilitate breast-tumour metastasis. *Nature* 475, 222-225, doi:10.1038/nature10138 [doi] (2011).

132 Talmadge, J. E. & Fidler, I. J. AACR centennial series: the biology of cancer metastasis: historical perspective. *Cancer research* 70, 5649-5669, doi:10.1158/0008-5472.CAN-10-1040 [doi] (2010).

133 Fidler, I. The pathogenesis of cancer metastasis: the 'seed and soil' hypothesis revisited. *Nature Reviews Cancer* 3, 453-458 (2003).

134 Psaila, B. & Lyden, D. The metastatic niche: adapting the foreign soil. *Nature reviews.Cancer* 9, 285-293, doi:10.1038/nrc2621 [doi] (2009).

135 Shibue, T. & Weinberg, R. A. Metastatic colonization: settlement, adaptation and propagation of tumor cells in a foreign tissue environment. *Seminars in cancer biology* 21, 99-106, doi:10.1016/j.semcancer.2010.12.003 [doi] (2011).

136 Tabaries, S. *et al.* Claudin-2 is selectively enriched in and promotes the formation of breast cancer liver metastases through engagement of integrin complexes. *Oncogene* 30, 1318-1328, doi:10.1038/onc.2010.518 [doi] (2011).

137 Mundy, G. Metastasis to bone: causes, consequences and therapeutic opportunities. *Nature Reviews Cancer* 2, 584-593 (2002).

138 Olechnowicz, S. W. & Edwards, C. M. Contributions of the host microenvironment to cancer-induced bone disease. *Cancer research* 74, 1625-1631, doi:10.1158/0008-5472.CAN-13-2645 [doi] (2014).

139 Lu, X. *et al.* VCAM-1 promotes osteolytic expansion of indolent bone micrometastasis of breast cancer by engaging alpha4beta1-positive osteoclast progenitors. *Cancer cell* 20, 701-714, doi:10.1016/j.ccr.2011.11.002 [doi] (2011).

140 Fukudome, K. & Esmon, C. T. Identification, cloning, and regulation of a novel endothelial cell protein C/activated protein C receptor. *The Journal of biological chemistry* 269, 26486-26491 (1994).

141 Simmonds, R. E. & Lane, D. A. Structural and functional implications of the intron/exon organization of the human endothelial cell protein C/activated protein C receptor (EPCR) gene: comparison with the structure of CD1/major histocompatibility complex alpha1 and alpha2 domains. *Blood* 94, 632-641 (1999).

142 Oganesyan, V. *et al.* The crystal structure of the endothelial protein C receptor and a bound phospholipid. *The Journal of biological chemistry* 277, 24851-24854, doi:10.1074/jbc.C200163200 [doi] (2002).

143 Liaw, P. C., Mather, T., Oganesyan, N., Ferrell, G. L. & Esmon, C. T. Identification of the protein C/activated protein C binding sites on the endothelial cell protein C receptor. Implications for a novel mode of ligand recognition by a major histocompatibility complex class 1-type receptor. *The Journal of biological chemistry* 276, 8364-8370, doi:10.1074/jbc.M010572200 [doi] (2001).

144 Lopez-Sagaseta, J. *et al.* sPLA2-V inhibits EPCR anticoagulant and antiapoptotic properties by accommodating lysophosphatidylcholine or PAF in the hydrophobic groove. *Blood* 119, 2914-2921, doi:10.1182/blood-2011-05-353409 [doi] (2012).

145 Nayak, R. *et al.* Endothelial cell protein C receptor cellular localization and trafficking: potential functional implications. *Blood* 114, 1974-1986 (2009).

146 Esmon, C. T. The endothelial cell protein C receptor. *Thrombosis and haemostasis* 83, 639-643 (2000).

147 Mohan Rao, L. V., Esmon, C. T. & Pendurthi, U. R. Endothelial cell protein C receptor: a multiliganded and multifunctional receptor. *Blood* 124, 1553-1562, doi:10.1182/blood-2014-05-578328 [doi] (2014).

148 Qu, D., Wang, Y., Esmon, N. L. & Esmon, C. T. Regulated endothelial protein C receptor shedding is mediated by tumor necrosis factor-alpha converting enzyme/ADAM17. *Journal of thrombosis and haemostasis* 5, 395-402 (2007).

149 Qu, D., Wang, Y., Song, Y., Esmon, N. L. & Esmon, C. T. The Ser219-->Gly dimorphism of the endothelial protein C receptor contributes to the higher soluble protein levels observed in individuals with the A3 haplotype. *Journal of thrombosis and haemostasis : JTH* 4, 229-235, doi:JTH1676 [pii] (2006).

150 Kurosawa, S., Stearns-Kurosawa, D. J., Hidari, N. & Esmon, C. T. Identification of functional endothelial protein C receptor in human plasma. *The Journal of clinical investigation* 100, 411-418, doi:10.1172/JCI119548 [doi] (1997).

151 Fukudome, K. *et al.* The endothelial cell protein C receptor. Cell surface expression and direct ligand binding by the soluble receptor. *The Journal of biological chemistry* 271, 17491-17498 (1996).

152 Liaw, P. C., Neuenschwander, P. F., Smirnov, M. D. & Esmon, C. T. Mechanisms by which soluble endothelial cell protein C receptor modulates protein C and activated protein C function. *The Journal of biological chemistry* 275, 5447-5452 (2000).

153 Ye, X. *et al.* The endothelial cell protein C receptor (EPCR) functions as a primary receptor for protein C activation on endothelial cells in arteries, veins, and capillaries. *Biochemical and biophysical research communications* 259, 671-677, doi:10.1006/bbrc.1999.0846 [doi] (1999).

154 Laszik, Z., Mitro, A., Taylor, F. B., Jr., Ferrell, G. & Esmon, C. T. Human protein C receptor is present primarily on endothelium of large blood vessels: implications for the control of the protein C pathway. *Circulation* 96, 3633-3640 (1997).

155 Stephenson, D. A., Toltl, L. J., Beaudin, S. & Liaw, P. C. Modulation of monocyte function by activated protein C, a natural anticoagulant. *Journal of immunology (Baltimore, Md.: 1950)* 177, 2115-2122, doi:177/4/2115 [pii] (2006).

156 Xue, M., March, L., Sambrook, P. N., Fukudome, K. & Jackson, C. J. Endothelial protein C receptor is overexpressed in rheumatoid arthritic (RA) synovium and mediates the anti-inflammatory effects of activated protein C in RA monocytes. *Annals of the Rheumatic Diseases* 66, 1574-1580, doi:ard.2006.068239 [pii] (2007).

157 Sturn, D. H. *et al.* Expression and function of the endothelial protein C receptor in human neutrophils. *Blood* 102, 1499-1505, doi:10.1182/blood-2002-12-3880 [doi] (2003).

158 Bretschneider, E. *et al.* Human vascular smooth muscle cells express functionally active endothelial cell protein C receptor. *Circulation research* 100, 255-262, doi:01.RES.0000255685.06922.c7 [pii] (2007).

159 Xue, M., Campbell, D. & Jackson, C. J. Protein C is an autocrine growth factor for human skin keratinocytes. *The Journal of biological chemistry* 282, 13610-13616, doi:M610740200 [pii] (2007).

160 Faioni, E. M. *et al.* Activation of Protein C in Human Trophoblasts in Culture and Downregulation of Trophoblast Endothelial Protein C Receptor by TNF-alpha. *Reproductive sciences (Thousand Oaks, Calif.)*, doi:1933719115570904 [pii] (2015).

161 Wang, J., Yang, L., Rezaie, A. R. & Li, J. Activated protein C protects against myocardial ischemic/reperfusion injury through AMP-activated protein kinase signaling. *Journal of thrombosis and haemostasis : JTH* 9, 1308-1317, doi:10.1111/j.1538-7836.2011.04331.x [doi] (2011).

162 Kurata, T. *et al.* Activated protein C stimulates osteoblast proliferation via endothelial protein C receptor. *Thrombosis research* 125, 184-191, doi:10.1016/j.thromres.2009.09.005 [doi] (2010).

163 Jackson, M. T. *et al.* Activation of cartilage matrix metalloproteinases by activated protein C. *Arthritis and Rheumatism* 60, 780-791, doi:10.1002/art.24303 [doi] (2009).

164 Julovi, S. M. *et al.* Activated protein C inhibits proliferation and tumor necrosis factor alpha-stimulated activation of p38, c-Jun NH2-terminal kinase (JNK) and Akt in rheumatoid synovial fibroblasts. *Molecular medicine (Cambridge, Mass.)* 19, 324-331, doi:10.2119/molmed.2013.00034 [doi] (2013).

165 Balazs, A. B., Fabian, A. J., Esmon, C. T. & Mulligan, R. C. Endothelial protein C receptor (CD201) explicitly identifies hematopoietic stem cells in murine bone marrow. *Blood* 107, 2317-2321, doi:2005-06-2249 [pii] (2006).

166 Ivanova, N. B. *et al.* A stem cell molecular signature. *Science (New York, N.Y.)* 298, 601-604, doi:10.1126/science.1073823 [doi] (2002).

167 Ramalho-Santos, M., Yoon, S., Matsuzaki, Y., Mulligan, R. C. & Melton, D. A. "Stemness": transcriptional profiling of embryonic and adult stem cells. *Science (New York, N.Y.)* 298, 597-600, doi:10.1126/science.1072530 [doi] (2002).

168 Wang, D. *et al.* Identification of multipotent mammary stem cells by protein C receptor expression. *Nature* 517, 81-84, doi:10.1038/nature13851 [doi] (2015).

169 Regan, L. M., Mollica, J. S., Rezaie, A. R. & Esmon, C. T. The interaction between the endothelial cell protein C receptor and protein C is dictated by the gamma-carboxyglutamic acid domain of protein C. *The Journal of biological chemistry* 272, 26279-26284 (1997).

170 Ghosh, S., Pendurthi, U. R., Steinoe, A., Esmon, C. T. & Rao, L. V. Endothelial cell protein C receptor acts as a cellular receptor for factor VIIa on endothelium. *The Journal of biological chemistry* 282, 11849-11857, doi:M609283200 [pii] (2007).

171 Preston, R. J. *et al.* Multifunctional specificity of the protein C/activated protein C Gla domain. *The Journal of biological chemistry* 281, 28850-28857, doi:M604966200 [pii] (2006).

172 Lopez-Sagaseta, J. *et al.* Binding of factor VIIa to the endothelial cell protein C receptor reduces its coagulant activity. *Journal of thrombosis and haemostasis : JTH* 5, 1817-1824, doi:JTH2648 [pii] (2007).

173 Montes, R., Puy, C., Molina, E. & Hermida, J. Is EPCR a multi-ligand receptor? Pros and cons. *Thrombosis and haemostasis* 107, 815-826, doi:10.1160/TH11-11-0766 [doi] (2012).

174 Sen, P. *et al.* Factor VIIa binding to endothelial cell protein C receptor: differences between mouse and human systems. *Thrombosis and haemostasis* 107, 951-961, doi:10.1160/TH11-09-0672 [doi] (2012).

175 Puy, C., Hermida, J. & Montes, R. Factor X and factor VII binding to endothelial protein C receptor differs between species. *Journal of thrombosis and haemostasis : JTH* 9, 1255-1257, doi:10.1111/j.1538-7836.2011.04295.x [doi] (2011).

176 Gleeson, E. M., O'Donnell, J. S. & Preston, R. J. The endothelial cell protein C receptor: cell surface conductor of cytoprotective coagulation factor signaling. *Cellular and molecular life sciences : CMLS* 69, 717-726, doi:10.1007/s00018-011-0825-0 [doi] (2012).

177 Kurosawa, S., Esmon, C. T. & Stearns-Kurosawa, D. J. The soluble endothelial protein C receptor binds to activated neutrophils: involvement of proteinase-3 and CD11b/CD18. *Journal of immunology (Baltimore, Md.: 1950)* 165, 4697-4703 (2000).

178 Villegas-Mendez, A. *et al.* Proteolysis of the endothelial cell protein C receptor by neutrophil proteinase 3. *Journal of thrombosis and haemostasis : JTH* 5, 980-988, doi:JTH2480 [pii] (2007).

179 Fink, K. *et al.* Mac-1 directly binds to the endothelial protein C-receptor: a link between the protein C anticoagulant pathway and inflammation? *PloS one* 8, e53103, doi:10.1371/journal.pone.0053103 [doi] (2013).

180 Willcox, C. R. *et al.* Cytomegalovirus and tumor stress surveillance by binding of a human gammadelta T cell antigen receptor to endothelial protein C receptor. *Nature immunology* 13, 872-879, doi:10.1038/ni.2394 [doi] (2012).

181 Witherden, D. A. & Havran, W. L. EPCR: a stress trigger for gammadelta T cells. *Nature immunology* 13, 812-814, doi:10.1038/ni.2398 [doi] (2012).

182 Ho, M. EPCR: holy grail of malaria cytoadhesion? *Blood* 123, 157-159, doi:10.1182/blood-2013-12-541318 [doi] (2014).

183 Kahrstrom, C. T. Parasite biology: EPCR unlocks severe malaria. *Nature reviews.Microbiology* 11, 433, doi:10.1038/nrmicro3055 [doi] (2013).

184 Aird, W. C., Mosnier, L. O. & Fairhurst, R. M. Plasmodium falciparum picks (on) EPCR. *Blood* 123, 163-167, doi:10.1182/blood-2013-09-521005 [doi] (2014).

185 Turner, L. *et al.* Severe malaria is associated with parasite binding to endothelial protein C receptor. *Nature* 498, 502-505, doi:10.1038/nature12216 [doi] (2013).

186 Stearns-Kurosawa, D. J., Kurosawa, S., Mollica, J. S., Ferrell, G. L. & Esmon, C. T. The endothelial cell protein C receptor augments protein C activation by the thrombin-thrombomodulin complex. *Proceedings of the National Academy of Sciences of the United States of America* 93, 10212-10216 (1996).

187 Esmon, C. T. *et al.* Regulation and functions of the protein C anticoagulant pathway. *Haematologica* 84, 363-368 (1999).

188 Tsuneyoshi, N. *et al.* Expression and anticoagulant function of the endothelial cell protein C receptor (EPCR) in cancer cell lines. *Thrombosis and haemostasis* 85, 356-361 (2001).

189 Bouwens, E. A., Stavenuiter, F. & Mosnier, L. O. Mechanisms of anticoagulant and cytoprotective actions of the protein C pathway. *Journal of thrombosis and haemostasis : JTH* 11 Suppl 1, 242-253, doi:10.1111/jth.12247 [doi] (2013).

190 Disse, J. *et al.* The endothelial protein C receptor supports tissue factor ternary coagulation initiation complex signaling through protease-activated receptors. *The Journal of biological chemistry* 286, 5756-5767, doi:10.1074/jbc.M110.201228 [doi] (2011).

191 Feistritzer, C. *et al.* Protective signaling by activated protein C is mechanistically linked to protein C activation on endothelial cells. *Journal of Biological Chemistry* 281, 20077-20084 (2006).

192 Mosnier, L. O., Zlokovic, B. V. & Griffin, J. H. The cytoprotective protein C pathway. *Blood* 109, 3161-3172, doi:blood-2006-09-003004 [pii] (2007).

193 Cheng, T. *et al.* Activated protein C blocks p53-mediated apoptosis in ischemic human brain endothelium and is neuroprotective. *Nature medicine* 9, 338-342, doi:10.1038/nm826 [doi] (2003).

194 Liu, D. *et al.* Tissue plasminogen activator neurovascular toxicity is controlled by activated protein C. *Nature medicine* 10, 1379-1383, doi:nm1122 [pii] (2004).

195 Brueckmann, M. *et al.* Activated protein C inhibits the release of macrophage inflammatory protein-1-alpha from THP-1 cells and from human monocytes. *Cytokine* 26, 106-113, doi:10.1016/j.cyto.2004.01.004 [doi] (2004).

196 White, B. *et al.* Activated protein C inhibits lipopolysaccharide-induced nuclear translocation of nuclear factor kappaB (NF-kappaB) and tumour necrosis factor alpha (TNF-alpha) production in the THP-1 monocytic cell line. *British journal of haematology* 110, 130-134, doi:bjh2128 [pii] (2000).

197 Toltl, L. J., Beaudin, S., Liaw, P. C. & Canadian Critical Care Translational Biology, G. Activated protein C up-regulates IL-10 and inhibits tissue factor in blood monocytes. *Journal of immunology (Baltimore, Md.: 1950)* 181, 2165-2173, doi:181/3/2165 [pii] (2008).

198 Feistritzer, C. & Riewald, M. Endothelial barrier protection by activated protein C through PAR1-dependent sphingosine 1-phosphate receptor-1 crossactivation. *Blood* 105, 3178-3184, doi:2004-10-3985 [pii] (2005).

199 Finigan, J. H. *et al.* Activated protein C mediates novel lung endothelial barrier enhancement: role of sphingosine 1-phosphate receptor transactivation. *The Journal of biological chemistry* 280, 17286-17293, doi:M412427200 [pii] (2005).

200 Minhas, N., Xue, M., Fukudome, K. & Jackson, C. J. Activated protein C utilizes the angiopoietin/Tie2 axis to promote endothelial barrier function. *FASEB journal : official publication of the Federation of American Societies for Experimental Biology* 24, 873-881, doi:10.1096/fj.09-134445 [doi] (2010).

201 Stavenuiter, F. & Mosnier, L. O. Noncanonical PAR3 activation by factor Xa identifies a novel pathway for Tie2 activation and stabilization of vascular integrity. *Blood* 124, 3480-3489, doi:10.1182/blood-2014-06-582775 [doi] (2014).

202 Vu, T. K., Hung, D. T., Wheaton, V. I. & Coughlin, S. R. Molecular cloning of a functional thrombin receptor reveals a novel proteolytic mechanism of receptor activation. *Cell* 64, 1057-1068, doi:0092-8674(91)90261-V [pii] (1991).

203 Coughlin, S. R. Thrombin signalling and protease-activated receptors. *Nature* 407, 258-264, doi:10.1038/35025229 [doi] (2000).

204 Bae, J. S., Yang, L. & Rezaie, A. R. Lipid raft localization regulates the cleavage specificity of protease activated receptor 1 in endothelial cells. *Journal of thrombosis and haemostasis : JTH* 6, 954-961, doi:10.1111/j.1538-7836.2008.02924.x [doi] (2008).

205 Russo, A., Soh, U. J., Paing, M. M., Arora, P. & Trejo, J. Caveolae are required for protease-selective signaling by protease-activated receptor-1. *Proceedings of the National Academy of Sciences of the United States of America* 106, 6393-6397, doi:10.1073/pnas.0810687106 [doi] (2009).

206 Bae, J. S., Yang, L. & Rezaie, A. R. Receptors of the protein C activation and activated protein C signaling pathways are colocalized in lipid rafts of endothelial cells. *Proceedings of the National Academy of Sciences of the United States of America* 104, 2867-2872, doi:0611493104 [pii] (2007).

207 Bae, J. S., Yang, L., Manithody, C. & Rezaie, A. R. The ligand occupancy of endothelial protein C receptor switches the protease-activated receptor 1-dependent signaling specificity of thrombin from a permeability-enhancing to a barrier-protective response in endothelial cells. *Blood* 110, 3909-3916, doi:blood-2007-06-096651 [pii] (2007).

208 Bae, J. S. & Rezaie, A. R. Protease activated receptor 1 (PAR-1) activation by thrombin is protective in human pulmonary artery endothelial cells if endothelial protein C receptor is occupied by its natural ligand. *Thrombosis and haemostasis* 100, 101-109, doi:10.1160/TH08-02-0127 [doi] (2008).

209 Bae, J. S. & Rezaie, A. R. Thrombin inhibits HMGB1-mediated proinflammatory signaling responses when endothelial protein C receptor is occupied by its natural ligand. *BMB reports* 46, 544-549, doi:2274 [pii] (2013).

210 Rezaie, A. R. The occupancy of endothelial protein C receptor by its ligand modulates the par-1 dependent signaling specificity of coagulation proteases. *IUBMB life* 63, 390-396, doi:10.1002/iub.447 [doi] (2011).

211 Soh, U. J. & Trejo, J. Activated protein C promotes protease-activated receptor-1 cytoprotective signaling through beta-arrestin and dishevelled-2 scaffolds. *Proceedings of the National Academy of Sciences of the United States of America* 108, E1372-1380, doi:10.1073/pnas.1112482108 [doi] (2011).

212 Esmon, C. The protein C pathway. *Chest* 124, 26S-32S (2003).

213 Mosnier, L. O., Sinha, R. K., Burnier, L., Bouwens, E. A. & Griffin, J. H. Biased agonism of protease-activated receptor 1 by activated protein C caused by noncanonical cleavage at Arg46. *Blood* 120, 5237-5246, doi:10.1182/blood-2012-08-452169 [doi] (2012).

214 Schuepbach, R. A., Madon, J., Ender, M., Galli, P. & Riewald, M. Protease-activated receptor-1 cleaved at R46 mediates cytoprotective effects. *Journal of thrombosis and haemostasis : JTH* 10, 1675-1684, doi:10.1111/j.1538-7836.2012.04825.x [doi] (2012).

215 Schuepbach, R. A., Feistritzer, C., Brass, L. F. & Riewald, M. Activated protein C-cleaved protease activated receptor-1 is retained on the endothelial cell surface even in the presence of thrombin. *Blood* 111, 2667-2673, doi:blood-2007-09-113076 [pii] (2008).

216 Burleigh, A. *et al.* A co-culture genome-wide RNAi screen with mammary epithelial cells reveals transmembrane signals required for growth and differentiation. *Breast cancer research : BCR* 17, 4-014-0510-y, doi:10.1186/s13058-014-0510-y [doi] (2015).

217 Anton, I. *et al.* Receptor of activated protein C promotes metastasis and correlates with clinical outcome in lung adenocarcinoma. *American journal of respiratory and critical care medicine* 186, 96-105, doi:10.1164/rccm.201110-1826OC [doi] (2012).

218 Beaulieu, L. M. & Church, F. C. Activated protein C promotes breast cancer cell migration through interactions with EPCR and PAR-1. *Experimental cell research* 313, 677-687, doi:S0014-4827(06)00474-5 [pii] (2007).

219 Ducros, E. *et al.* Endothelial protein C receptor expressed by ovarian cancer cells as a possible biomarker of cancer onset. *International journal of oncology* 41, 433-440, doi:10.3892/ijo.2012.1492 [doi] (2012).

220 Scheffer, G. L. *et al.* Expression of the vascular endothelial cell protein C receptor in epithelial tumour cells. *European journal of cancer* 38, 1535-1542.

221 Keshava, S. *et al.* Endothelial cell protein C receptor opposes mesothelioma growth driven by tissue factor. *Cancer research* 73, 3963-3973, doi:10.1158/0008-5472.CAN-12-1690 [doi] (2013).

222 Bezuhly, M. *et al.* Role of activated protein C and its receptor in inhibition of tumor metastasis. *Blood* 113, 3371-3374 (2009).

223 Heng, W., Mu, C. Y., Chen, C., Huang, J. A. & Wang, Z. Y. Endothelial cell protein C receptor (EPCR) is expressed by lung carcinoma and correlated with clinical parameters. *Clinical laboratory* 59, 375-380 (2013).

224 Heng, W., Huang, J. A. & Wang, Z. Y. Inhibition of cellular growth and migration by suppression of endothelial protein C receptor (EPCR) in lung carcinoma cells. *Oncology research* 20, 231-240 (2012).

225 Wang, Q. *et al.* Endothelial cell protein C receptor promotes MGC803 gastric cancer cells proliferation and migration by activating ERK1/2. *Medical oncology (Northwood, London, England)* 32, 162-015-0614-y. Epub 2015 Apr 0621, doi:10.1007/s12032-015-0614-y [doi] (2015).

226 Park, S. Y. *et al.* Heterogeneity for stem cell-related markers according to tumor subtype and histologic stage in breast cancer. *Clinical cancer research : an official journal of the American Association for Cancer Research* 16, 876-887, doi:10.1158/1078-0432.CCR-09-1532 [doi] (2010).

227 Schaffner, F. *et al.* Endothelial protein C receptor function in murine and human breast cancer development. *PloS one* 8, e61071, doi:10.1371/journal.pone.0061071 [doi] (2013).

228 Keshava, S., Kothari, H., Rao, L. V. & Pendurthi, U. R. Influence of endothelial cell protein C receptor on breast cancer development. *Journal of thrombosis and haemostasis : JTH* 11, 2062-2065, doi:10.1111/jth.12402 [doi] (2013).

229 Gramling, M. W., Beaulieu, L. M. & Church, F. C. Activated protein C enhances cell motility of endothelial cells and MDA-MB-231 breast cancer cells by intracellular signal transduction. *Experimental cell research* 316, 314-328, doi:10.1016/j.yexcr.2009.10.024 [doi] (2010).

230 Poole, D., Bertolini, G. & Garattini, S. Withdrawal of 'Xigris' from the market: old and new lessons. *Journal of epidemiology and community health* 66, 571-572, doi:10.1136/jech-2012-200977 [doi] (2012).

231 Cailleau, R., Young, R., Olive, M. & Reeves, W. J., Jr. Breast tumor cell lines from pleural effusions. *Journal of the National Cancer Institute* 53, 661-674 (1974).

232 Knutson, K. L., Almand, B., Dang, Y. & Disis, M. L. Neu antigen-negative variants can be generated after neu-specific antibody therapy in neu transgenic mice. *Cancer research* 64, 1146-1151 (2004).

233 Knutson, K. L. *et al.* Immunoediting of cancers may lead to epithelial to mesenchymal transition. *Journal of immunology (Baltimore, Md.: 1950)* 177, 1526-1533, doi:177/3/1526 [pii] (2006).

234 Santisteban, M. *et al.* Immune-induced epithelial to mesenchymal transition in vivo generates breast cancer stem cells. *Cancer research* 69, 2887-2895, doi:10.1158/0008-5472.CAN-08-3343 [doi] (2009).

235 Ogawa, M. *et al.* B cell ontogeny in murine embryo studied by a culture system with the monolayer of a stromal cell clone, ST2: B cell progenitor develops first in the embryonal body rather than in the yolk sac. *The EMBO journal* 7, 1337-1343 (1988).

236 Ponomarev, V. *et al.* A novel triple-modality reporter gene for whole-body fluorescent, bioluminescent, and nuclear noninvasive imaging. *European journal of nuclear medicine and molecular imaging* 31, 740-751 (2004).

237 Schindelin, J. *et al.* Fiji: an open-source platform for biological-image analysis. *Nature methods* 9, 676-682, doi:10.1038/nmeth.2019 [doi] (2012).

238 Wang, Y. *et al.* Gene-expression profiles to predict distant metastasis of lymph-node-negative primary breast cancer. *Lancet* 365, 671-679 (2005).

239 Vargo-Gogola, T. & Rosen, J. M. Modelling breast cancer: one size does not fit all. *Nature reviews.Cancer* 7, 659-672, doi:nrc2193 [pii] (2007).

240 Kim, M. Y. *et al.* Tumor self-seeding by circulating cancer cells. *Cell* 139, 1315-1326, doi:10.1016/j.cell.2009.11.025 [doi] (2009).

241 Murakami, K. *et al.* Activated protein C attenuates endotoxin-induced pulmonary vascular injury by inhibiting activated leukocytes in rats. *Blood* 87, 642-647 (1996).

242 Feistritzer, C., Sturn, D. H., Kaneider, N. C., Djanani, A. & Wiedermann, C. J. Endothelial protein C receptor-dependent inhibition of human eosinophil chemotaxis by protein C. *The Journal of allergy and clinical immunology* 112, 375-381, doi:S0091674903015409 [pii] (2003).

243 Ein-Dor, L., Kela, I., Getz, G., Givol, D. & Domany, E. Outcome signature genes in breast cancer: is there a unique set? *Bioinformatics (Oxford, England)* 21, 171-178, doi:10.1093/bioinformatics/bth469 [doi] (2005).

244 Massague, J. Sorting out breast-cancer gene signatures. *The New England journal of medicine* 356, 294-297, doi:356/3/294 [pii] (2007).

245 Fantozzi, A. & Christofori, G. Mouse models of breast cancer metastasis. *Breast cancer research : BCR* 8, 212, doi:bcr1530 [pii] (2006).

246 Bos, P. D., Nguyen, D. X. & Massague, J. Modeling metastasis in the mouse. *Current opinion in pharmacology* 10, 571-577, doi:10.1016/j.coph.2010.06.003 [doi] (2010).

247 Pepler, L., Yu, P., Dwivedi, D. J., Trigatti, B. L. & Liaw, P. C. Characterization of mice harboring a variant of EPCR with impaired ability to bind protein C: Novel role of EPCR in hematopoiesis. *Blood*, doi:blood-2014-02-558940 [pii] (2015).

248 Preston, R. J. *et al.* Selective modulation of protein C affinity for EPCR and phospholipids by Gla domain mutation. *The FEBS journal* 272, 97-108, doi:EJB4401 [pii] (2005).

249 Biguzzi, E. *et al.* A 23bp insertion in the endothelial protein C receptor (EPCR) gene impairs EPCR function. *Thrombosis and haemostasis* 86, 945-948, doi:01100945 [pii] (2001).

250 Wang, W., Erbe, A. K., Hank, J. A., Morris, Z. S. & Sondel, P. M. NK Cell-Mediated Antibody-Dependent Cellular Cytotoxicity in Cancer Immunotherapy. *Frontiers in immunology* 6, 368, doi:10.3389/fimmu.2015.00368 (2015).

251 Bakema, J. E. & van Egmond, M. Fc receptor-dependent mechanisms of monoclonal antibody therapy of cancer. *Current topics in microbiology and immunology* 382, 373-392, doi:10.1007/978-3-319-07911-0_17 (2014).

252 Boroughs, L. K. & DeBerardinis, R. J. Metabolic pathways promoting cancer cell survival and growth. *Nature cell biology* 17, 351-359, doi:10.1038/ncb3124 [doi] (2015).

253 Anastas, J. N. & Moon, R. T. WNT signalling pathways as therapeutic targets in cancer. *Nature reviews.Cancer* 13, 11-26, doi:10.1038/nrc3419 [doi] (2013).

254 Wu, F. H. *et al.* Extracellular HSPA1A promotes the growth of hepatocarcinoma by augmenting tumor cell proliferation and apoptosis-resistance. *Cancer letters* 317, 157-164, doi:10.1016/j.canlet.2011.11.020 [doi] (2012).

255 Kaur, P. *et al.* A mouse model for triple-negative breast cancer tumor-initiating cells (TNBC-TICs) exhibits similar aggressive phenotype to the human disease. *BMC cancer* 12, 120-2407-2412-2120, doi:10.1186/1471-2407-12-120 [doi] (2012).

256 Mound, A., Rodat-Despoix, L., Bougarn, S., Ouadid-Ahidouch, H. & Matifat, F. Molecular interaction and functional coupling between type 3 inositol 1,4,5-trisphosphate receptor and BKCa channel stimulate breast cancer cell proliferation. *European journal of cancer (Oxford, England : 1990)* 49, 3738-3751, doi:10.1016/j.ejca.2013.07.013 [doi] (2013).

257 Kabir, N. N., Ronnstrand, L. & Kazi, J. U. Keratin 19 expression correlates with poor prognosis in breast cancer. *Molecular biology reports* 41, 7729-7735, doi:10.1007/s11033-014-3684-6 [doi] (2014).

258 Asfaha, S. *et al.* Krt19(+)/Lgr5(-) Cells Are Radioresistant Cancer-Initiating Stem Cells in the Colon and Intestine. *Cell stem cell* 16, 627-638, doi:10.1016/j.stem.2015.04.013 [doi] (2015).

259 Savoy, R. M. & Ghosh, P. M. The dual role of filamin A in cancer: can't live with (too much of) it, can't live without it. *Endocrine-related cancer* 20, R341-356, doi:10.1530/ERC-13-0364 [doi] (2013).

260 Bandaru, S. *et al.* Targeting filamin B induces tumor growth and metastasis via enhanced activity of matrix metalloproteinase-9 and secretion of VEGF-A. *Oncogenesis* 3, e119, doi:10.1038/oncsis.2014.33 [doi] (2014).

261 Adachi-Hayama, M. *et al.* Circulating anti-filamin C autoantibody as a potential serum biomarker for low-grade gliomas. *BMC cancer* 14, 452-2407-2414-2452, doi:10.1186/1471-2407-14-452 [doi] (2014).

262 Shu, Y. J. *et al.* SPOCK1 as a potential cancer prognostic marker promotes the proliferation and metastasis of gallbladder cancer cells by activating the PI3K/AKT pathway. *Molecular cancer* 14, 12-014-0276-y, doi:10.1186/s12943-014-0276-y [doi] (2015).

263 Li, Y. *et al.* SPOCK1 is regulated by CHD1L and blocks apoptosis and promotes HCC cell invasiveness and metastasis in mice. *Gastroenterology* 144, 179-191.e174, doi:10.1053/j.gastro.2012.09.042 [doi] (2013).

264 Miao, L. *et al.* SPOCK1 is a novel transforming growth factor-beta target gene that regulates lung cancer cell epithelial-mesenchymal transition. *Biochemical and biophysical research communications* 440, 792-797, doi:10.1016/j.bbrc.2013.10.024 [doi] (2013).

265 Spencer, V. A., Xu, R. & Bissell, M. J. Gene expression in the third dimension: the ECM-nucleus connection. *Journal of mammary gland biology and neoplasia* 15, 65-71, doi:10.1007/s10911-010-9163-3 [doi] (2010).

266 Vidi, P. A., Bissell, M. J. & Lelievre, S. A. Three-dimensional culture of human breast epithelial cells: the how and the why. *Methods in molecular biology (Clifton, N.J.)* 945, 193-219, doi:10.1007/978-1-62703-125-7_13 [doi] (2013).

267 Weigelt, B., Ghajar, C. M. & Bissell, M. J. The need for complex 3D culture models to unravel novel pathways and identify accurate biomarkers in breast cancer. *Advanced Drug Delivery Reviews* 69-70, 42-51, doi:10.1016/j.addr.2014.01.001 [doi] (2014).

VIII Appendixes

APPENDIX 1. Histological classification of breast tumors (WHO, 4th edition).

Invasive breast carcinomas (without microinvasive carcinoma and invasive papillary lesions)
Invasive carcinoma of no special type (NST)
Pleomorphic carcinoma
Carcinoma with osteoclast-like stromal giant cells
Carcinoma with choriocarcinomatous features
Carcinoma with melanotic features
Invasive lobular carcinoma
Classic lobular carcinoma
Solid lobular carcinoma
Alveolar lobular carcinoma
Pleomorphic lobular carcinoma
Tubulolobular carcinoma
Mixed lobular carcinoma
Tubular carcinoma
Cribriform carcinoma
Mucinous carcinoma
Carcinoma with medullary features
Medullary carcinoma
Atypical medullary carcinoma
Invasive carcinoma NST with medullary features
Carcinoma with apocrine differentiation
Carcinoma with signet-ring-cell differentiation
Invasive micropapillary carcinoma
Metaplastic carcinoma of no special type
Low-grade adenosquamous carcinoma
Fibromatosis-like metaplastic carcinoma
Squamous cell carcinoma
Spindle cell carcinoma
Metaplastic carcinoma with mesenchymal differentiation
Chondroid differentiation
Osseous differentiation
Other types of mesenchymal differentiation
Mixed metaplastic carcinoma
Myoepithelial carcinoma
Epithelial-myoepithelial tumors
Adenomyoepithelioma with carcinoma
Adenoid cystic carcinoma
Rare types
Carcinoma with neuroendocrine features
Neuroendocrine tumor, well-differentiated
Neuroendocrine carcinoma poorly differentiated (small cell carcinoma)
Carcinoma with neuroendocrine differentiation
Secretory carcinoma
Invasive papillary carcinoma
Acinic cell carcinoma
Mucoepidermoid carcinoma
Polymorphous carcinoma
Oncocytic carcinoma
Lipid-rich carcinoma
Glycogen-rich clear cell carcinoma
Sebaceous carcinoma

APPENDIX 2. TNM staging of breast tumors.

Stage	T (Primary tumor)	N (Lymph nodes)	M (Metastasis)
0	Tis	N0	M0
IA	T1*	N0	M0
IB	T0	N1mi	M0
	T1*	N1mi	M0
IIA	T0	N1**	M0
	T1*	N1**	M0
	T2	N0	M0
IIB	T2	N1	M0
	T3	N0	M0
IIIA	T0	N2	M0
	T1*	N2	M0
	T2	N2	M0
	T3	N1	M0
	T3	N2	M0
IIIB	T4	N0	M0
	T4	N1	M0
	T4	N2	M0
IIIC	Any T	N3	M0
IV	Any T	Any N	M1

* T1 includes T1mi. **T0 and T1 tumors with nodal micrometastases only are excluded from stage IIA and are classified stage IB.

Primary tumor (T)

T0	no evidence of primary tumor
Tis	carcinoma *in situ*
T1	tumor ≤ 20 mm in greatest dimension
T1mi	tumor ≤ 1 mm in greatest dimension
T2	tumor > 20 mm but ≤ 50 mm in greatest dimension
T3	tumor > 50 mm in greatest dimension
T4	tumor of any size with direct extension to the chest wall and/or to the skin (ulceration or skin nodules)

Regional lymph nodes (N)

N0	no regional lymph node metastases
N1	metastases to movable ipsilateral level I, II axillary lymph node(s)
N1mi	micrometastases (> 0.2 mm and/or > 200 cells but ≤ 2 mm)
N2	metastases in ipsilateral level I, II axillary lymph nodes that are clinically fixed or matted; or in clinically detected ipsilateral internal mammary nodes in the absence of clinically evident axillary lymph node metastases
N3	metastases in ipsilateral infraclavicular (level III axillary) lymph node(s) with or without level I, II axillary lymph node involvement; or in clinically detected ipsilateral internal mammary lymph node(s) with clinically evident level I, II axillary lymph node metastases; or metastases in ipsilateral supraclavicular lymph node(s) with or without axillary or internal mammary lymph node involvement

Distant metastases (M)

M0	no clinical or radiographic evidence of distant metastases
M1	distant detectable metastases as determined by classic clinical and radiographic means and/or histologically proven larger than 0.2 mm

APPENDIX 3. Identification of breast cancer driver genes in clinical samples.

Study	Samples	Methods	Driver genes		Altered signaling pathways
			Variation	Genes	
Shah *et al.*, 2009 (ref. 33)	One ER+ lobular primary tumor	Genome-seq RNA-seq	Prevalent mutation Low frequency mutation	HAUS3, PALB2, ABCB11, SLC24A4 KIF1C, USP28, MYH8, MORC1, KIAA1468, RNASEH2A	Not indicated
Shah *et al.*, 2012 (ref. 32)	104 primary TN breast cancer	Genome-seq RNA-seq Exome-seq	CNV Mutation Gene expression	PARK2, RB1, PTEN, EGFR TP53, PI3KCA, USH2A, ATR, MYO3A, UBR5, COL6A3, RB1, SYNE1, SYNE2, PTEN, GH1, BRCA2, BRAF, NRAS, HER2, HER3 TP53, PIK3CA, NRAS, EGFR, RB1, ATM, PRPS2, NRC31, PRKCZ, PRKCQ, PRKG1, PRKCE	TP53-related pathways Chromatin remodelling PI3K signaling HER signaling Integrin signaling and focal adhesions WNT/cadherin signaling Growth hormone and nuclear coactivators ATM/RB-related pathways
Banerji *et al.*, 2012 (ref. 34)	108 breast cancers of several subtypes	Genome-seq Exome-seq	Mutation Deletion Gene fusion	TP53, PIK3CA, AKT1, GATA3, MAP3K1, CBFB RUNX1 MAGI3-AKT3	AKT activation
Ellis *et al.*, 2012 (ref. 35)	77 ER+ tumors	Genome-seq Exome-seq	Mutation	PIK3CA, TP53, GATA3, CDH1, RB1, MLL3, MAP3K1, CDKN1B, TBX3, RUNX1, LDLRAP1, STNM2, MYH9, AGTR2, STMN2, SF3B1, CBFB	Apoptosis HER and PI3K signaling TP53/RB signaling MAPK/JNK pathways
Stephens *et al.*, 2012 (ref. 36)	79 ER+ tumors 21 ER- tumors	Exome-seq	Mutations, insertions and deletions	AKT1, BRCA1, CDH1, GATA3, PIK3CA, PTEN, RB1, TP53, HER2, MYC, FGFR1/ZNF703, CCND1, APC, ARID1A, ARID2, ASXL1, BAP1, KRAS, MAP2K4, MLL2, MLL3, NF1, SETD2, SF3B1, SMAD4, STK11, ARID1B, CASP8, MAP3K1, MAP3K13, NCOR1, CDKN1B, SMARCD1	JNK signaling AKT activation Chromatin remodelling Cell cycle progression Apoptosis Tumor-initiation

TCGA, 2012 (ref. 37)	825 breast tumors	mRNA microarrays Methylation chips SNP arrays miRNA seq Exome-seq RPPA	***Luminal/ER+ tumors***		
			Mutation	GATA3, FOXA1, RUNX1, PIK3CA, MAP3K1, MAP2K4, TP53	Apoptosis ER signaling
			Amplification	MDM2, FGFR, IGFR1, CCND1, CDK4, CDK6	PI3K signaling
			Deletion	ATM	MAPK/JNK signaling
			High expression	ESR1, GATA3, FOXA1, XBP1, MYB	Cell cycle progression
			Low expression	CDKN2C	Growth factor signaling
			HER2+ tumors*		
			Mutation	PIK3CA, HER2, EGFR, HER3	
				TP53 (HER2-E)	Cell cycle progression
				GATA3 (HER2-Lum)	Growth factor signaling
			Deletion	PTEN, INPP4B	ER signaling
			Amplification	FGFR, EGFR, CDK4, CCND1	Apoptosis
			High expression	FGFR4, EGFR, HER2, GRB7 (HER2-E) GATA3, BCL2, ESR1 (HER2-Lum)	PI3K signaling
			Basal-like tumors		
			Mutation	TP53 (80%), PIK3CA, ATM, RB1, BRCA1/2	
			Amplification	PIK3CA, MYC, CCNE1, KRAS, BRAF, EGFR, FGFR1, FGFR2, IGFR1, KIT, MET, PDGFRA	PI3K signaling DNA repair Cell cycle progression
			Deletion	PTEN, INPP4B, RB1	Apoptosis
			High expression	CK5, CK6, CK17	
Curtis *et al.*, 2012 (ref. 38)	2,000 breast tumors	mRNA microarrays SNP arrays	Mutation	GATA3 (Clust 1) PIK3CA, CDH1, RUNX1 (Clust 3) TP53 (Clust 5, 9, 10) MP3K1, CTCF (Clust 7) PIK3CA, GATA3, MAP2K4 (Clust 8)	Cell cycle regulation Apoptosis Immune response Proliferation Invasion DNA damage repair Tumor initiation
			Amplification	HER2 (Clust 5), ZNF703 (Clust 6)	
			Deletion	TCR (Clust 4), PPP252A (Clust 9)	
			High expression	RPS6KB1, PPM1D, PTRH2, APPBP2 (Clust 1) CCND1, EMSY, PAK1, RSF1, INTS4 (Clust2)	

*HER2+: tumors with HER2 amplification. HER2-E: tumors classified into HER2+ molecular subtype; HER2-Lum: tumors classified into luminal subtypes.

APPENDIX 4. References of materials and reagents.

Product	Manufacturer	Reference
Cell culture		
0.25% Trypsin-EDTA (1X)	GIBCO	25200-056
Bovine serum albumin (BSA)	Sigma-Aldrich	A7906
Cell strainer (100 µm)	Corning	352360
Cell strainer (40 µm)	Corning	352340
CellTiter 96® AQueous One Solution Cell Proliferation Assay (MTS)	Promega	G3580
Cellulose acetate filters (0.20 µm)	Sartorius	17597-K
DMSO	Sigma-Aldrich	41639
Dulbecco's Modified Eagle's Medium (DMEM)	Sigma-Aldrich	D6429
Dulbecco's Phosphate Buffered Saline (DPBS)	Sigma-Aldrich	14190-094
ECM Gel from Engelbreth-Holm-Swarm murine sarcoma	Sigma-Aldrich	E1270
Fetal bovine serum (FBS)	GIBCO	10270-106
Fibronectin	BD Biosciences	356008
GlutaMAX™ (100X)	GIBCO	35050-038
HEPES (1M)	Lonza	BE17-737E
Luciferase Assay System	Promega	E1500
MycoAlert® Mycoplasma Detection Kit	Lonza	LT07-318
Penicillin-Streptomycin 10 000 U/ml	GIBCO	15140-122
PureCol™ (3 mg/ml collagen)	Inamed Biomaterials	5005-B
Red Blood Cell Lysis Buffer	Sigma-Aldrich	R7757
RPMI 1640 with ultraglutamine 1	Lonza	BE12-702F/U1
Sodium pyruvate (100 mM)	Lonza	BE13-115E
Transwell® Permeable Support 8.0 µm pores	Costar	3422
Trypan Blue	Sigma-Aldrich	93595
Plasmids		
Mission Lentiviral Packaging Mix	Sigma-Aldrich	SHP001
PLKO.1-puro empty vector	Sigma-Aldrich	SHC001
pMD2.G	Addgene	12259
shControl	Sigma-Aldrich	SHC002
shRNAs targeting human EPCR	Sigma-Aldrich	SHCLNG_NM_006404
shRNAs targeting murine EPCR	Sigma-Aldrich	SHCLNG_NM_011171
Bacterial growth and plasmid extraction		
Ampicillin	Sigma-Aldrich	A9518
ATP Plasmid Mini Kit	ATP Biotech Inc.	APD100
Luria Broth (LB)	Conda	1231
Transfections and infections		
Cellulose acetate filters (0.45 µm)	Sartorius	17598
Opti-MEM I Reduced Serum Medium	GIBCO	51985-026
Polybrene®	Sigma-Aldrich	AL-118
Puromycin (10 mg/ml)	InvivoGen	ant-pr-1
X-tremeGENE HP DNA Transfection Reagent	Roche	06366244001
DNA and RNA		
1 kb DNA ladder	Invitrogen	10787-018
Agarose D1 Low EEO	Conda	8010
BIOTAQ DNA polymerase	Bioline	BIO-21040
Blue/Orange DNA loading dye (6X)	Promega	G190A
DyNAmo cDNA Synthesis Kit	Thermo Scientific	F470L
FastStart Universal Probe Master (ROX)	Roche	04913957001
FastStart Universal SYBR Green Master (ROX)	Roche	04913850001
RNeasy Mini Kit	Qiagen	74104
SYBR® Safe DNA Gel Stain	Invitrogen	S33102
TRIzol	GIBCO	15596-018
Western blot		
30% Acrylamide/Bis Solution, 29:1	Bio-Rad	161-0156
Ammonium persulfate (APS)	Bio-Rad	161-0700
Hyperfilm™ ECL	Amersham	28906837
Lumi-Light PLUS Western Blotting Substrate	Roche	12015196001
Nitrocellulose membrane	Bio-Rad	162-0112
Pierce BCA Protein Assay Kit	Thermo Scientific	23225

Precision Plus Protein™ Dual Color Standard	Bio-Rad	161-0374
Protease inhibitor cocktail	Roche	11836170001
Restore™ Western Blot Stripping Buffer	Thermo Scientific	21059
TEMED	Bio-Rad	161-0800
Flow cytometry		
7AAD	BD Biosciences	555815
Alexa Fluor 647-conjugated annexin-V	Invitrogen	A23204
Click-iT® EdU Flow Cytometry Assay Kit	Invitrogen	C10424
Ribonuclease A	Sigma-Aldrich	R6513
Other reagents		
APC	Eli Lilly	Xigris®
Staurosporine	Sigma-Aldrich	S5921
TRAIL	Sigma-Aldrich	T9701
Antibodies		
Flow cytometry		
Alexa Fluor 647 Goat Anti-rat	Invitrogen	A21247
CD11b-PE	BD Pharmigen	557397
CD19-APC-eFluor 780	eBioscience	47019380
CD45-APC	BD Pharmigen	559864
FITC Goat Anti-mouse	BD Pharmigen	554001
FITC Mouse Anti-rat	BD Pharmigen	553892
Ly6C- PE-Cy7	BioLegend	128017
Ly6G-APC-eFluor 780	eBioscience	47593180
MHCII-eFluor 450	eBioscience	48532180
Mouse IgG1, κ	BD Pharmigen	557273
Mouse IgG2a, κ	BD Pharmigen	553454
Nkp46-eFluor 450	eBioscience	48335180
PAR1 (ATAP2)	Santa Cruz	sc-13503
Rat IgG1,κ	BD Pharmigen	559072
Rat IgG1a-eFluor 450	eBioscience	48432180
Rat IgG1a-PE	eBioscience	12432180
Rat IgG2b-APC	BD Pharmigen	553991
Rat IgG2c-PE-Cy7	BioLegend	400721
S1P1 (MM0044-7M15)	Abcam	ab72806
TM (QBEND-40)	Thermo Scientific	MA1-90642
Western blot		
Anti-mouse IgG-HRP	Amersham	NA931
Anti-rabbit IgG-HRP	Amersham	NA934
Anti-rat IgG-HRP	Amersham	NA935
PARP	Cell Signaling	9542
β-actin (AC-15)	Sigma-Aldrich	A5441
β-tubulin (H-235)	Santa Cruz	sc-9104
Immunohistochemistry		
Caspase-3	Cell Signaling	9661
CD41	Dianova	DIA 310
EnVision anti-mouse	Dako	K4007
EnVision anti-rabbit	Dako	K4011
F4/80	eBiosciences	14-4801-82
Ki67	Neomarkers	RM9106
pERK	Cell Signaling	9101
Rabbit anti-rat	Dako	E0468
Vimentin	Dako	M0725
In vivo experiments		
4% formaldehyde	Panreac	252931.1315
D-luciferin	Promega	E-160X
IgG from rat serum	Sigma-Aldrich	I4131
Isofluorane	Braun	Isovet®
Ketamine (50 mg/ml)	Merial	Imalgene®
Matrigel, Growth Factor Reduced	BD Biosciences	354230
Mini-R S Film	Carestream Health	1732726
Osteosoft	Merck	1017281000
Xylazine (2%)	Bayer Healthcare	Rompun®

APPENDIX 5. Upregulated and downregulated genes in EPCR-silenced mammary tumors.

Probeset_ID	Gene Name	Gene Description	logFC.sh1	logFC.sh2	logFC
16917949	CST4	cystatin S	-1,43	-2,35	-1,79
17006863	HSPA1A	heat shock 70kDa protein 1A	-0,64	-2,64	-1,63
17038309	HSPA1B	heat shock 70kDa protein 1B	-0,56	-2,58	-1,61
16713309	FZD8	frizzled family receptor 8	-1,10	-1,25	-1,41
16829085	SLC7A5	solute carrier family 7 (amino acid transporter light chain, L system), member 5	-0,57	-1,76	-1,28
17000235	SPOCK1	sparc/osteonectin, cwcv and kazal-like domains proteoglycan (testican) 1	-0,58	-1,33	-1,14
16837938	ITGB4	integrin, beta 4	-0,43	-1,60	-1,13
17067314	SCARA3	scavenger receptor class A, member 3	-0,86	-0,91	-1,13
16848902	UNC13D	unc-13 homolog D (C. elegans)	-0,49	-1,83	-1,10
17098504	SNORA65	small nucleolar RNA, H/ACA box 65	-0,77	-2,03	-1,09
16860709	GPI	glucose-6-phosphate isomerase	-0,45	-1,49	-1,07
17007543	ITPR3	inositol 1,4,5-trisphosphate receptor, type 3	-0,53	-1,72	-1,05
16931384	GTSE1	G-2 and S-phase expressed 1	-0,28	-1,59	-1,01
17071119	PTDSS1	phosphatidylserine synthase 1	-0,47	-1,39	-1,01
16741287	CPT1A	carnitine palmitoyltransferase 1A (liver)	-0,41	-1,63	-1,01
17117441	MIG7	mig-7	-0,73	-2,11	-0,95
16694359	SCARNA4	small Cajal body-specific RNA 4	-0,45	-1,77	-0,93
17099114	FNBP1	formin binding protein 1	-0,54	-1,07	-0,91
17078558	PAG1	phosphoprotein associated with glycosphingolipid microdomains 1	-0,73	-1,06	-0,90
16858210	SLC44A2	solute carrier family 44, member 2	-0,42	-1,35	-0,88
16878137	CAD	carbamoyl-phosphate synthetase 2, aspartate transcarbamylase, and dihydroorotase	-0,37	-1,30	-0,87
16672426	RNA5SP60	RNA, 5S ribosomal pseudogene 60	-0,51	-1,16	-0,87
17062985	PODXL	podocalyxin-like	-0,53	-1,23	-0,86
16689734	MIG7	mig-7	-0,55	-1,75	-0,86
17082366	PLEC	plectin	-0,42	-1,41	-0,85
17059955	PDK4	pyruvate dehydrogenase kinase, isozyme 4	-0,42	-0,92	-0,84
16942103	FLNB	filamin B, beta	-0,44	-1,29	-0,82
16837226	SNORA38B	small nucleolar RNA, H/ACA box 38B	-0,47	-1,54	-0,81
17051286	FLNC	filamin C, gamma	-1,05	-0,90	-0,80

16660976	SEPN1	selenoprotein N, 1	-0,45	-1,10	-0,80
16685227	STK40	serine/threonine kinase 40	-0,33	-1,32	-0,80
16844775	KRT19	keratin 19	-0,51	-1,11	-0,80
16683264	HTR1D	5-hydroxytryptamine (serotonin) receptor 1D, G protein-coupled	-0,45	-1,13	-0,79
16756627	UNG	uracil-DNA glycosylase	-0,49	-1,14	-0,79
16857567	ARHGEF18	Rho/Rac guanine nucleotide exchange factor (GEF) 18	-0,50	-1,16	-0,79
16913065	PROCR	protein C receptor, endothelial	-0,76	-0,81	-0,79
17073759	HSF1	heat shock transcription factor 1	-0,46	-1,03	-0,76
16680284	CCNL2	cyclin L2	-0,56	-1,03	-0,75
16867680	KHSRP	KH-type splicing regulatory protein	-0,30	-1,08	-0,74
17008544	BYSL	bystin-like	-0,36	-1,13	-0,73
16866002	ZNF543	zinc finger protein 543	-0,35	-0,97	-0,71
16663621	PTPRF	protein tyrosine phosphatase, receptor type, F	-0,45	-0,91	-0,71
16682348	ATP13A2	ATPase type 13A2	-0,26	-1,36	-0,71
16857630	PNPLA6	patatin-like phospholipase domain containing 6	-0,39	-0,93	-0,70
17065811	FDFT1	farnesyl-diphosphate farnesyltransferase 1	-0,36	-0,86	-0,69
16698298	KISS1	KiSS-1 metastasis-suppressor	-0,50	-1,07	-0,68
16782153	OXA1L	oxidase (cytochrome c) assembly 1-like	-0,57	-1,22	-0,67
17066601	SLC39A14	solute carrier family 39 (zinc transporter), member 14	-0,52	-0,82	-0,67
16693173	MRPL9	mitochondrial ribosomal protein L9	-0,44	-0,85	-0,67
17063480	PARP12	poly (ADP-ribose) polymerase family, member 12	-0,33	-0,88	-0,63
16770507	DDX54	DEAD (Asp-Glu-Ala-Asp) box polypeptide 54	-0,39	-0,89	-0,63
16819539	GPR56	G protein-coupled receptor 56	-0,35	-0,86	-0,62
16911132	PRNP	prion protein	-0,29	-1,11	-0,60
17073565	CYC1	cytochrome c-1	-0,44	-0,75	-0,59
16759283	RNA5SP376	RNA, 5S ribosomal pseudogene 376	-0,56	-1,19	-0,59
16845794	KIF18B	kinesin family member 18B	-0,28	-0,95	-0,59
16850107	FASN	fatty acid synthase	-0,26	-0,84	-0,58
16741501	DHCR7	7-dehydrocholesterol reductase	-0,32	-0,71	-0,57
16991991	WWC1	WW and C2 domain containing 1	-0,52	-0,69	-0,54
17114728	MAGEC2	melanoma antigen family C, 2	-0,54	-0,72	-0,54

16895941	FNDC4	fibronectin type III domain containing 4	-0,35	-0,70	-0,53
16839642	CLUH	clustered mitochondria (cluA/CLU1) homolog	-0,28	-0,76	-0,52
16847520	TBC1D3P2	TBC1 domain family, member 3 pseudogene 2	-0,40	-0,77	-0,51
16680420	SLC35E2B	solute carrier family 35, member E2B	-0,48	-0,72	-0,49
16829801	SPNS2	spinster homolog 2 (Drosophila)	-0,32	-0,84	-0,48
16925983	C2CD2	C2 calcium-dependent domain containing 2	-0,32	-0,67	-0,48
16657730	GLTPD1	glycolipid transfer protein domain containing 1	-0,39	-0,75	-0,48
16680348	SSU72	SSU72 RNA polymerase II CTD phosphatase homolog (S. cerevisiae)	-0,32	-0,62	-0,46
16758585	SETD8	SET domain containing (lysine methyltransferase) 8	-0,40	-0,72	-0,44
16680478	GNB1	guanine nucleotide binding protein (G protein), beta polypeptide 1	-0,27	-0,67	-0,44
16680435	SLC35E2	solute carrier family 35, member E2	-0,28	-0,72	-0,42
16928967	MTFP1	mitochondrial fission process 1	-0,35	-0,66	-0,42
16948967	SNORD66	small nucleolar RNA, C/D box 66	-0,32	-0,80	-0,41
17066523	BMP1	bone morphogenetic protein 1	-0,28	-0,61	-0,41
16930954	TSPO	translocator protein (18kDa)	-0,28	-0,65	-0,38
16724779	OR5T1	olfactory receptor, family 5, subfamily T, member 1	0,34	0,79	0,36
17063924	TMEM139	transmembrane protein 139	0,30	0,69	0,36
16947605	MIR16-2	microRNA 16-2	0,56	0,93	0,48
16708744	WBP1L	WW domain binding protein 1-like	0,39	0,93	0,58
17102861	KDM6A	lysine (K)-specific demethylase 6A	0,39	1,04	0,58
16672349	OR10K1	olfactory receptor, family 10, subfamily K, member 1	0,33	0,85	0,59
16721771	KRT8P41	keratin 8 pseudogene 41	0,39	0,81	0,61
16735734	MTRNR2L8	MT-RNR2-like 8	0,41	1,07	0,63
16781602	RNASE3	ribonuclease, RNase A family, 3	0,50	0,99	0,64
16947061	MBNL1	muscleblind-like splicing regulator 1	0,29	1,16	0,69
17118273	PTN	pleiotrophin	0,32	1,17	0,70
16773581	RNU6-82P	RNA, U6 small nuclear 82, pseudogene	1,31	1,16	0,76
16906285	CALCRL	calcitonin receptor-like	0,80	0,75	0,81
16668582	CD53	CD53 molecule	0,34	0,98	0,81
16924143	TPTE	transmembrane phosphatase with tensin homology	0,78	1,33	0,84
17112918	BEX1	brain expressed, X-linked 1	0,68	1,63	1,07

APPENDIX 6. Functional analysis with Ingenuity (IPA®).

Diseases or Functions Annotation	p-Value	Activation z-score	Molecules	# Molecules
Angiogenesis	2,57E-02	-0,992	CALCRL,DHCR7,FLNB,FZD8,GPR56,HSF1,ITGB4,PNPLA6,PROCR,PTN	10
Apoptosis	9,59E-03	0,382	BMP1,CALCRL,CCNL2,CD53,FASN,FLNB,GPI,HSF1,HSPA1A/HSPA1B,ITGB4,mir-15,ITPR3,KISS1,MTFP1,PRNP,PROCR,PTN,PTPRF,SEPN1,SETD8,SPOCK1,STK40,TSPO,UNG	24
Behavior	9,36E-03	-0,616	ATP13A2,CPT1A,DHCR7,GNB1,HSPA1A/HSPA1B,ITPR3,PRNP,PTN,PTPRF,SEPN1,UNG,WWC1	12
Binding of cells	1,37E-02	-1,432	CALCRL,ITGB4,PRNP,PTPRF,RNASE3,SCARA3,SLC7A5	7
Cell cycle progression	4,22E-03	1,094	FASN,GPI,GTSE1,HSF1,HSPA1A/HSPA1B,ITGB4,KIF18B,KRT19,mir-15,PTN,PTPRF,SETD8,WWC1	13
Cell death	1,95E-03	1,655	ATP13A2,BMP1,CALCRL,CCNL2,CD53,DHCR7,FASN,FDFT1,FLNB,GPI,GPR56,HSF1,HSPA1A/HSPA1B,ITGB4,ITPR3,KISS1,KRT19,mir-15,MTFP1,PLEC,PRNP,PROCR,PTN,PTPRF,RNASE3,SEPN1,SETD8,SPOCK1,STK40,TSPO,UNG	31
Cell death of brain cells	1,20E-02	1,048	ATP13A2,HSF1,PRNP,RNASE3,UNG	5
Cell death of breast cancer cell lines	2,47E-02	2,196	FASN,HSPA1A/HSPA1B,ITGB4,mir-15,PRNP	5
Cell death of cancer cells	3,62E-03	-0,092	FASN,HSF1,HSPA1A/HSPA1B,mir-15,PRNP,PTN	6
Cell death of cerebral cortex cells	2,58E-02	0,694	ATP13A2,HSF1,PRNP,UNG	4
Cell death of neuroblastoma cell lines	1,20E-02	0,786	ATP13A2,HSF1,HSPA1A/HSPA1B,PRNP	4
Cell death of tumor cell lines	9,73E-03	1,681	ATP13A2,CCNL2,FASN,FDFT1,FLNB,GPI,HSF1,HSPA1A/HSPA1B,ITGB4,ITPR3,KISS1,mir-15,MTFP1,PRNP,PTPRF,SPOCK1	16
Cell death of tumor cells	6,01E-04	-0,362	DHCR7,FASN,HSF1,HSPA1A/HSPA1B,mir-15,PRNP,PROCR,PTN	8
Cell movement	2,33E-03	-1,572	CALCRL,FASN,FLNB,FLNC,GNB1,GPI,GPR56,HSPA1A/HSPA1B,ITGB4,KISS1,KRT19,mir-15,PLEC,PODXL,PRNP,PROCR,PTN,PTPRF,SETD8,SPNS2,TSPO,WWC1	22
Cell movement of fibrosarcoma cell lines	3,37E-05	-0,900	FLNB,FLNC,GPI,KISS1	4
Cell movement of tumor cell lines	1,18E-02	-1,354	FLNB,FLNC,GNB1,GPI,ITGB4,KISS1,KRT19,PODXL,PRNP,PTN	10
Cell spreading	1,26E-02	-1,715	FLNB,FLNC,ITGB4,PODXL,PRNP	5
Cellular homeostasis	2,01E-02	-0,610	FZD8,GNB1,GPI,HSF1,HTR1D,ITGB4,ITPR3,KISS1,mir-15,PAG1,PDK4,PRNP,PROCR,SLC39A14,SPNS2	15
Concentration of lipid	1,42E-02	0,318	CPT1A,DHCR7,FASN,FDFT1,KISS1,PDK4,PNPLA6,PRNP,PTDSS1,SPNS2	10
Contact growth inhibition	5,37E-03	1,177	GPI,HSPA1A/HSPA1B,mir-15,WWC1	4
Development of cardiovascular system	2,06E-02	-0,992	CALCRL,DHCR7,FLNB,FZD8,GPR56,HSF1,ITGB4,KDM6A,PLEC,PNPLA6,PROCR,PTN	12
Epithelial-mesenchymal transition	1,30E-02	-0,686	GPI,KISS1,PRNP,WWC1	4
Fatty acid metabolism	2,92E-02	-1,951	CPT1A,FASN,KISS1,PDK4,PRNP,SPNS2,TSPO	7

Growth of organism	1,28E-02	-1,980	BYSL,DHCR7,FDFT1,HSF1,ITPR3,KDM6A,KRT19,PRNP,PTN,STK40	10
Growth of tumor	7,42E-03	-1,019	FASN,GPR56,HSF1,HSPA1A/HSPA1B,KISS1,MAGEC2,mir-15,PLEC,PROCR,PTN	10
Invasion of breast cancer cell lines	5,43E-03	-1,432	GPI,ITGB4,KISS1,KRT19,PODXL	5
Invasion of malignant tumor	5,73E-03	0,000	CD53,FASN,ITGB4,KISS1	4
Invasion of tumor	6,97E-03	0,000	ARHGEF18,CD53,FASN,ITGB4,KISS1	5
Locomotion	8,21E-03	0,391	FASN,HSPA1A/HSPA1B,PNPLA6,PRNP,PTPRF,UNG	6
Mass of organism	6,69E-03	-2,425	FASN,FLNB,FLNC,HSPA1A/HSPA1B,ITPR3,PTPRF	6
Metastasis	2,43E-02	0,128	BEX1,FASN,FDFT1,ITGB4,ITPR3,KISS1,PRNP,PROCR,PTN	9
Migration of cells	1,38E-03	-1,382	CALCRL,FASN,FLNB,FLNC,GPI,GPR56,HSPA1A/HSPA1B,ITGB4,KISS1,KRT19,mir-15,PLEC,PODXL,PRNP,PROCR,PTN,PTPRF,SETD8,SPNS2,TSPO,WWC1	21
Migration of connective tissue cells	1,06E-02	-1,029	CALCRL,FLNB,PLEC,PTN	4
Migration of epithelial cells	2,22E-04	-0,555	ITGB4,PLEC,PTN,PTPRF,SETD8	5
Migration of tumor cell lines	2,47E-02	-0,729	FLNB,FLNC,ITGB4,KISS1,KRT19,PODXL,PRNP,PTN	8
Necrosis	1,36E-02	2,110	ATP13A2,CALCRL,CCNL2,DHCR7,FASN,FDFT1,FLNB,GPI,HSF1,HSPA1A/HSPA1B,ITGB4,ITPR3,KISS1,mir-15,MTFP1,PLEC,PRNP,PROCR,PTN,PTPRF,RNASE3,SPOCK1,UNG	23
Neoplasia of cells	1,29E-03	-1,238	FASN,GPI,ITGB4,KISS1,mir-15,PDK4,PRNP,PROCR	8
Neoplasia of tumor cell lines	1,31E-02	-0,277	KISS1,mir-15,PDK4,PRNP,PROCR	5
Neuronal cell death	1,05E-02	1,349	ATP13A2,GPI,HSF1,mir-15,PRNP,PTN,PTPRF,RNASE3,UNG	9
Organismal death	1,19E-03	3,260	BMP1,BYSL,CALCRL,CPT1A,DHCR7,FASN,FDFT1,FLNB,FLNC,GNB1,HSF1,ITGB4,ITPR3,KDM6A,KRT19,PLEC,PNPLA6,PRNP,PROCR,PTPRF,SETD8,SLC7A5,STK40,UNC13D,UNG	25
Organization of cytoplasm	2,41E-02	-0,105	ARHGEF18,FASN,FLNB,FLNC,FNBP1,GPI,ITGB4,KIF18B,KISS1,MTFP1,PLEC,PRNP,PTN,PTPRF,SEPN1	15
Proliferation of cells	4,92E-03	-0,920	BMP1,BYSL,CALCRL,CCNL2,DHCR7,FASN,FDFT1,FZD8,GNB1,GPI,GPR56,HSF1,HSPA1A/HSPA1B,ITGB4,ITPR3,KDM6A, KISS1,KRT19,mir-15,PAG1,PDK4,PLEC,PRNP,PROCR,PTN,PTPRF,RNASE3,SETD8,SLC7A5,SPOCK1,TSPO,WWC1	32
Proliferation of prostate cancer cell lines	1,53E-02	-1,452	FASN,FDFT1,PDK4,PTN,SLC7A5	5
Proliferation of tumor cells	1,25E-02	-0,522	FASN,HSF1,HSPA1A/HSPA1B,KISS1,mir-15,PROCR,PTN	7
Senescence of cells	2,88E-02	0,688	FASN,GPI,HSPA1A/HSPA1B,mir-15	4
Synthesis of lipid	1,65E-02	-1,943	DHCR7,FASN,FDFT1,KISS1,PDK4,PNPLA6,PRNP,PTDSS1,TSPO	9
Tumorigenesis of cells	6,56E-03	-1,109	GPI,mir-15,PDK4,PRNP,PROCR	5
Tumorigenesis of tumor cell lines	6,37E-03	-0,762	mir-15,PDK4,PRNP,PROCR	4